UNIVERSITY OF PADUA
FACULTY OF ENGINEERING
—
Dept. of Innovation In Mechanics and Management
—
Doctoral School of Industrial Engineering
Curriculum in Mechatronics and Industrial Systems
Cycle XXIII

ANALYSIS AND DEVELOPMENT OF CABLE-DRIVEN ROBOTIC DEVICES

A dissertation submitted in partial fulfillment
of the requirements for the degree of
Doctor of Philosophy in Mechatronics and Industrial Systems

Prof. Paolo Francesco Bariani, Chair of the School
Prof. Alberto Trevisani, Course Coordinator
Prof. Giulio Rosati, Candidate's Supervisor

Ph.D. Candidate: Damiano Zanotto

March 8, 2011

Acknowledgments

The research presented in this thesis has been carried out at the Department of Innovation in Mechanics and Management (DIMEG), University of Padua (Italy), and, partially, at the Mechanical Systems Laboratory (MechSys), University of Delaware (USA).

The author acknowledges his debt to those who have helped to develop the results presented in this thesis. In particular, I wish to express my gratitude to my supervisor, Professor G. Rosati, for his fundamental suggestions and valuable contributions to this work, and to Professor A. Rossi for his continued encouragement.

I would also like to include my gratitude to Professor S. K. Agrawal for his hospitality at the Mechanical Systems Laboratory and for the help he provided in the control of robotic systems. I also gratefully acknowledge the support from the *Fondazione Ing. Aldo Gini*, whose grant has partially funded my research period in the US.

Furthermore, I would like to thank all the Ph.D. candidates at the DIMEG-Robotics Research Group for the assistance they provided during these three years, and the three students who collaborated to the development of the *Sophia-3* prototype.

Finally, I want to thank my family for the encouragement and the support.

Contents

Analysis and Development of Cable-Driven Robotic Devices

Abstract:

The design of a mechanical system is often the result of an *optimization process*, aimed to obtain the best performances inside a given task space under fixed constraints.

Due to the *unilateral actuation*, cable-based devices possess specific features that make some of the tools commonly used in robotics completely unsuitable, thus requiring the definition of specific tools for analysis and design rules.

Even though several examples of geometrical, kinematic and dynamic performance indices have been introduced as analysis tools in the last years, only few authors proposed rigorous *design methodologies*. Traditional approaches seek to find the optimal set of design parameters by maximizing the robot capabilities inside a given reference workspace. However, since most of the properties of cable-based devices depend on both robot geometry (i.e., number and disposition of cable attachment points) and cable configuration (i.e., directions of cables in the end-effector reference frame), the capabilities of a given robot are *extremely variable* throughout the workspace. Thus, the structure of traditional devices often appears cumbersome if compared to the useful workspace they have been designed for.

The aim of this work is first to present a set of local, configuration dependent performance indices that properly characterize cable-based devices. Then, a new methodology is described to obtain effective, well-tailored designs. The formulated design paradigm takes advantage of the introduction of *moving pulley-blocks*, leading to the definition of a new class of cable devices defined as *adaptive cable-based devices*.

In the first half of this thesis, the new methodology is described in detail, and a numerical validation is performed by solving simple case-studies. In order to empirically validate the proposed methodology, the first prototype of *Adaptive cable-based device* has been designed and developed. The second half of this thesis deals with layout definition, mechanical design and control system design of the *Sophia-3* prototype. Finally, results from the first experimental tests on the new device are reported.

Keywords:

cable-driven devices, unilateral actuation, performance indices, kinematic design.

Analisi e Sviluppo di Dispositivi Cable-Driven

Riassunto:

La progettazione di un sistema meccanico é spesso il risultato di un *processo di ottimizzazione*, il cui scopo é quello di massimizzare le performance all'interno di un dato workspace rispettando una serie di vincoli.

A causa dell'*attuazione unilaterale*, i dispositivi cable-driven possiedono caratteristiche specifiche, cosicché gli strumenti di analisi tradizionalmente impiegati in robotica risultano inadeguati o poco efficaci. Di qui la necessitá di definire indici di analisi e metodologie di progettazione specifici.

Sebbene siano stati sviluppati nel corso degli anni svariati indici di performance (geometrici, cinematici e dinamici), solo pochi autori hanno finora proposto metodi di progettazione rigorosi. Negli approcci tradizionali, lo scopo é quello di determinare il set di parametri di progetto che massimizza le performance del dispositivo all'interno di una data regione dello spazio di lavoro. Tuttavia, poiché molte delle proprietá dei dispositivi cable-based dipendono sia dalla geometria del manipolatore (numero di cavi, disposizione delle pulegge alla base, ecc..) sia dalla disposizione dei cavi (cioé dalla direzioni assunte dai cavi rispetto all'end-effector), le performance di un manipolatore risultano estremamente variabili all'interno dello spazio di lavoro. Di conseguenza, l'ingombro complessivo di un robot cable-driven risulta spesso decisamente maggiore rispetto allo spazio di lavoro per il quale é stato progettato.

Lo scopo di questo lavoro consiste dapprima nel presentare un set di indici di performance locali, in grado di caratterizzare le proprietá principali di un dispositivo. Successivamente, viene presentata una nuova metodologia di progettazione basata su questi indici, che permette di ottenere soluzioni progettuali piú efficaci, cioé sviluppate *su misura* in base alle specifiche. La metodologia proposta si basa sull'introduzione di *passacavi mobili*, ed ha condotto alla definizione di una nuova classe di dispositivi cable-based denominati *adattativi*.

Al fine di validare numericamente la procedura, nella prima parte di questa tesi vengono presentati alcuni semplici esempi di progettazione. Allo scopo di dare una validazione empirica alla metodologia introdotta, é stato inoltre progettato e sviluppato il prototipo *Sophia-3*, primo esempio di sistema a cavi adattativo. Nella seconda parte di questa tesi viene presentato il prototipo, descrivendone il layout, la progettazione meccanica e l'architettura del controllo. Vengono inoltre presentati i primi risultati sperimentali dei test effettuati sul nuovo prototipo.

Parole chiave:

dispositivi cable-driven, attuazione unilaterale, indici di performance, progettazione cinematica.

Chapter 1

Introduction

In the last two decades, many research works have been published on cable-based systems, reflecting the considerable interest of the scientific community in this area. Cables are used both in conjunction with rigid-link structures, to remotely actuate serial and parallel kinematic chains, and alone, to directly control the motion of a mobile platform or end-effector (EE). In this section, a brief introduction on cable-based systems is presented. Starting from a basic classification of the robotic systems that employ tendon-like elements, we recall the definition of cable-based parallel robots and their main features. Then, the related Literature on this class of manipulators is outlined. The chapter is completed by a short description of the cable-based rehabilitation devices that have been developed at the rehab-robotics laboratory of the Dept. of Innovation in Mechanics and Management (DIMEG), University Padua, Italy.

1.1 Traditional designs and cable-based robots

When designing new robotic devices, some of the most common requirements designers must take into account are: cost-effectiveness, force capability, dynamic performances, capability of handling large workspaces, repeatability and safety.

The cost of the actuators and those of manufacturing represent main contributions to the overall cost of a robotic device. Therefore, a simple structure employing few components may lead to a cost-effective design. On the other hand, increasing the complexity of the control architecture has usually limited impact on the design costs, since more and more powerful controllers are made available in the market at relatively low prices every few years. Hence, a trend towards *mechanically simple* but *computationally demanding* systems may be expected in the near future [1]. Traditional rigid-link designs are commonly classified into *serial-link* and *parallel-link* robots. Both these subclasses possesses several advantages and several drawbacks with respect to the aforementioned requirements.

Moving large loads is a common task in industrial automation (e.g., cranes, palletizing robots, etc.), unfortunately, traditional rigid-link robots with serial architectures are characterized by low *payload-to-weight* ratios (i.e., cumbersome structures are often required to move relatively small loads). This is primarily due to the fact that each motor must carry the weight and the inertial forces produced by the following links and by the load. The inherently low stiffness of serial structures plays a role in determining the link cross sections as well. In many applications, such as *pick-and-place* tasks, high dynamic performances (i.e., high accelerations and/or high velocities) are desirable to reduce the cycle times. Parallel structures may handle heavier loads, since the overall force is split between the actuators. Parallel structures are also stiffer, thus allowing higher dynamic performances. However, the mechanical structure of those manipulators is rather complex: *ball-and-socket* joints are often employed

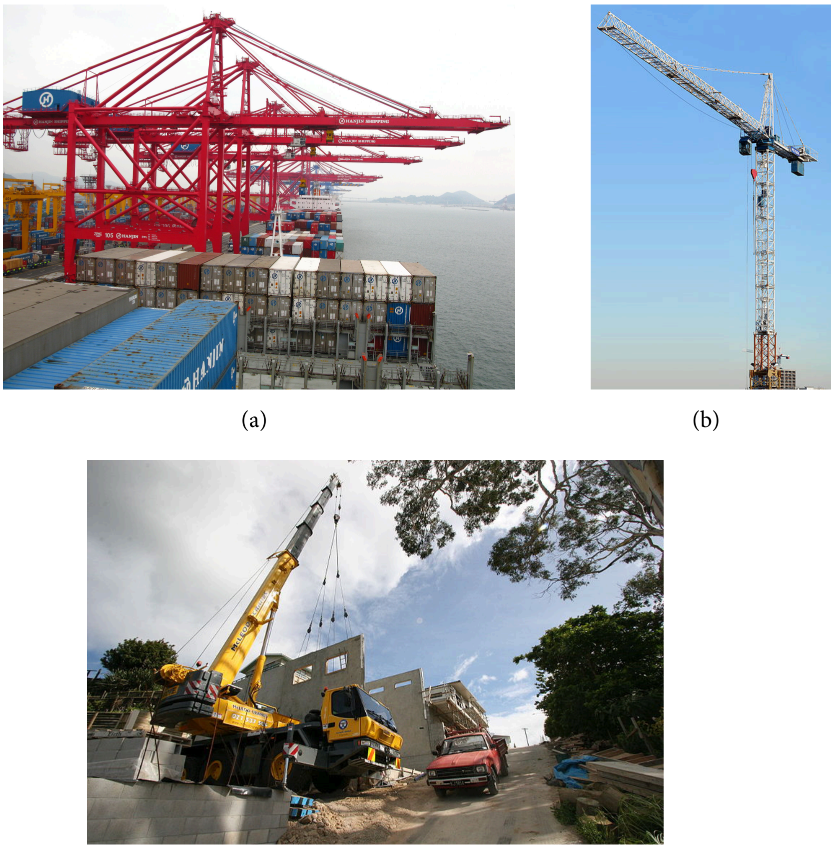

(a) (b)

(c)

Figure 1.1: Examples of crane devices: gantry cranes (a), the tower crane (b) and the mobile crane (c).

between links, preventing large relative motions. Also, singularities and multiple solutions to the forward kinematics arise the complexity of the control system. As a consequence, most of the commercially available parallel devices possess four or less DOFs (degrees of freedom) [2].

The capability of moving heavy objects over large workspaces is typical of *crane-type* structures (Fig. 1.1). Gantry cranes are used to load and unload containers in ships and trains, tower cranes and mobile cranes are employed in building construction. The latter subclasses employ a rigid-link serial structure, whereas gantry cranes use parallel rigid-link structures. In either cases, the rigid-link structure provides additional DOFs to the single cable carrying the load. Those machines are energetically efficient, however, the underconstrained nature of the cranes makes it difficult to implement completely automated systems, even though applications exists where fully automated cranes might be efficiently utilized [3]. Traditionally, sway motions are controlled by operating the device in *quasi-static* conditions.

Usually, a robot is required to possess high *repeatability*[1]. This feature is fundamental

---

[1] Repeatability is a statistical term associated with accuracy. However, repeatability does not describe the error with respect to absolute coordinates: system repeatability is the positional deviation from the average of displacements, as measured in different trials having the same goal target and conducted under the same conditions.

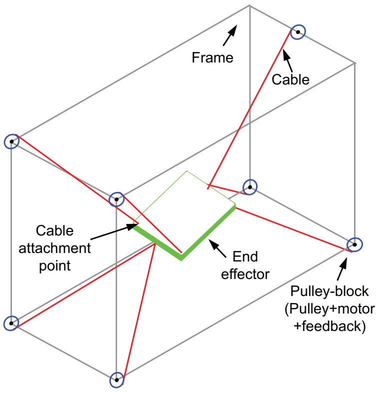

Figure 1.2: Concept drawing of a cable-based parallel device.

in a number of tasks, where either the goal poses (e.g., automatic assembly) or the target trajectories (e.g., continuous soldering, robotic painting) must be reached with high accuracy. There are other applications, however, where a limited degree of accuracy may be acceptable to reduce costs [1].

Safety is a main concern in machine design. Especially when acting in close contact with human operators (e.g., co-robots, tele-operated robots, medical and rehabilitation robots), machines must have redundant safety systems installed, both at the hardware and at the software level. The use of light and intrinsically compliant components instead of rigid massive links further reduces the risk for the operator in case of fault.

The use of cables and tendon-like components in robotics have attracted the interest of many research teams over the last years. As compared to rigid links, cables are lighter and can handle larger loads while guaranteeing considerable ranges of motion. *Cable-based parallel devices* consist of a moving platform supported in-parallel by cables that are actuated by tensioning motors (Fig. 1.2). Usually, each cable is reeled on a pulley that is keyed on the shaft of an electric motor, and has the other extremity fixed to an attaching point on the end effector. A series of idle pulleys may also be interposed between the two extremities of each cable, to measure the cable tension/orientation and to provide fixed reference points for the kinematics. By properly adjusting cable lengths and tensions, the required poses and wrenches are attained.

Several advantages distinguish cable-based systems from common manipulators. Indeed, these manipulators show interesting properties with respect to all the aforementioned keypoints.

First of all, the mechanical architecture is rather simple and cost-effective, even in the case of multiple-DOF spatial systems. Furthermore, since cables are low-weight components, inertia forces are usually limited or, alternatively, very high accelerations can be reached at the end effector. Indeed, examples of cable-based devices for high-speed pick-and-place tasks have been presented in the past years (e.g., [4, 2]).

Low inertial loads may be useful even when moving an object over a predefined trajectory is not the task of the device. Haptic displays are devices capable of reproducing real and

---

Repeatability is a well-known Robot Performance Standard. The currently used definition is the *ISO 9283* one.

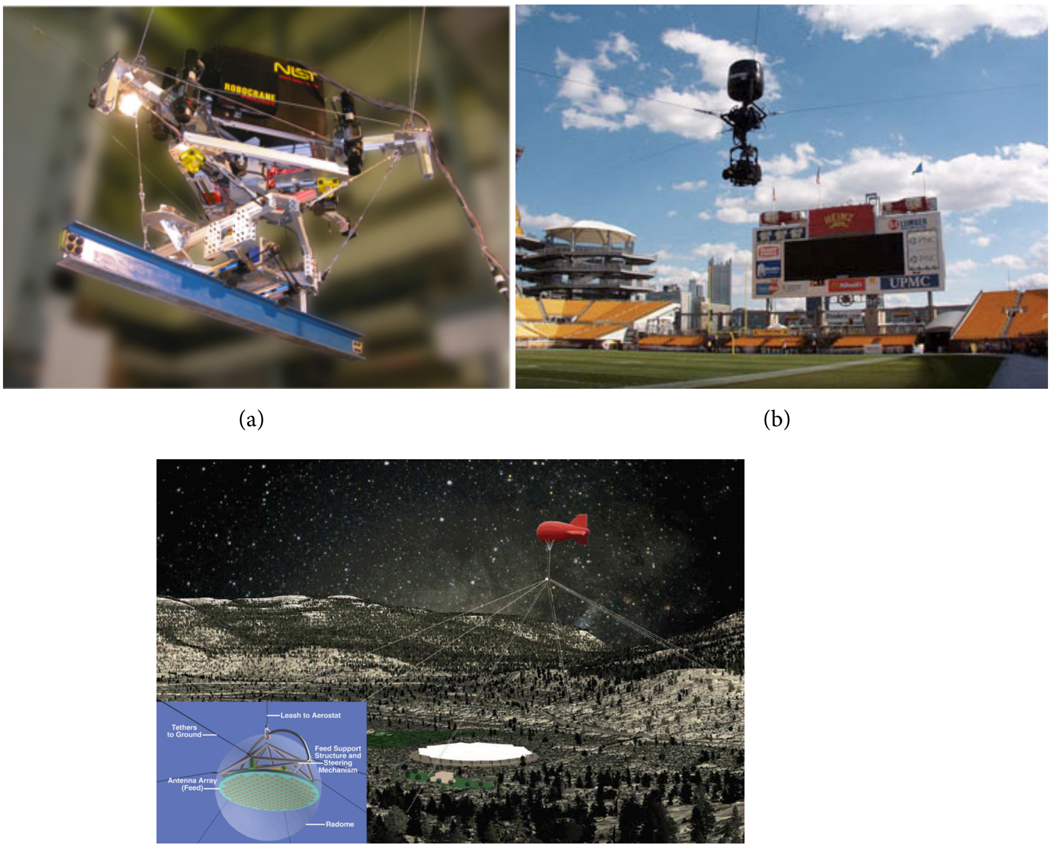

(a) (b)

(c)

Figure 1.3: Cable-based parallel robots with large workspaces: the NIST Robocrane [11] (a), the Skycam [12] (b) and the LAR [13] (c).

virtual environments by exerting a variable mechanical impedance to the user's hand. A low mechanical impedance perceived at the end-effector of the robot (i.e., the interface with the human operator) is crucial to effectively render a large range of virtual environments, thus improving the *transparency* of the device[2].

As a further consequence of the low inertia, cable-based robots often show very high payload-to-weight ratios. Like traditional cranes, underconstrained (or *crane-type*) cable-based robots operate based on the action of gravity [9]. However, the presence of multiple cables allows to control not only the position but also the orientation or the load. This property may be crucial in applications where the quasi-static assumption is not applicable (e.g., cargo to cargo operations [10]), and where sway motions are not tolerable, as in dangerous materials handling [11].

Since long amounts of cable can be reeled on relatively small pulleys, cable-based robots may handle large or even huge workspaces. One of the applications of the NIST Robocrane

---

[2] Haptic transparency is used to quantify the fidelity with which the properties of virtual objects are presented to and perceived by the human operator [5]. Examples of cable-based haptic displays have been presented in recent years [6, 7, 8].

(Fig. 1.3(a)), a six-DOF tendon-based parallel manipulator developed by the National Institute of Standards and Technology, is the maintenance of large aicrafts [11, 14]. Skycam (Fig. 1.3(b)) is an example of aerial, cable-driven camera used in stadiums and arenas [12, 15]. A cable-driven mobile platform has been theorized to be used in contour crafting fabrication technology [16]. The LAR (Large Adaptive Reflector [13]) and the Arecibo Radio Telescope [17] are radioscopes wherein the receiver is lifted by an aerostat and position-controlled by a set of cables (Fig. 1.3(c)). Additionally, the possibility to handle large workspaces implies that motors can be located sufficiently away from the end-effector, therefore, these systems might be used in hazardous environments for rescue purposes [18].

High levels of accuracy and repeatability are hardly achieved with cable-based devices. Polymeric cables under load deform in a non-linear, time dependent fashion, thus making it difficult to compensate elasticity by control. Without well designed pulleys and alignment systems, cables wind around pulleys in a non-ideal way, thus introducing a further source of position error. Auxiliary idle pulleys, on the other hand, introduce friction forces which must be compensated as well. In spite of this, kinematic redundancy may be exploited to compute good estimates of the pose of the moving platform. Indeed, examples can be found in the Literature where passive cable-based devices are used as metrology systems [19].

The basic characteristic of cable-based devices is the *unilateral actuation* (i.e., cables can only carry tension forces [20, 21]). As it will be discussed later in this chapter, this feature has many implications, making it crucial to choose the appropriate number of actuators and their locations based on the design requirements. Nonetheless, unilateral actuation can also be exploited to improve the system safety, which is essential for devices that must interact with human operators (e.g. medical applications). Indeed, subjects tend to feel less constrained when interacting with cables instead of rigid links [22].

Lastly, as a further advantage over traditional rigid-link devices, these manipulators are very suitable for modular designs that allow rearrangeable configurations and easy transportability.

1.2 Cable-driven designs and cable-based parallel robots

In the past years, the employment of cables in robotics gave rise to a variety of design solutions. Basically, cables may *work in conjunction* with a rigid-link structure by actuating the kinematic chain, or may *substitute* traditional rigid-link structures, by directly acting on a rigid body (i.e., the moving platform or end-effector). In both cases, the motors may be mounted at the base of the manipulator, thus reducing the inertial load. The focus of this work is on the latter class of devices.

Cable-driven serial link structures (Fig. 1.4) are often used in planar devices (e.g. [25, 26]). Even though hybrid solutions have been developed where a parallel chain made by cables is employed to actuate the serial structure [27, 28], the commonly adopted layout is the one having each cable passing through the previous joints before reaching the corresponding rigid link (e.g., [23]). Thus, it may be an issue to guide cables around the joints in 3D applications. The problem can be tackled by using bowden cables [29, 24], however, this solution increases friction, which must be compensated by control. Prototypes of this class of

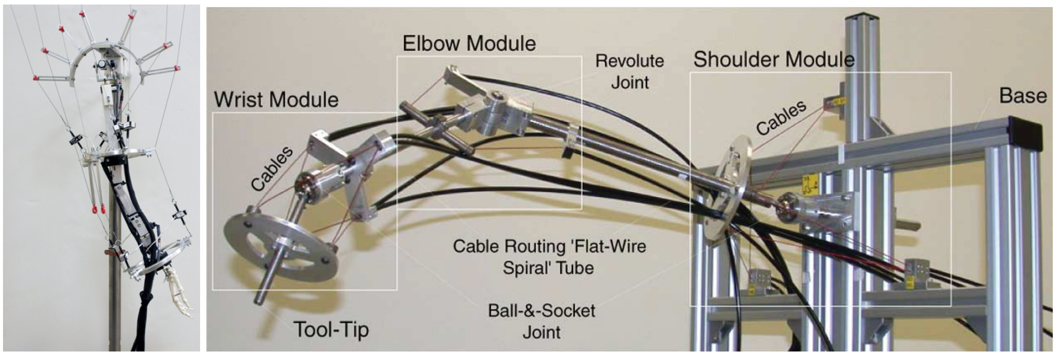

(a) (b)

Figure 1.4: Two examples of cable-driven serial link structures: (a) the Wearable cable-driven upper arm exoskeleton [23]; (b) the Biologically Inspired Cable-Driven Robotic Arm [24].

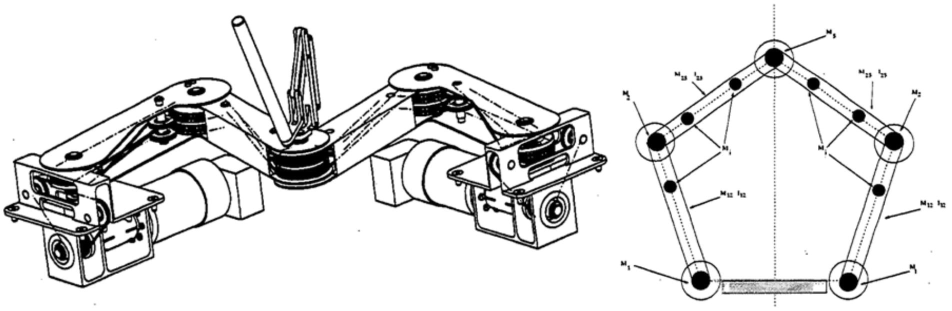

Figure 1.5: Haptic display consisting of a parallel rigid-link structure driven by cables [33].

manipulators have been recently presented in the field of rehabilitative robotics [30]. Determining the controllable workspace of generic cable-driven open chains still remains an open question, even though a novel study has recently been published, which deals with this topic [31]. Parallel rigid-link chains that are driven by cables have been designed as well (Fig. 1.5). These designs present a further advantage, as the load can be distributed among the actuators [32, 33].

This work focuses on *cable-based parallel robots*, i.e., those devices where a single rigid body, called the end-effector, is directly supported by cables (Fig. 1.2). Traditionally, each cable is actuated by an independent motor, which controls the cable length and tension. Besides the actuated cables, a set of passive, fixed-length wires may also be installed to constrain the movements of the platform [32].

A main difference between cable-based parallel systems and common parallel robots is that cables can only carry tension forces. This characteristic is usually referred to as *unilateral actuation*. The use of elements capable of exerting unilateral forces has many implications. First of all, having the number of actuators greater than the number of DOFs forces the designer to employ algorithms that seek a feasible tension distribution for any given wrench. Secondly, unlike traditional rigid-link devices, the workspace does not depend on geometric constraints solely. Indeed, the *workspace* wherein the mobile platform is controllable is a function of both the cables configuration and of the allowable range for the cable tensions.

As it will be discussed in the following section, the analysis and optimization of the workspace is a major topic in the related Literature [32]. The broadest definitions of workspace (eg. *"theoretical"* [34], *"force-closure"* [35], *"statics"* [34], *"controllable"* [36] or "useful" [32] workspace) are purely geometrical. These depend on cable disposition only and are related to the capability of exerting arbitrary wrenches at end-effector. Other workspaces may be defined as subsets of the previous ones, by introducing additional requirements (e.g. cable tension constraints, required set of wrenches or accelerations, etc..).

Definition 1.2.1. We define the *workspace* of a cable-based system as the set of end-effector poses in which the system is *manipulable* [37]. A cable-based system is *manipulable* at a given configuration if any wrench can be exerted with only positive tensions on cables[3].

A necessary and sufficient condition for a cable-based robot to be manipulable was first investigated by Y. Shen e H. Osumi [40], who stated that a rigid body with m DOFs can be manipulated by at least $n = m + 1$ cables *if and only if* the structure matrix $\mathbf{A}$[4], that maps the vector of cable tensions to that of the exerted wrenches is full rank, and there exists a vector $\boldsymbol{\alpha} \in \ker(\mathbf{A})$ s.t. $(\boldsymbol{\alpha} > \mathbf{0}) \vee (\boldsymbol{\alpha} < \mathbf{0})$ [5].

Following to the previous condition, Verhoeven [1] classified cable-driven systems into *Incompletely Restrained Positioning Mechanisms* (IRPMs, $n \leq m + 1$), *Completely Restrained Positioning Mechanisms* (CRPMs, $n = m + 1$), and *Redundantly Restrained Positioning Mechanisms* (RRPMs, $n > m + 1$). This classification derived from a previous notation by Ming and Higuchi [41]. IRPM are not manipulable by means of the forces exerted by the cables. Indeed, they relies on an external force to keep the cables stretched, which can be provided by dynamics, gravity, or an extra actuator/spring. The definition of *tensionability* was introduced to address the aptitude of an IRPM to remain in tension under any loading, with a large enough ballast force [38].

Clearly, knowing the workspace of the system and its force exertion capabilities is crucial for planning even basic tasks. Unfortunately, close-form definitions of the workspace boundaries are available for specific classes of devices only [42]. The common tools to investigate general designs are numerical algorithms. In [43], a distinction is pointed out between *discrete* and *continuous* numerical algorithms.

In the former approach, the feasible range of values for each design parameter is discretized into a set of values. A superset of the target workspace (usually a *spatial box*) is also discretized into a grid of equally spaced points. Then, for each combination of the design parameters, a certain performance index is computed in each point of the grid. The resulting optimal design is the one yielding the maximum average value of the performance index [21]. Sometimes the number of points belonging to the controllable workspace is employed instead of a specific performance index.

---

[3] Other authors used different, equivalent terms to denote the condition of manipulability (e.g., *tensionability* [38] and *controllability* [39])

[4] The transposed Jacobian matrix of a cable-based parallel manipulator is usually denoted as the *structure matrix* in the Literature.

[5] In this work, a vector is defined as greater (lower) than **0** if *all* its components are greater (lower) than 0.

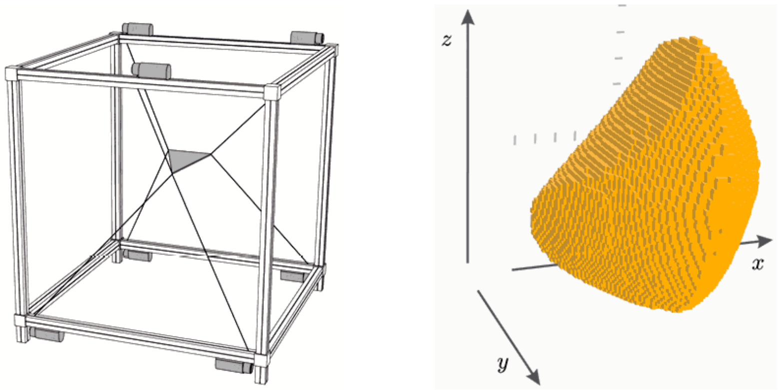

(a) (b)

Figure 1.6: Example of a spatial CRPM (a) and its controllable workspace (b) under a fixed load [43].

Discrete algorithms are generally unable to detect singularities and require higher computational times as the resolution of the grid is incremented. To overcome these issues, continuous algorithms based on the *interval analysis* have been recently proposed. A detailed review on these approaches is presented in [43].

Roughly speaking, motors number and locations must be chosen carefully, in order to achieve the desired controllable workspace: otherwise forces exertion will be strongly reduced both in magnitude and allowable directions, despite of the sizes of the motors and the number of cables. Besides workspace optimization and positioning accuracy, the control system may be another major issue, since cables must always be kept in tension. Cable interference and disturbances due to friction in *pulley-block*[6] rollers increase the complexity of the control architecture as well.

1.3 State of the Art

Many authors and research teams focused their attention on the analysis and synthesis of cable-based parallel devices. In the following, a brief description of the most important works is reported.

Y. Shen, H. Osumi and T. Arai presented early theoretical results on wire-driven and wire-suspended devices [40, 45]. They defined necessary and sufficient conditions for *manipulability* and used the *manipulability ellipsoid* along with a *set of manipulating forces* as performance indices.

M. Hiller and R. Verhoeven designed one of the pioneering prototypes of cable-based devices, employing both cables and rigid-link arms [4]. They also brought out a comprehensive theoretical study on tendon-based Stewart platforms [36, 1] (Fig. 1.7(a)), dealing with workspace characterization, force tension computation, kinematics and optimal trajectory planning. As a tool to inspect singularities, they introduced a stiffness matrix for cable based

---

[6] The term is used throughout this thesis to indicate a pulley and the set of devices required to control its position and the exerted torque (e.g., motor, gearboxes, idle pulleys, feedback sensors, etc.).

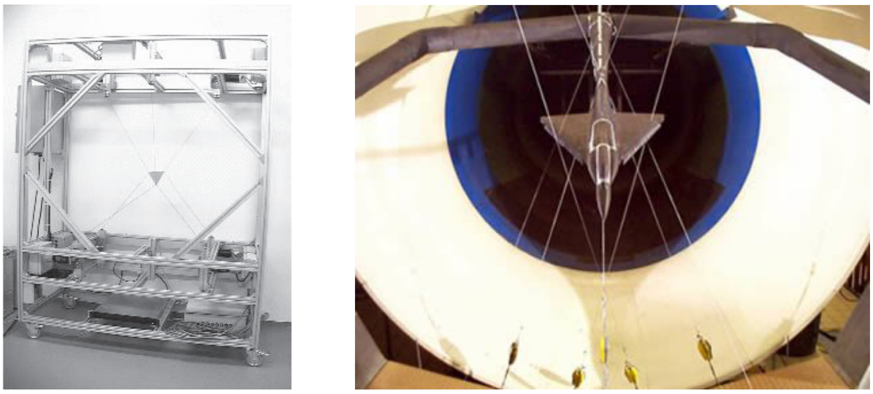
(a) (b)

Figure 1.7: The SEGESTA test bed developed at the University Essen-Duisburg [1] (a) and the SACSO project, developed at the French Aerospace Lab [44] (b).

systems.

R. L. Williams II and P. Gallina presented early studies on planar cable-based devices, dealing with layout optimization, kinematics, dynamics, optimal cable tension distribution and workspace estimation [46, 34, 47, 48]. In [28], Trevisani, Gallina, and Williams II introduced a novel design where a passive SCARA-type manipulator supports the EE of a planar CDDR against loading normal to the motion plane.

G. Rosati and P. Gallina introduced a *set of manipulability indices* for planar cable-driven robots, that allows to describe the isotropic force and moment exertion capabilities and the coupling between them by analyzing the properties of the structure matrix $\mathbf{A}$. By using those indices, the *maximum operational isotropic force* (i_F) and the *maximum operational isotropic moment* (i_M) can be evaluated separately. An additional index (i_I) was introduced to account for force and moment coupling[7]. The new indices were applied to assess the performances of a 3-DOF haptic interface called the Feriba3 [8, 37]. The same indices were generalized and employed in the design of a 5-DOF haptic display, called the PiRoGa-5 [49, 50]. Other works by the same authors involved the design of two cable-suspended machines for robot-assisted upper-limb rehabilitation of post-stroke patients: the NeReBot [51] and the MaRiBot [22]. The aforementioned devices will be described in detail in the next section.

P. Lafourcade and M. Llibre presented a graphical method for deriving the workspace of systems having 3 DOFs or less [52, 44]. The method is easily applicable to planar *point-mass* systems[8]. For non-point mass devices and systems with more than 3 DOFs, only approximate and partial results were obtained. This methodology was presented as a tool to help designers in early choices of a robot geometry, and was validated in the design of fully and over constrained devices for wind-tunnel simulations (Fig. 1.7(b)).

An extensive study on cable-based systems can be found in the works by S.K. Agrawal and coworkers. Several of them deal with mechanical design of cable suspended robots [9, 21].

---

[7] These indices will be described in detail in the next chapter

[8] Point-mass systems are those cable-based devices wherein all the cables are attached to a single point at the end-effector, thereby controlling only its translational movements.

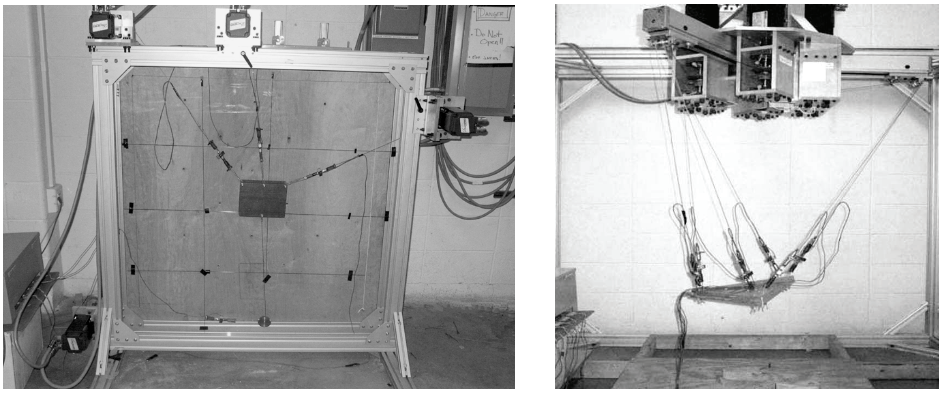
(a) (b)

Figure 1.8: The prototypes of cable-cased manipulators developed at the Mechanical Systems Lab., University of Delaware [9, 21].

In [9], for example, the GDI was successfully applied to compare different design solutions[9]. The authors used the GDI and the volume of the workspace as performance indices for the design optimization of a 6-DOF cable-suspended robot, driven by 6 cables. A discrete set of robot geometries were inspected for different orientations: though the computational time grew with the number of design parameters taken into account and their range of variability, it was shown that even a limited set of design variables allows to deduce significant trends, that can be successively exploited for solving a specific design problem. The same optimization method was later applied to cable-suspended planar devices [21]. The authors showed that weighting both the design criteria in a cost function usually lead to better design solutions. Recently, a work by H. Hadian and A. Fattah investigated the isotropic design of the 6-DOF device by applying both a symbolic and a numerical approach [54]. Besides design methods, S.R. Oh and S.K. Agrawal investigated several control approaches to make a manipulator follow prescribed trajectories while keeping all the cable tensions positive during motion [55].

S. Krut, O. Company and F. Pierrot pointed out some issues arising from the application of typical velocity performance indices - based on *Jacobian matrix* - to parallel mechanisms with actuation redundancy, and proposed the introduction of more significant indices, based on the *operational polytope* [58]. For this class of devices, they illustrated how the inverses of the singular values do not give the semi-axes of the largest ellipse belonging to the operational polytope. Hence, they proposed the introduction of more significant indices, based on the *operational polytope* (the ratio of the maximum velocity and the isotropic velocity) and on the actual largest ellipse (the ratio of the semi-axes). As for the force performance, the *maximum operational isotropic force* was recognized as a suitable index to characterize force capabilities [59]. More recently [35], M. Gouttefarde, and S. Krut proposed a 2-step numerical method

---

[9] The *Global Dexterity Index* (also referred to as *Global Conditioning Index*, GCI) is the inverse of the Jacobian condition number, averaged over the workspace. It was employed for the first time as a measure of the kinematic isotropy of robotic devices by Gosselin and Angeles [53]. The index is a common tool to quantify the robot accuracy and its capability to move the end-effector towards arbitrary directions. The GDI is described in detail in the next chapter, where a way to cope with non-homogeneous entries in the Jacobian matrix is also proposed.

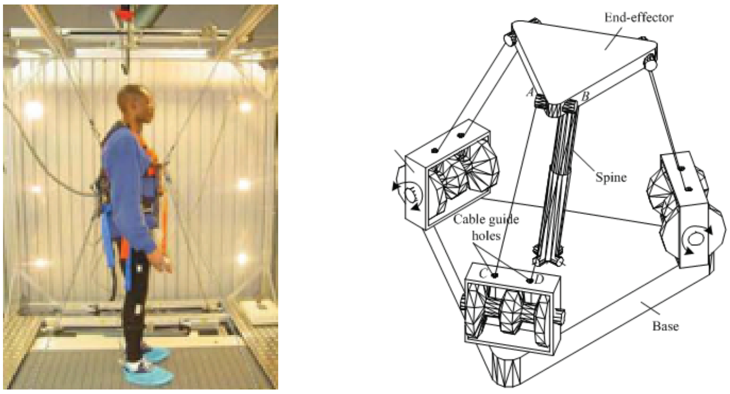

(a) (b)

Figure 1.9: The STRINGMAN [56] developed at the Fraunhofer IPK (a) and a concept drawing of the Betabot, designed at the University of Alberta [57] (b)

to find geometries of fully-constrained robots for which a given prescribed workspace is included in the *wrench-feasible workspace* (i.e., the robot wrench exertion capabilities satisfy some requirements inside a given spatial box). The peculiarities of the method consist in the use of a *"branch-and-prune"* algorithm that allows to explore the space of design parameters without a fixed discretization.

A. T. Riechel, P. Bosscher and I. Ebert-Uphoff worked on underconstrained cable-suspended robots, developing several parameters to analyze the wrench exertion capabilities of a device [42, 60]. Suppose a set of cable tension constraints are imposed: by first defining a geometrical method to calculate the set of wrenches a system is able to exert at the moving platform for a given configuration (NW_{avail}), one is able to specify regions of the task space that satisfy a given property, such as the possibility to apply a required wrench set or to carry a given payload. The same idea was extended to the dynamic case. Indeed, since wrenches are related to accelerations through the *Cartesian State Space equation*, regions of the task space wherein certain accelerations are reachable may be calculated as well. More recently, other performance indices of certain interest for cable suspended devices have also been inspected, such as a configuration-dependent measure of the robustness to external static and impulsive disturbances [61]. In [62], the authors investigated the relationship between *robot grasping* and manipulability of parallel cable-driven robots.

The advantage of Bossher and Ebert-Uphoff's approaches is to allow for a close-form description of the boundaries of the studied workspace. On the other hand, the formulations do not apply to non-underconstrained cable manipulators (i.e. arbitrary cable number and attachment points), and grow in complexity as the number of DOFs increases. Thus, in practice, the approaches are effective for simple devices only.

S. Khajepour and A. Behzadipour studied the *tensionability* condition for high-speed cable-based robots with translational DOFs [2, 57, 63] (Fig. 1.9(b)). In their designs, an active or passive varying-length link called *spine* is introduced between the base and the mobile platform to provide the ballast force that keeps the cables in tension. Also, the authors employed passive, fixed-length cables to constrain the motion of the end-effector.

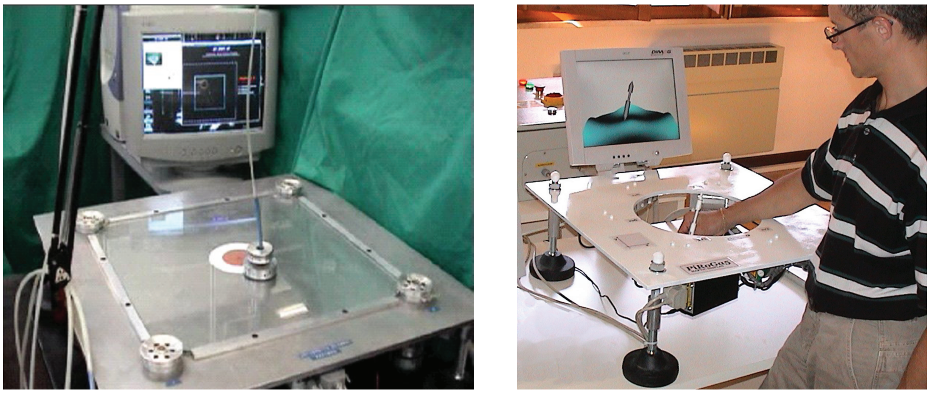
(a) (b)

Figure 1.10: The desktop-like, general-purpose haptic displays designed at DIMEG: Feriba3 [8, 37] (a) and Piroga5 [7, 65, 49] (b).

X. Diao and O. Ma studied systematic algorithms to derive the *force-closure workspace* of 6-DOF fully-constrained and over-constrained devices [39]. Following this approach, one must check an equivalent condition for *controllability*. The method consists in calculating vectors orthogonal to each set of 5 linearly independent columns of the structure matrix $\mathbf{A}$, and checking the signs of the projections of these vectors on the remaining columns. For a pose to be inside the *wrench-closure workspace*, those signs must be different.

D. Surdilovic and R. Bemhardt proposed a multi-objective design optimization method to design a cable-based robot for gait rehabilitation, based on the Jacobian condition number and on the homogeneity of the kernel. The method was validated through the development of the cable-based robot prototype for gait rehabilitation [56, 64] shown in Fig. 1.9(a).

1.4 Cable-based devices at DIMEG

In this Section, the robotic devices developed at the Robotics, Mechatronics and Rehabrobotics Labs of DIMEG (Dept. of Innovation in Mechanics and Management, University of Padua, Padua, Italy) are introduced.

1.4.1 General-purpose haptic displays

The Feriba3 [8, 37], depicted in Fig. (1.10(a)), is a 4-wire planar CRPM with a circular end-effector and a square-shaped workspace. It was designed to be used as a general-purpose haptic display, i.e., a device capable of reproducing real and virtual environments by exerting a variable mechanical impedance to the user's hand. It exploits 4 driven cables to generate 3 generalized forces on a round-shaped end-effector. The end-effector position is imposed by the operator, who perceives the force-feedback from the device. The direction and amount of force reflected depends on end-effector position and on the specific remote or virtual environment represented.

Each wire is fixed to the lateral side of the circular end-effector (named spool) and can wind around the end-effector. The other end of the wire is wound around a pulley, that is directly keyed on the shaft of a DC motor. Each pulley-block provides tension in the corresponding cable up to $f_{\max} = 10$N. The motors are mounted on a steel base at the vertices of a square ($l = 450$mm). The spool consists of a lower disc-shaped base and an upper circular handle that are connected by means of a universal joint, so as to avoid transmission of dumping moments. To minimize the spool friction, a sheet of glass is fixed on the base and a flux of compressed air is blown towards the glass through a series of little holes drilled in the lower side of the spool. This solution, together with the selection of low rolling-friction motors, aims to reduce the mechanical impedance perceived at the end-effector, thus improving the *haptic transparency* obtained at the end-effector. The base of the end-effector and the pulleys have the same winding radius $r = r_p = 30$mm: this feature ensures a simple, closed-form forward kinematic algorithm, avoids cable/end-effector interferences and has favorable consequences on the performances of the device, since two force components and one moment can be generated independently on the end-effector, regardless its position in the working space.

PiRoGa5 is a cable-driven 5-DOF haptic display, with a pen-like shaped end-effector [7, 65, 49]. Six wires are attached to the end-effector, three to each end-point of the pen (Fig. 1.10(b)). Each wire is tensioned by a motor-pulley direct drive system. Pulley radius is 15mm: this value represents a trade off between the maximum force each wire can exert and the transparency of the haptic display. The operator is able to move the end-effector along six DOFs; nevertheless, the control system is able to apply only five generalized forces to the pen (three forces and two torques), since wire configuration prevents the system from generating any torque along the pen axis. Each wire is forced to pass trough a PTFE eye-bolt: odd and even eye-bolts belong to two different parallel planes. On each plane, the three corresponding connections to the ground represent the vertexes of an equilateral triangle.

The force generated by the three wires connected to the each extremity of the pen belongs to the pseudo-pyramid formed by the same wires: hence, the total wrench acting on the end-effector is given by the composition of two such forces. Accurate machining leads one to consider the three wires meeting on the pyramid vertex, so that forward kinematics and wire tension computation can be carried out in closed form.

The wire-driven architecture leads to a very simple and light mechanical structure, low costs and high transparency. The main drawback is that with six actuators, only five generalized forces can be generated on the end-effector. Correspondingly, the control system is not able to detect end-effector orientation along its main axis.

1.4.2 Robots for the rehabilitation of the upper-limb

Both the Feriba3 and the Piroga5 were not specifically conceived for rehabilitation purposes, and were used for laboratory tests, both in the field of haptic teleoperation and in the simulation of virtual environments. In the following, three cable-based devices specifically conceived for the treatment of post-stroke patients will be discussed: the NeReBot, the MariBot and the Sophia-4.

The NeReBot (NEuro REhabilitation roBOT) employs 3 cables to sustain and move the forearm of the patient during the rehabilitation treatment. The device is easily transportable,

(a) (b)

Figure 1.11: The 3D wire-based rehabilitation devices designed at DIMEG: NeReBot [66, 51] (a) and MariBot [22, 67] (b).

and represents a good compromise between robot simplicity and range of motion.

The NeReBot is shown in Fig. (1.11(a)). The robot is composed of a wheeled base and a manually adjustable overhead structure, from which the wires originate. Three driven wires are used to sustain a splint on which the forearm of the patient is fastened [66, 51]. The exercise can be recorded by using a very simple *teaching-by-showing* procedure: the therapist moves the patient's arm through a set of via-points, which are recorded by the machine (*learning phase*); after this, the control system generates joint-interpolated trajectories for the three motors which control the wires. As a result, a very smooth and comfortable motion of the upper arm is obtained (*therapy phase*) [10].

The arm trajectories obtained with the NeReBot have been evaluated by developing a simulation tool addressing the static interaction between the human arm and the robot. By extensively using this simulation tool, a set of optimal configurations of the adjustable overhead structure has been identified. In this way, machine set-up can be optimized according to the specific rehabilitation exercise [51, 68].

This device was tested in two randomized controlled trials (RCT) that gave encouraging clinical results [69, 51, 70]. These results also demonstrated that even a simple, low-cost transportable machine can be very effective in the rehabilitation of post stroke patients.

Some limitations of the NeReBot came up during first clinical trials. Mainly, since the wires originate from a fixed overhead structure, the NeReBot has a good vertical range of motion, but less control of movements in the horizontal plane. To overcome this and other limitations of the first prototype, a new machine was developed, named MariBot [22, 67].

The MariBot (MARIsa roBOT) is shown in Fig. (1.11(b)). The basic principles from which the NeReBot was designed were maintained. However, the manually adjustable overhead structure was replaced with a controlled 2-DOF serial robotic arm. In this way, wire configuration can be changed during therapy, according to the horizontal motion of the up-

---

[10] During NeReBot-assisted therapy, the upper limb of the patient is a 5-DOF kinematic chain constrained by three unidirectional actuators only. Hence, the whole system still have 2 DOF [68]. This gives a very good sensation to the patient, who never feels to be restrained by the machine.

Figure 1.12: The first planar cable-based rehabilitation device developed at DIMEG: Sophia-4 [72, 73].

per limb of the patient. As a result, the working space was improved, encompassing nearly the whole range of motion of the human arm. Moreover, the MariBot does not need to be set-up before the beginning of therapy. Also, the weight of the robot has been reduced significantly, by using a commercial lifting device as base structure to build the robot. The MaRiBot is currently undergoing lab tests and clinical trials will start in the next future.

Sophia-4 (String Operated Planar Haptic Interface for the Arm-rehabilitation) was conceived for the rehabilitation of chronic patients, and came up as an evolution of the general-purpose haptic display FeRiBa3.

The prototype is depicted in Fig. 1.12. Two major aspects were considered in the early design of the device: workspace shape and force capabilities. The dimensions of the workspace were calculated considering the dimensions of the patient's body [71] and his/her sitting posture. The length of the lower base of the trapezoidal layout was determined based on the average shoulder distance of adult males, thus allowing the patient to lean his/her elbows outside the lower pulley-blocks during robot therapy. The manipulability index i_F was employed to adjust the force capabilities of the machine to the requirements [72, 73].

A commercial office table constitutes the mechanical structure of Sophia-4. The patient, while sitting on a wheelchair, holds a handlebar-grip that can be moved over a flat horizontal surface, sliding on low-friction PTFE discs. Four nylon cables are used to exert forces at the end-effector, each having one end fixed to a point on the axis of the grip, and the other directly keyed to a direct-drive pulley. Pulley-blocks which can spin around a vertical axis are used to pass cables underneath the table surface, where the DC motors are mounted. The cables are all attached to a single point of the end-effector, so the device is capable of exerting only horizontal pure forces on the patient's hand. The handlebar-grip itself is mounted on the base of the end-effector by means of a ball bearing, in such a way that no moment can be transmitted to the patient's hand along the vertical axis.

A real-time high-level controller manages the type of assistance to be given to the patient, while a low-level controller is responsible for kinematics, force distribution algorithms and surveillance routines [74, 73]. The therapy consists of point-to-point reaching tasks.

1.4.3 Adaptive cable-based systems and Sophia-3

The *main goal* of this thesis consists in the design and development of Sophia-3. Sophia-3 represents a further evolution of the *desktop-like device* concept initiated with Feriba3. Sophia-3 guarantees comparable force performances as those of Sophia-4, while employing only 3 cables (i.e., the minimum number of cables that guarantees manipulability).

The device has been developed following the novel design approach described in Chapter 3 [75]. The main idea relies on the introduction of one or more moving pulley-blocks to optimize cable configuration according to the current end-effector position. By properly moving the pulley-block(s), the workspace can be on-line modified to always keep the end-effector in a convenient subset of the working space, thus enhancing robot capabilities without the need for additional cables. Installing only one moving pulley-block proved to be the better compromise between force performances and reduction of design complexity. Additionally, it has been shown that this *Semi-adaptive* configuration leads to further advantages, even over the standard 4-cable configuration, in terms of compactness, workspace exploitation, cable interference, perceived mass, power dissipation and position accuracy [76].

Starting from these observations, the novel design was developed, with the aim of introducing the aforementioned advantages, while still keeping comparable force capabilities. In addition, a new degree of freedom was introduced to allow table rotation around a longitudinal axis: this solution has partially overcome one of the limitations of Sophia-4, i.e., the impossibility to train the patient's shoulder as much as the 3D devices do. A detailed description of Sophia-3 is reported in Chapter 4 and Chapter 5.

Chapter 2

Performance Assessment of Cable-based Devices

This chapter deals with performance analysis of cable-based parallel devices, as described by a set of local, configuration-dependent indices that focus on the key features of a given design. The specificity of this class of robotic systems, primarily due to the unilateral actuation, imposes to adopt new tools for evaluating force exertion capabilities and power consumption under static conditions. Kinematic dexterity and equivalent inertia are addressed as well, by adapting common tools borrowed from rigid-link robotics. Although numerical algorithms allow to apply these indices to any cable-based device, in this section we deal with spatial and planar CRPMs, which allow close-form formulations.

The set has been conceived as an integrated tool for the analysis and the design optimization of new devices. Reducing the number of optimization parameters plays a role in simplifying the algorithms, therefore, non-dimensional indices are employed. In the following analysis, cables are assumed to be ideal (i.e., infinitely stiff with negligible mass.). The effectiveness of the approach is validated by applying the set to three layouts of planar CRPM, each corresponding to a real prototype developed in the past years.

2.1 Manipulability indices for CRPMs

Examples of commonly adopted performance parameters used in robotics are: workspace size, perceived mass, acceleration capabilities, accuracy, force magnitude, isotropy and bandwidth. As far as cable-driven systems are concerned, most of the mechanical components are low weight (no rigid links are employed), motors are usually direct-driven and friction can be kept down through a wise design: as a consequence, the perceived mechanical impedance is small. Hence, for cable-driven devices, force capabilities are generally recognized as being more crucial than inertial properties [77]

A main issue when designing a cable-based system is to guarantee the *manipulability* of its end-effector [37]. Robot manipulability, as originally defined by Yoshikawa [78] and Sciavicco and Siciliano [79], is a measure of the performances of a robotic structure. This definition has been partially revised for wire-driven systems, since the wire-actuation is unilateral (Shen, Osumi, and Arai [40]).

A set of *manipulability indices* has been defined in the last years. In this section, we briefly recall some of the results on the *manipulability* condition for *completely restrained* designs (CRPMs, see Chapter 1.2 for a definition). These results are based on the works of Gallina & Rosati on planar CRPMs [37], which have been recently extended to any CRPM [49] by Rosati & Zanotto.

To fix the ideas, let us first introduce the form of the force equilibrium equation for a planar mobile platform driven by n cables. With the notation shown in Fig. 2.1, the three generalized forces exerted by the cables on the platform are:

$$F_x = \sum_{i=1}^{n} f_i u_{ix}, \quad F_y = \sum_{i=1}^{n} f_i u_{iy}, \quad M_z = \sum_{i=1}^{n} f_i \left(\mathbf{r}_i \wedge \mathbf{u}_i\right) \cdot \mathbf{k} = \sum_{i=1}^{n} f_i c_i \tag{2.1}$$

where $\mathbf{k}$ is the unit vector orthogonal to the plane of motion and $c_i = \left(\mathbf{r}_i \wedge \mathbf{u}_i\right) \cdot \mathbf{k}$. Thus, the equilibrium may be rewritten in matrix form as:

$$\mathbf{F} = \mathbf{A}\mathbf{f}$$

$$\mathbf{F} = \begin{bmatrix} F_x \\ F_y \\ M_z \end{bmatrix}, \quad \mathbf{A} = \begin{bmatrix} u_{1x} & \dots & u_{nx} \\ u_{1y} & \dots & u_{ny} \\ c_1 & \dots & c_n \end{bmatrix}, \quad \mathbf{f} = \begin{bmatrix} f_1 \\ \dots \\ f_n \end{bmatrix} \tag{2.2}$$

Equation (2.2) is addressed as the *wrench-closure equation* in the related Literature. Clearly, the so-called *structure matrix* $\mathbf{A}$ coincides with the transpose of the Jacobian matrix of the manipulator. Following a similar approach, the structure matrix for a generic 3D cable-based system can be derived.

Let us consider a m-DOF system, driven by $n = (m+1)$ wires. The system possesses the minimum number of cables necessary to guarantee *manipulability*, and is thereby defined as completely restrained (CRPM). The following theorem gives three equivalent conditions for manipulability:

Theorem 2.1.1. *Let* $\mathbf{A} \in \mathbf{M}_{m \times n}(\mathbf{R})$, $\operatorname{rank}(\mathbf{A}) = m$, *let* $h_i = (-1)^{i+1} \det(\mathbf{A}_i)$ *be the* i*-th* m*-order algebraic minor of* $\mathbf{A}$, *where* $\mathbf{A_i} \in \mathbf{M}_{m \times m}$ *is the submatrix of* $\mathbf{A}$ *obtained by deleting the* i*-th column of* $\mathbf{A}$; *the following facts are equivalent:*

(i) for any $\mathbf{F} \in \mathbf{R}^m$, *there exists a vector* $\mathbf{f} \in \mathbf{R}^{m+1}$ *such that* $\mathbf{A}\mathbf{f} = \mathbf{F}$;

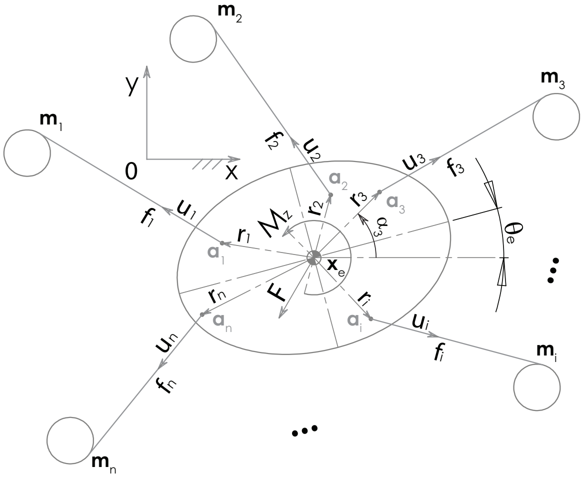

Figure 2.1: Sketch of a planar CRPM.

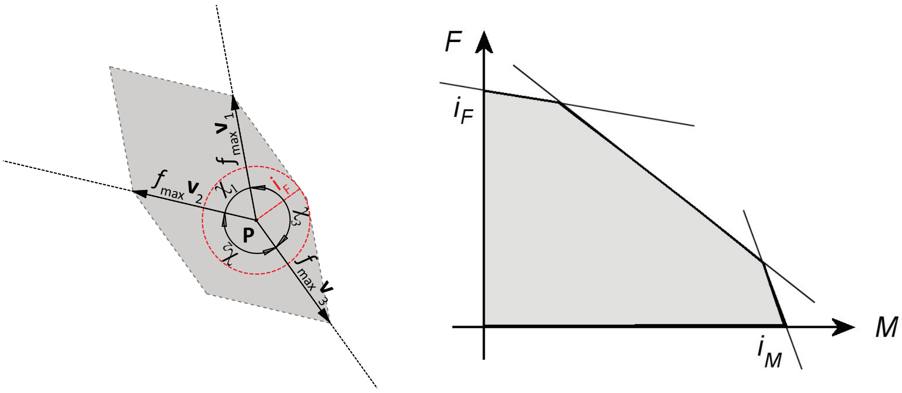

(a) (b)

Figure 2.2: Set of feasible wrenches for a planar translational CRPM and geometric interpretation of the maximum allowable isotropic force (a). Coupling effect between isotropic forces and isotropic moments for a generic CRPM (b), [49].

(ii) *there exists a vector* $\boldsymbol{\alpha} \in \mathbf{R}^{m+1}$, $\boldsymbol{\alpha} > \mathbf{0}$ *such that* $\boldsymbol{A\alpha} = \mathbf{0}$*;*

(iii) *vector* $\mathbf{h} = \left\{ \begin{array}{ccc} h_1 & \ldots, & h_{m+1} \end{array} \right\}^T$ *is such that* $(\mathbf{h} < \mathbf{0}) \vee (\mathbf{h} > \mathbf{0})$

The theorem, which has been demonstrated in [37], provides a method to compute the *statics workspace* of a device: once the analytical expression of the structure matrix has been derived in terms of the design parameters, condition *(iii)* is imposed on vector $\mathbf{h}$, thus obtaining $(m+1)$ inequalities involving the disposition of cables. The set of end-effector poses for which these conditions are satisfied constitutes the *statics workspace* of the device.

The definition of statics workspace relies on geometrical considerations only. However, due to motor torque capabilities, each component f_i of vector $\mathbf{f}$ is constrained by an upper bound $f_{\max}$, so that a limited set of vectors $\mathbf{F}$ is to be expected at the end-effector, even though it lays inside the statics workspace[1]. Thus, *manipulability indices* are introduced to describe the actual force capabilities of a device.

As far as point-mass end-effectors are concerned, only pure forces can be exerted, thus, a single parameter can conveniently be adopted, which is the module of the maximum feasible isotropic force. The derivation of this index is straightforward in the case of planar *translational* CRPMs. Let us consider the system shown in Fig. 2.2(a): the polygon that describes all the feasible forces at a given position is obtained by drawing along each cable a vector representing the cable maximum tension $\mathbf{f}_{\max}$, and two lines passing by the tip of that vector, parallel to the remaining cables. Clearly, the maximum isotropic force is given by the radius of the circle centered in P and tangent to the polygon. Since cable configuration varies as a function of end-effector position, different values are to be expected throughout the workspace.

A different approach must be applied in the case of more complex CRPMs, which accounts for generic wrenches (i.e. force/moment combinations). Two dedicated performance

---

[1] Although a lower bound $\mathbf{f}_{\min} > \mathbf{0}$ should also be considered, in order to prevent cable slackening during motor shaft accelerations, in the computation of the manipulability indices, this aspect is neglected.

indices have been introduced to address pure force and pure moment capabilities[2], furthermore, since forces and moments are coupled to the wire tensions, an additional index is introduced, that deals with the system aptitude to independently generate forces and moments.

Assume that the end-effector is laying inside the workspace, and let M be the magnitude of an arbitrary pure moment that can be attained in any available direction. Since cable tensions are upper bounded, for a moment of magnitude M acting in a given direction, only a limited set of forces can be exerted and, specifically, a maximum isotropic force. Therefore, by checking all the possible directions for the moment M and taking the minimum magnitude of the isotropic forces calculated for each direction, the value of F can be derived. Repeating this approach for different values of M gives the plot of $F = g(M)$, which yields the maximum isotropic force that can be obtained at fixed values of moment (Fig. 2.2(b)). Based on this function, the following indices have been defined:

$$i_F = \max(F)\,; \quad i_M = \max(M)\,; \quad i_i = \frac{1}{i_F i_M}\int_0^{i_M} f(M)\,dM \tag{2.3}$$

It can be proved that the maximum of F is obtained as the moment M is kept null, and vice-versa. The last index accounts for the aptitude of the system to independently generate forces and moments: the more i_I approaches the unity, the more the forces and the moment are uncoupled. Under the assumption that all the cables are subjected to the same tension constraints $0 \leqslant f_i \leqslant f_{\max}$, the estimation of these indices is straightforward. Indeed, an analytical formulation have been derived in [49] which applies to any CRPM[3].

Additionally, it has been shown that both i_F and i_M are directly proportional to $f_{\max}$, whereas i_I is independent of $f_{\max}$. Thus, for estimating the force exertion capabilities of a given layout, we employ the following modified *non-dimensional* set: $i_F/i_{F,\max}$, $i_M/i_{M,\max}$, i_I. where $i_{F,\max}$ and $i_{M,\max}$ are the maximum values of i_F and i_M obtainable with a CRPM having the same number of cables n. All the parameters range from 0 to 1 and are independent of $f_{\max}$. Therefore, they may be used to objectively compare the layouts of devices that are characterized by different values of $f_{\max}$. Notice that, by using this approach, the force capabilities depends on the geometric layout only, and can therefore be determined in the early design steps.

2.2 Power dissipation index

Because of Joule heating, each DC motor dissipates an amount of power that is proportional to the square of the current flowing through the winding resistance. In addition, the current is proportional to the exerted torque, with $1/k_\tau$ (i.e., the inverse of the torque constant) being the proportionality constant. Under the *pseudostatic* hypothesis, the torque equals the product of the pulley radius and the tension in the corresponding cable, thus, for a cable-based

---

[2] In principle, heterogeneous quantities can be handled by introducing a linear mapping, based on the inertial properties of the end-effector, that maps wrenches to vectors with linear units only [61]. Actually, this approach has been applied for the isotropy indices described later, where the focus is on determining how far a device is from an isotropic configuration. However, as far as the assessment of force capabilities is concerned, a more effective method lies in considering forces and moments separately.

[3] The approach was first formulated in [37] for planar CRPMs, and later generalized to any CRPM in [49].

device with n identical tensioning motors, the total amount of dissipated power is proportional to the squared Euclidean norm of the wire tension vector $\mathbf{f}$:

$$P = c\sum_{i=1}^{n} f_i^2 = c\|\mathbf{f}\|^2 \tag{2.4}$$

where the constant c depends on the pulley-block characteristics.

During operation, a minimum tension $f_{\min}$ must always be maintained to avoid cable slackening. Hence, the power dissipated in static conditions may be considerable, even when the applied wrench is zero, especially when the end-effector pose is approaching the boundary of the statics workspace.

The value of P (computed at a given pose, in static equilibrium and for $\mathbf{F} = \mathbf{0}$) has already been used as a performance index in [76]. Instead, in this work a modified index is employed, which depends on matrix $\mathbf{A}$ and on the ratio $f_{\max}/f_{\min}$ only. To define such an index, a criterion must first be decided for solving the force equilibrium $\mathbf{A}\mathbf{f} = \mathbf{F}$. Since $\operatorname{nullity}(\mathbf{A}) = 1$ for a manipulable CRPM, the *minimum-norm* feasible solution is straightforward to derive. Let us consider a CRPM with n cables and a manipulable end-effector: because of the manipulability condition stated in Theorem 2.1.1, there exists a vector $\boldsymbol{\alpha} > \mathbf{0}$ s.t. $\ker(\mathbf{A}) = \langle\boldsymbol{\alpha}\rangle$. If we take into account the lower constraints $f_i \geqslant f_{\min}$, then the *minimum-norm* feasible solution $\mathbf{f}_0$ that satisfies $\mathbf{A}\mathbf{f}_0 = \mathbf{0}$ is:

$$\tilde{\mathbf{f}}_0 = f_{\min}\left(\frac{\boldsymbol{\alpha}}{\min\limits_{i=1..n}(\alpha_i)}\right) \tag{2.5}$$

If also the upper constraints are taken into account, then a feasible solution does exist only if $\tilde{\mathbf{f}}_0$ already satisfies the upper constraints. If this is not the case, static equilibrium can still be achieved by neglecting the lower constraints and by scaling $\tilde{\mathbf{f}}_0$, therefore:

$$\mathbf{f}_0 = \begin{cases} \tilde{\mathbf{f}}_0 \quad \text{if} \quad \tilde{\mathbf{f}}_0 \leqslant f_{\max} \\ f_{\max}\left(\dfrac{\tilde{\mathbf{f}}_0}{\max\limits_{i=1..n}(\tilde{f}_{0,i})}\right) = f_{\max}\left(\dfrac{\boldsymbol{\alpha}}{\max\limits_{i=1..n}(\alpha_i)}\right) \quad \text{otherwise} \end{cases} \tag{2.6}$$

Assuming the force-distribution criterion described by (2.5) and (2.6), the power dissipation index is defined as the ratio between the actual dissipated power P (at a given pose, in static equilibrium and for $\mathbf{F} = \mathbf{0}$) and the minimum allowable power dissipation $P_{\min}$:

$$P/P_{\min} = \|\mathbf{f}_0\|^2/\left(n f_{\min}^2\right), \quad \mathbf{f}_0 \in \mathbb{R}^n : \mathbf{A}\mathbf{f}_0 = \mathbf{0}_{m\times 1} \tag{2.7}$$

Thus, similarly to the non-dimensional *manipulability indices* described in the previous section, the power dissipation index depend mainly on the geometric characteristics of the device (i.e., on the matrix $\mathbf{A}$). In this case, however, a value for the ratio $f_{\max}/f_{\min}$ must be set as well.

2.3 Dexterity index

Let us consider the *reverse kinematics* equations for a cable-based device. The length of each wire is computed by calculating the Euclidean distance between the attachment point to the ground and the corresponding attachment point at the mobile platform (see Fig. 2.1):

$$\begin{gathered} l_i = d\left(\mathbf{a}_i, \mathbf{x}_{mi}\right) = d\left(\mathbf{x}_e + \mathbf{r}_i, \mathbf{x}_{mi}\right); \\ \mathbf{x}_e = \begin{bmatrix} x_e \\ y_e \end{bmatrix}; \quad \mathbf{r}_i = r \begin{bmatrix} \cos\left(\alpha_i + \theta_e\right) \\ \sin\left(\alpha_i + \theta_e\right) \end{bmatrix}; \end{gathered} \tag{2.8}$$

After differentiating the first one of (2.8) we get:

$$\delta l_i = \frac{\partial l_i}{\partial x}\delta x + \frac{\partial l_i}{\partial y}\delta y + \frac{\partial l_i}{\partial \theta_e}\delta\theta_e \tag{2.9}$$

Which can be rewritten for all the cables in a more convenient matrix form as:

$$\delta\mathbf{l} = \begin{bmatrix} \delta l_1 \\ \dots \\ \delta l_n \end{bmatrix} = \begin{bmatrix} \frac{\partial l_1}{\partial x} & \frac{\partial l_1}{\partial y} & \frac{\partial l_1}{\partial \theta_e} \\ \dots & \dots & \dots \\ \frac{\partial l_n}{\partial x} & \frac{\partial l_n}{\partial y} & \frac{\partial l_n}{\partial \theta_e} \end{bmatrix} \begin{bmatrix} \delta x \\ \delta y \\ \delta\theta_e \end{bmatrix} = \mathbf{A}^T \delta\mathbf{x} \tag{2.10}$$

Finally, after dividing (2.10) by the infinitesimal dt, the following expression is obtained, which relates the vector of task space velocities $\dot{\mathbf{x}}$ to the vector of the pulley angular velocities $\dot{\boldsymbol{\theta}}_p$:

$$r_p \dot{\boldsymbol{\theta}}_p = \mathbf{A}^{\mathrm{T}} \dot{\mathbf{x}} \tag{2.11}$$

where r_p is the pulley radius. For the manipulator depicted in Fig. 2.1, $\dot{\mathbf{x}}$ and $\dot{\boldsymbol{\theta}}_p$ take the following form[4]:

$$\dot{\boldsymbol{\theta}}_p = \begin{bmatrix} \dot{\theta}_{p1} \\ \dots \\ \dot{\theta}_{pn} \end{bmatrix} \quad \dot{\mathbf{x}} = \begin{bmatrix} \dot{x} \\ \dot{y} \\ \dot{\theta}_e \end{bmatrix} \tag{2.12}$$

Equations (2.2) and (2.11) show the role of $\mathbf{A} = \mathbf{J}^{\mathrm{T}}$ in mapping joint forces to Cartesian forces and Cartesian velocities to joint velocities.

Kinetostatic parameters based on the *pseudo-inverse* of the Jacobian matrix are often used to evaluate the performances of rigid link manipulators. By mapping through this matrix the unit hypersphere of joint velocities into the operational-space, the *velocity manipulability ellipsoid* is derived, which expresses the ease of arbitrarily changing the position and orientation of the end-effector in a given configuration. Yoshikawa introduced a manipulability measure given by the product of the singular values of $\mathbf{A}$, and proposed the inverse of the Jacobian condition number as a measure of the kinematic isotropy of a mechanism [80], Gosselin and Angeles used the same parameter to define a *global dexterity index* (GDI) for the kinematic optimization of robotic manipulators [53]. Shen et al. [40] applied Yoshikawa's manipulability index to cable-driven devices. Several authors employed the GDI in conjunction with other indices to identify the optimal design of planar cable-based devices (Agrawal [21], Li [81]). To the best of the author's knowledge, this work presents for the first time a local description of the dexterity of planar CRPMs.

When the end-effector possesses both translational and rotational DOF, the Jacobian matrix shows dimensional inhomogeneity, and the value of the condition number depends on

---

[4] If we use the notation in (2.2) for the structure matrix, (2.11) holds true if $\dot{\theta}_p > 0$ causes a reduction in the length of unrolled cable

the choice of units. This issue can be addressed by dividing the entries of the matrix corresponding to rotational DOF by a conventional length. In principle, the choice of the normalizing length is not unique. However, by using the *characteristic length* (i.e., the length that minimizes the condition number of the normalized matrix [82, 83, 84]), the singular values are equal in the isotropic configurations.

Let us consider a generic planar device driven by n cables (Fig. 2.1), thereby the structure matrix $\boldsymbol{A}$ takes the form shown in (2.2). By dividing the last row of $\boldsymbol{A}$ by L_A, the normalized matrix $\bar{\mathbf{A}}$ is obtained.

$$\bar{\mathbf{A}} = \mathbf{D}_{\mathrm{A}}\mathbf{A}; \quad \mathbf{D}_{\mathrm{A}} = \mathrm{diag}\left(1,\ 1,\ \frac{1}{L_{\mathrm{A}}}\right) \tag{2.13}$$

The singular values of $\bar{\mathbf{A}}$ can be derived as the square roots of the eigenvalues of $\bar{\mathbf{A}}\bar{\mathbf{A}}^T$; then, the inverse of the matrix condition number $\kappa\left(\bar{\mathbf{A}}\right)^{-1}$ is computed.:

$$\bar{\mathbf{A}}\bar{\mathbf{A}}^T = \begin{bmatrix} \sum\limits_{i=1}^{n} \mathbf{u}_i\mathbf{u}_i^T & \sum\limits_{i=1}^{n} c_i\mathbf{u}_i/L_{\mathrm{A}} \\ \sum\limits_{i=1}^{n} c_i\mathbf{u}_i^T/L_{\mathrm{A}} & \sum\limits_{i=1}^{n} c_i^2/L_{\mathrm{A}}^2 \end{bmatrix} \tag{2.14}$$

We now derive the value of L_A by imposing the condition of isotropy $\bar{\mathbf{A}}\bar{\mathbf{A}}^T = \sigma^2\mathbf{I}_3$, thus obtaining the following constraints on the six independent entries of the matrix:

$$\begin{array}{lll} \sum\limits_{i=1}^{n} u_{ix}^2 = \sigma^2; & \sum\limits_{i=1}^{n} u_{iy}^2 = \sigma^2; & \sum\limits_{i=1}^{n} c_i^2/L_{\mathrm{A}}^2 = \sigma^2; \\ \sum\limits_{i=1}^{n} u_{ix}u_{iy} = 0; & \sum\limits_{i=1}^{n} c_i u_{ix}/L_{\mathrm{A}} = 0; & \sum\limits_{i=1}^{n} c_i u_{iy}/L_{\mathrm{A}} = 0; \end{array} \tag{2.15}$$

To find L_A, it is sufficient to consider the three equations appearing in the first row of (2.15). Indeed, by summing the fist equation to the second one and then substituting into the third one, we get:

$$L_{\mathrm{A}} = \sqrt{\frac{2}{n}\sum_{i=1}^{n} c_i^2} \tag{2.16}$$

Equations (2.15) also allow to derive the isotropic configurations of a device. However, as it will be clear in the example included at the end of this chapter, the isotropic configurations must be calculated separately for each specific design.

2.4 Inertial isotropy index

The inertial isotropy of a manipulator can be efficiently investigated through the eigenvalue analysis of the Cartesian mass matrix $\boldsymbol{\Lambda}$. H. Asada [85] first used the *General Inertial Ellipsoid* (GIE) derived from the quadratic form associated with the task-space mass matrix as a generalization of the inertia ellipsoid of a single rigid body, and applied it to the design of serial manipulators with only translating end-effector. As for manipulators with both translational and rotational DOFs, O. Khatib [86] proposed a decomposition of the Cartesian mass matrix into three submatrices to overcome the inhomogeneity in the matrix entries.

In previous works [76, 72], we proposed for the first time the use of the condition number $\kappa(\mathbf{\Lambda})$ to assess the inertial properties of planar cable-based devices with only translational DOFs. More recently, we extended the derivation of this index to any planar device [87], by using the characteristic length L_Λ to overcome inhomogeneity issues.

The Cartesian mass matrix $\mathbf{\Lambda}$ may be derived from the *Cartesian state space equation*. Let consider a planar device driven by n wires (Fig. 2.1): by taking twice the time-derivative of (2.11), the following equation is obtained:

$$\ddot{\boldsymbol{\theta}}_p = \frac{1}{r_p}\mathbf{A}^{\mathrm{T}}\ddot{\mathbf{x}} + \frac{1}{r_p}\frac{d\mathbf{A}^{\mathrm{T}}}{dt}\dot{\mathbf{x}} \tag{2.17}$$

If friction is negligible, the equation that describes the dynamics of the n pulley-blocks (supposed identical for simplicity) is:

$$\mathbf{f} = \frac{1}{r_p}\boldsymbol{\tau} - \frac{I_p}{r_p}\ddot{\boldsymbol{\theta}}_p \tag{2.18}$$

where $\boldsymbol{\tau}$ is the vector of motor torques and I_p is the moment of inertia of the pulley block around the axis of rotation. On the other end, the dynamics of the end-effector is yielded by:

$$\mathbf{F} = diag\left(m_e, m_e, I_{eG}\right)\ddot{\mathbf{x}} \tag{2.19}$$

Where m_e is the end-effector mass and I_{eG} is its moment of inertia w.r.t. the axis orthogonal to the plane of motion, passing through the CoM. Now, as far as each cable is in tension, (2.2) can be used to link the dynamics of the pulley blocks to the dynamics of the end-effector[5]. After substituting (2.17) into (2.18), the expression of $\mathbf{f}$ is introduced into (2.2) and the resulting $\mathbf{F}$ is finally plugged into (2.19) to get the *Cartesian state space equation*:

$$\begin{gathered}\mathbf{\Lambda}\ddot{\mathbf{x}} + \mathbf{N}\dot{\mathbf{x}} = \frac{1}{r_p}\mathbf{A}\tau \\ \mathbf{\Lambda} = m_e\mathrm{diag}\left(1, 1, \rho_e^2\right) + j\mathbf{A}\mathbf{A}^{\mathrm{T}}; \quad \mathbf{N} = j\mathbf{A}\frac{d\mathbf{A}^{\mathrm{T}}}{dt}\end{gathered} \tag{2.20}$$

with ρ_e being the end-effector *radius of gyration* around an axis orthogonal to the plane of motion which passes through the CoM, and $j = I_p/r_p^2$ the pulley-block equivalent mass as perceived at the cable.

In order to compute how far a device is from inertial isotropy, the last row of $\mathbf{\Lambda}$ is divided by the squared characteristic length L_Λ^2:

$$\bar{\mathbf{\Lambda}} = \mathbf{D}_\Lambda\Lambda\mathbf{D}_\Lambda; \quad \mathbf{D}_\Lambda = \mathrm{diag}\left(1,\ 1,\ \frac{1}{L_\Lambda}\right) \tag{2.21}$$

As in the previous section, to compute L_Λ, we impose the condition of isotropy:

$$\bar{\mathbf{\Lambda}} = m_e\,\mathrm{diag}\left(1, 1, \rho_e^2/L_\Lambda^2\right) + j\begin{bmatrix}\sum_{i=1}^{n}\mathbf{u}_i\mathbf{u}_i^T & \sum_{i=1}^{n}c_i\mathbf{u}_i/L_\Lambda \\ \sum_{i=1}^{n}c_i\mathbf{u}_i^T/L_\Lambda & \sum_{i=1}^{n}c_i^2/L_\Lambda^2\end{bmatrix} = \sigma_\Lambda\mathbf{I_3} \tag{2.22}$$

---

[5] We assume here infinitely stiff cables, with negligible mass.

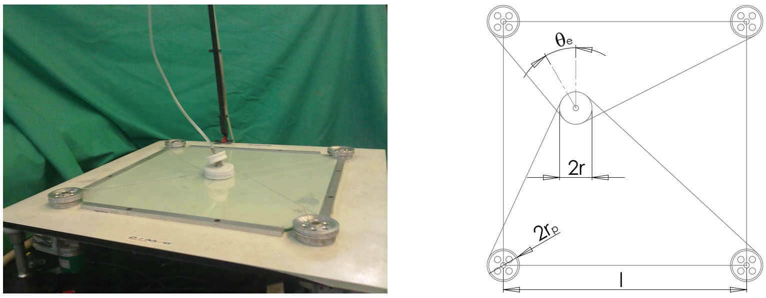

(a) (b)

Figure 2.3: The Feriba-3 haptic display (University of Padua, DIMEG) [8, 37]: a picture of the prototype (a) and the corresponding kinematic scheme (b).

From which the following six constraints are derived:

$$\begin{array}{lll} m_e + j\sum\limits_{i=1}^{n} u_{ix}^2 = \sigma_\Lambda; & m_e + j\sum\limits_{i=1}^{n} u_{iy}^2 = \sigma_\Lambda; & m_e\rho_e^2/L_\Lambda^2 + j\sum\limits_{i=1}^{n} c_i^2/L_\Lambda^2 = \sigma_\Lambda; \\ j\sum\limits_{i=1}^{n} u_{ix}u_{iy} = 0; & j\sum\limits_{i=1}^{n} c_i u_{ix}/L_\Lambda = 0; & j\sum\limits_{i=1}^{n} c_i u_{iy}/L_\Lambda = 0; \end{array} \tag{2.23}$$

Again, if we consider the three equations appearing in the first row of (2.23), we get:

$$L_\Lambda^2 = \frac{m_e\rho_e^2 + j\sum\limits_{i=1}^{n} c_i^2}{m_e + j\frac{n}{2}} \tag{2.24}$$

which can be rewritten using (2.16):

$$L_\Lambda^2 = \frac{m_e}{m_e + j\frac{n}{2}}\rho_e^2 + \frac{j\frac{n}{2}}{m_e + j\frac{n}{2}}L_\Lambda^2 \tag{2.25}$$

Equations (2.20) and (2.25) show that the normalized $\mathbf{\Lambda}$ depends on both inertial parameters (m_e, j) and device configuration $(\mathbf{A})$. Hence, in order to compare different layouts, the values of m_e and j must be known.

2.5 Case-study: comparative analysis of three planar CRPMs

Most of the performances of a device are strictly related to the structure matrix $\mathbf{A}$, which depends on the disposition of the pulley-blocks, on the disposition of the attachment-points in the end-effector and on the pose of the end-effector. Thus, once the number of DOFs and the number of cables have been decided, choosing the most convenient layout becomes the most important step in the design process.

The indices presented above allow to estimate the key-features of a design solution in the early phase of the design process. To prove the effectiveness of these tools, the indices will be applied to three different layouts, each corresponding to a prototype of planar CRPM that can be found in the Literature. In the following, a brief description of each design is presented.

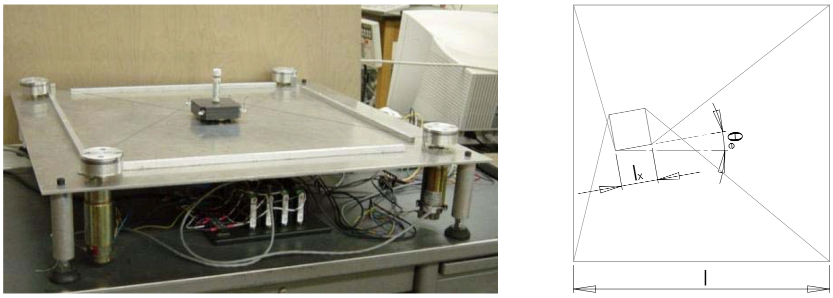

(a) (b)

Figure 2.4: The CDDR haptic display (Ohio University) [48] (a) and its kinematic scheme (b).

2.5.1 Feriba-3

The Feriba-3 [8, 37] haptic display has already been described in Section 1.4.1. Here we recall that it is a 4-wire planar CRPM with a circular end-effector, a square-shaped workspace (l = 450mm) and no fixed attachment points at the base (Fig. 2.3). The design allows cables to wind around the end-effector, and the base of the end-effector and the pulleys have the same winding radius ($r = r_p$ = 30mm). Each direct-driven pulley-block provides tension in the corresponding cable up to $f_{\max}$ = 10N.

2.5.2 CDDR

The Planar Translational Cable-Direct-Driven Robot [48] (simply referred to as CDDR in the following) is a 4-wire planar CRPM with a square-shaped end-effector, which was developed by R. L. Williams II and J. Vadia as an evolution of a similar concept prototype of cable-driven haptic device [46]. In [20], the authors studied a subclass of planar 3-DOF CRPM with rectangular end-effector and fixed cable points arranged on the vertexes of a square. They pointed out the advantages of crossed cable designs over non-crossed ones with respect to the wrench exertion capabilities. In addition, they found designs with square-shaped end-effectors to be the best ones, when considering only the statics workspace volume as the design criterion. Nonetheless, they showed that this result does not hold when taking into account the additional constraint of cable/end-effector interference. The resulting design (Fig. 2.4(a)) was conceived to operate at the nominal orientation $\theta_e = 0°$, so that cable interference cannot take place except at the boundaries of the workspace. The CDDR is part of a hybrid device composed of the cable-based module and a serial wrist mechanism, mounted at the CDDR end-effector. The former provides translational DOFs whereas the latter provides rotational DOFs. Hence, the CDDR is required to possess moment capabilities to keep zero orientation whenever a torque is applied at the end-effector. The base square has side l = 700mm and the end-effector square has side l_x = 100mm. Each pulley has a radius r_p = 38.1mm and is actuated by a DC gearmotor whose continuous rated torque is c_m = 2640Nmm. Since the main point of this chapter is to apply the performance indices to three different layouts rather than to specific prototypes, cable/end-effector interferences are neglected and the design is analyzed also for $\theta_e \neq 0°$.

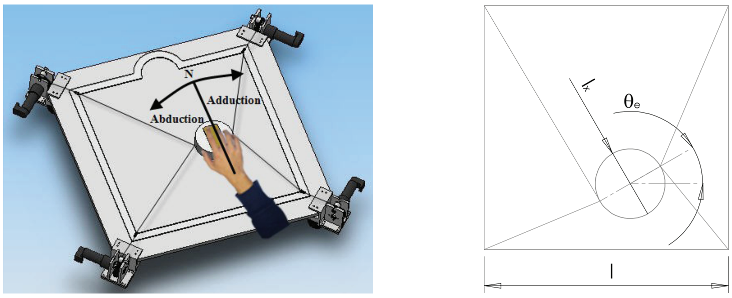

(a) (b)

Figure 2.5: CAD rendering (a) and kinematic scheme (b) of the CDHD haptic display (Beihang University) [88].

2.5.3 CDHD

The 3-DOF Cable-Driven Haptic Device [88] (simply referred to as CDHD in the following) is a 4-wire planar CRPM with a circular end-effector, designed for haptic applications (Fig. 2.5). The cable-based module provide force and moment feedback, whereas tactile feedback is conveyed via a piezoceramic plate mounted at the end-effector. Since there are only two attachment points at the end-effector, it can be modeled as a bar-shaped moving platform. Such configuration reduces the problem of cable interference, allowing for a wide range of end-effector orientations, as it was first noticed in one of the early studies on cable-based devices [89]. However, unlike the Feriba-3, incrementing $|\theta_e|$ has a strong detrimental effect on the statics workspace area, as it will be shown in the following. Thus, even though the authors declare an allowable workspace $350 \times 350mm^2$ wide and a $[-45°, 45°]$ orientation range, in many of those configurations the manipulator is not able to achieve static equilibrium for $f_{\text{min}} > 0$. The base square has side l = 350mm and the end-effector has a diameter l_x = 100mm. Each motor can generate tension in cables up to $f_{\text{max}} = 20.6N$.

2.5.4 Discussion

The performance indices defined in the previous sections are now applied to the planar CRPMs, with the aim of highlighting the advantages and the drawbacks of each layout. The *convex hull* of the cable connections to ground has been discretized into a grid of equally-spaced points that represent the positions of the end-effector centroid. Three orientations of the end-effector have been considered: $\theta_e = -30°, 0, 30°$. For each orientation, the values of the indices have been calculated over the computational grid, discarding points that do not belong to the statics workspace.

Results are presented in the form of contour plots, one for each orientation. Due to the particular design, the structure matrix of the Feriba-3 does not depend on θ_e. Therefore, a single contour plot is employed for this device, for each index. In each plot, a dashed-line rectangle encloses the workspace at $\theta_e = 0°$, while black dots are used to indicate the cable connection points (CDDR, CDHD) or the pulley rotation axes (Feriba-3)[6]. The design of the

---

[6] Notice that both the CDDR and the CDHD use fixed cable connection points to the ground, the pulley-blocks being mounted outside the square-shaped layout. The design of the Feriba-3, on the other hand, does not

		Feriba-3	Pl. Tr. CDDR	Pl. CDHD
$i_F/i_{F,\max}$	max	1.00	0.96	0.94
	min	0.65	0.50	0.34
	mean	0.78	0.73	0.68
	σ	0.08	0.10	0.14
$i_M/i_{M,\max}$	max	1.00	0.99	0.81
	min	0.62	0.47	0.28
	mean	0.77	0.70	0.53
	σ	0.09	0.12	0.12
i_I	max	0.65	0.64	0.67
	min	0.59	0.56	0.54
	mean	0.62	0.60	0.60
	σ	0.01	0.02	0.03
$P/P_{\min}$	max	2.42	3.97	7.55
	min	1.00	1.00	1.00
	mean	1.74	1.95	2.46
	σ	0.36	0.65	1.26
$\kappa(\mathbf{A})^{-1}$	max	1.00	0.75	0.84
	min	0.79	0.70	0.58
	mean	0.85	0.73	0.67
	σ	0.05	0.02	0.06
$\kappa(\mathbf{\Lambda})^{-1}$	max	1.00	0.68	0.78
	min	0.69	0.60	0.45
	mean	0.78	0.65	0.57
	σ	0.07	0.02	0.07

Table 2.1: Performance indices for the three devices at $\theta_e = 0°$. The $x - y$ workspaces have been discretized into a 500×500 point grid, and a circle ($r = l/4$) has been used as the reference region to calculate statistical measures.

Feriba-3 is the one that better exploits the overall dimension of the robot, since the statics workspace constantly equals the convex hull of the black dots. Conversely, the CDDR and the CDHD shows a rectangular workspace at $\theta_e = 0°$, since two symmetric lateral regions are wasted, where the angle between two crossed cables is greater than π. In the CDDR, this drawback is partially compensated, since the statics workspace exceeds the convex hull in two symmetrical regions located at the top and bottom of the device. In addition, the larger the orientation of the end-effector, the stronger the reduction of the workspace area, the effect being more noticeable for the CDHD.

The plots of $\theta_e = -30°$ and $\theta_e = 30°$ show symmetry, since the cable configuration is symmetric with respect to the y-axis for any pairs (x, y, θ_e) and $(-x, y, -\theta_e)$. Moreover, at $\theta_e = 0°$, all plots are symmetric to both the x-axis and the y-axis, since the cable configurations are symmetric in points having the same $|x|$ and $|y|$.

2.5.4.1 Manipulability indices

It can be easily proved that the maximum values of i_F and i_M for a planar CRPM having all the cables attaching points located at a distance r from the centroid of the end-effector are equal to $i_{F,\max} = f_{\max}$ and $i_{M,\max} = 2rf_{\max}$, respectively. These values have been used to compute the non-dimensional manipulability indices, which depend on the cables configuration only. Hence, they can be employed to objectively compare the layouts of the three devices, which are characterized by different values of $f_{\max}$.

As it is shown in Fig. 2.6 and in Fig. 2.7, the Feriba-3 achieves both $i_{F,\max}$ and $i_{M,\max}$ at

---

employ any fixed attachment point, so that cable connections vary with the position of the spool. In the following plots, however, according to the definition of statics workspace, only the configuration of the cables is taken into account, while end-effector interferences with attachment points and pulleys are not considered.

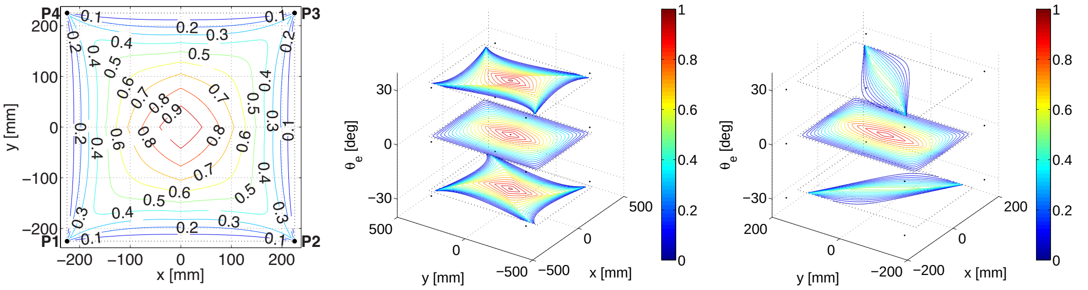

(a) (b) (c)

Figure 2.6: $i_F / i_{F,\max}$, normalized maximum isotropic force for the Feriba-3 (a), the planar translational CDDR (b) and the planar CDHD (c).

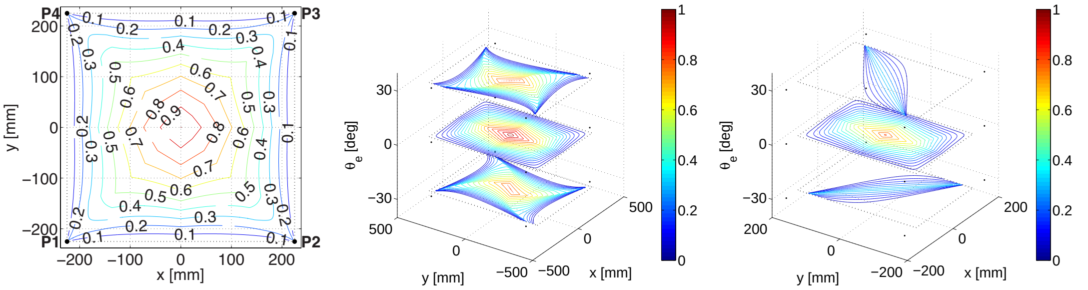

(a) (b) (c)

Figure 2.7: $i_M / i_{M,\max}$, normalized maximum moment for the Feriba-3 (a), the planar translational CDDR (b) and the planar CDHD (c).

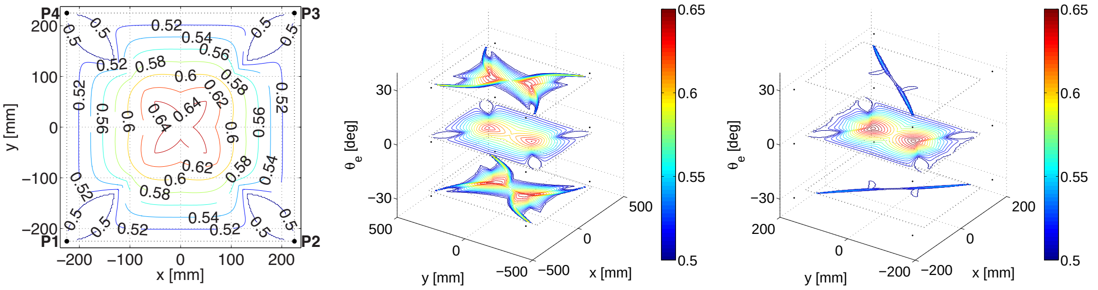

(a) (b) (c)

Figure 2.8: i_I, force-moment correlation index for the Feriba-3 (a), the planar translational CDDR (b) and the planar CDHD (c).

the center of the workspace, where the angles between adjacent cables are equal to $45°$ (this is the *optimal* cable configuration for manipulability indices). In the same pose, the maximum value of i_I is reached (Fig. 2.8). Both the contour lines of i_F and the contour lines of i_M are approximately circular near the origin and square near the boundaries of the workspace. Thus, the deterioration of the force capabilities is approximately a function of the distance between the centroid of the end-effector and the center of the workspace. This is a desirable feature, since the best force capabilities are attained in the most used region of the workspace. The CDDR and the CDHD show similar behaviors, as far as $\theta = 0°$. Nonetheless, the contour lines of i_M and i_F are "stretched" along the y-axis: the sudden loss of performance which occurs when the end-effector moves outward along the x-axis is due to the corresponding increment in the angle between two crossed cables. Due to their layout, neither the CDDR nor the CDHD can reach $i_{F,\max}$ or $i_{M,\max}$.

For $\theta = 0°$, two maximum points belonging to the y-axis can be observed in the plot of i_I, both in the CDDR and in the CDHD. In those points, the latter device shows slightly greater values of i_I (see Tab. 2.1). If we consider a circle with radius $l/4$ centered in the origin as the reference region, the Feriba-3 yields the most uniformly distributed values in all the manipulability indices, whereas the CDHD shows the highest variability (Tab. 2.1).

When departing from $\theta_e = 0°$, the force performances of both the CDDR and the CDHD decrease, the change being more sudden for the latter device. Hence, the CDHD may hardly show suitable force performances when $\theta_e \neq 0°$, unless opportunely oversized motors have been installed and, anyway, only inside a narrow workspace.

2.5.4.2 Power dissipation index

The non-dimensional power dissipation index depend on cable configuration and on the ratio $f_{\max}/f_{\min}$. For this study, we have set $f_{\max} = 10 f_{\min}$. In the contour plots of the normalized power dissipation $P/P_{\min}$, the contour lines range from 1 to 10 (see Fig. 2.9). While approaching the boundaries of the statics workspace, the dissipated power increases rapidly, until the constraint on $f_{\max}$ is reached. Clearly, the boundary of the statics workspace would be reachable only with infinite tensions on the aligned cables (i.e., power dissipation tends to infinity).

In all the devices, a considerable region of the statics workspace cannot be reached unless large amount of power is dissipated ($P > 10 P_{\min}$), even though the external force is zero ($\mathbf{F} = \mathbf{0}$). The remaining available workspace area is still acceptable for the Feriba-3 and the CDDR, whereas the CDHD proves to be nearly unusable at $\theta_e = \pm 30°$.

The index takes the optimal unitary value *if and only if*, with all the cables being tensioned

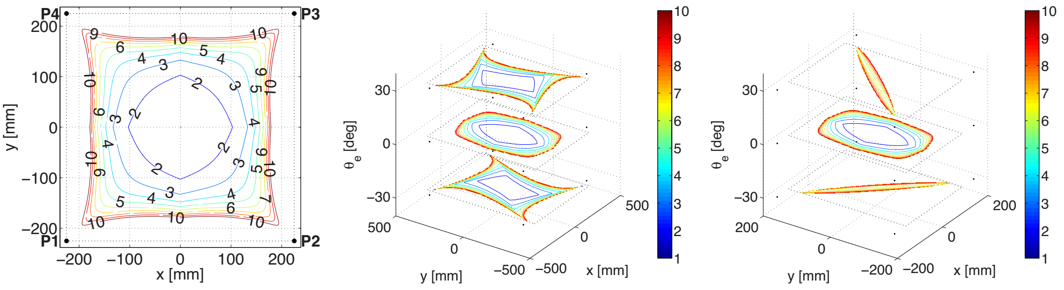

(a) (b) (c)

Figure 2.9: $P/P_{\min}$, normalized power dissipation for the Feriba-3 (a), the planar translational CDDR (b) and the planar CDHD (c).

at $f_{\min}$, the end-effector is in static equilibrium. For this condition to be satisfied, the cables configuration must be symmetric with respect to two orthogonal axes, or equivalently, there exists a *unitary vector* of $\mathbb{R}^n$ belonging to the null space of $\mathbf{A}$ (e.g., for CRPMs: $\ker(\mathbf{A}) = \langle \mathbf{1}_{m\times 1} \rangle$). At $\theta_e = 0$, all the devices reach the optimal value at the center of the workspace.

Inside the circular reference region, the Feriba-3 shows the lowest and most uniformly distributed values of the index (Tab. 2.1). The CDDR and the CDHD don't reach the optimal configuration for $\theta_e = \pm 30°$, even though the former shows two symmetric minimum points that are close to optimality ($P/P_{\min} \simeq 1.15$).

2.5.4.3 Dexterity index

For the analyzed devices, (2.16) yields the following values of L_A:

$$L_{A,Feriba} = \sqrt{2}r; \quad L_{A,CDDR} = l_x \left|\cos\theta_e\right|; \quad L_{A,CDHD} = l_x/2; \tag{2.26}$$

At $\theta_e = 0$, it can be proved that the end-effectors of the Feriba-3 and of the CDDR are isotropic *if and only if* each cable is orthogonal to the adjacent cables. For the end-effector of the CDHD, the *necessary and sufficient* condition is the cables connected to the same point being orthogonal.

At $\theta_e \neq 0$, the same condition holds for the Feriba-3, while for the other devices the constraints become *only sufficient*, that is, there exist other isotropic configurations where only two opposite pairs of adjacent cables are orthogonal (CDDR) or cables connected to the same point are not orthogonal (CDHD).

Clearly, some isotropic configurations cannot be reached, depending on the locations of the cable connections to the ground. The Feriba-3 reaches the kinematic isotropicity at the center of the workspace, whereas the CDHD reaches the isotropicity only at $\theta_e = 0$, in two symmetric poses (Fig. 2.10). The CDDR does not have any isotropic pose inside the workspace.

The dexterity index for the Feriba-3 varies approximately as a function of the distance between the end-effector centroid and the center of the workspace, unless the end-effector is near the pulley-blocks.

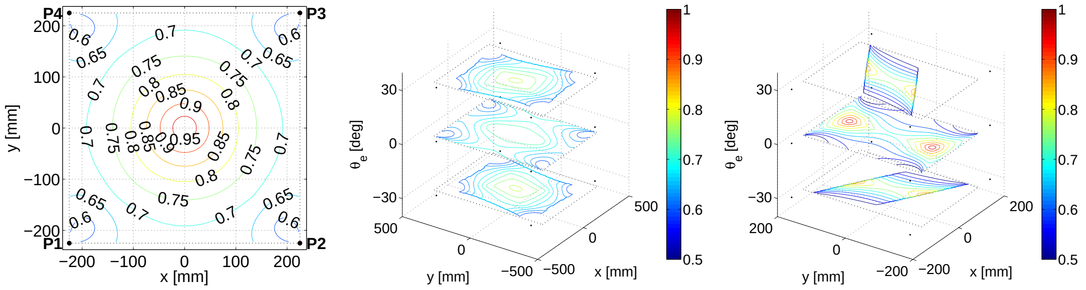

(a) (b) (c)

Figure 2.10: $\kappa\left(\bar{\mathbf{A}}\right)^{-1}$, dexterity index for the Feriba-3 (a), the planar translational CDDR (b) and the planar CDHD (c).

Inside the reference region, the dexterity index of the Feriba-3 shows the maximum values as compared to the other devices (see Tab. 2.1). Even though the CDDR does not reach isotropicity, the plot of $\kappa\left(\bar{\mathbf{A}}\right)^{-1}$ is the most uniformly distributed among those of the three devices, while the CDHD shows an undesirable decreasing trend as the end-effector approaches the center of the workspace, i.e., in the most useful region of the workspace.

2.5.4.4 Inertial Isotropy

In order to compute the inertial isotropicity index for different layouts, we arbitrarily set $m_e = 0.5\text{kg}$ and $j = 0.52\text{kg}$ for all the devices. The latter value has been calculated by assuming a fictitious average pulley with $r_p = 30\text{mm}$, $m_p = 0.5\text{kg}$ and a fictitious average motor with $I_m = 244\text{kgmm}^2$.

It can be proved that the isotropicity of $\mathbf{A}$ and the isotropicity of $\mathbf{\Lambda}$ are *equivalent* as far as translational DOFs are involved. In this case, the corresponding eigenvalues of $\mathbf{\Lambda}$ may be calculated from the singular values of $\mathbf{A}$ in close form. Even for the CRPMs analyzed here, the contour plots of $\kappa\left(\bar{\mathbf{\Lambda}}\right)^{-1}$ and $\kappa\left(\bar{\mathbf{A}}\right)^{-1}$ share the same maximum points (Fig. 2.10 and Fig. 2.11).

Clearly, the values of $\kappa\left(\bar{\mathbf{\Lambda}}\right)^{-1}$ differ from those of $\kappa\left(\bar{\mathbf{A}}\right)^{-1}$, as the latter depends on the mass matrix of the end-effector (2.25). Due to the particular choice of j and m_e, however, the two indices are quite similar for each prototype, thus, the same comments made in the previous paragraph apply here as well. With a heavier end-effector and/or smaller pulley-blocks (i.e., high m_e, ρ_e and/or small I_p/r_p ratio), the robot dynamics would be determined almost by the end-effector dynamics, yielding approximately uniform and unitary values of $\kappa\left(\bar{\mathbf{\Lambda}}\right)^{-1}$ over the entire workspace. Hence, inertial isotropy *may be improved in two ways*: by choosing a suitable design layout (i.e., by improving kinematic isotropy) and by choosing the right matching between end-effector and pulley-blocks.

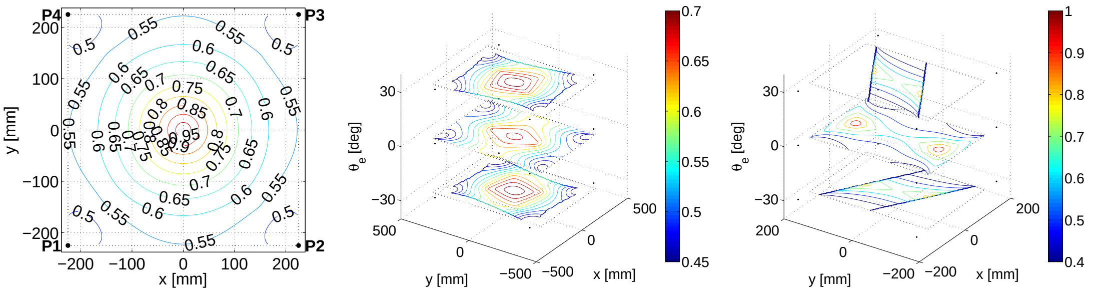

(a) (b) (c)

Figure 2.11: $\kappa\left(\bar{\mathbf{\Lambda}}\right)^{-1}$, inertial isotropy for the Feriba-3 (a), the planar translational CDDR (b) and the planar CDHD (c).

2.6 Conclusion

This chapter presented a set of performance indices for cable-based devices that can be employed in the design analysis as well as in the design optimization. The indices address the main kinetostatic and inertial properties of a cable-based robotic device. By using normalized indices that only depend on geometrical parameters, the designer is able to evaluate the strength and weakness points of different layouts, and to identify the most suitable one at the very early stage of the design process.

The effectiveness of this approach has been validated by applying the indices to three layouts, each corresponding to an existing planar CRPM: the Feriba-3, the Planar Translational Cable-Direct-Driven Robot (CDDR) and the 3-DOF Cable-Driven Haptic Device (CDHD). Results showed that the rotation of the end-effector has a detrimental effect on the performances of the CDDR and the CDHD. Thus, if the end-effector is required to operate at $\theta_e \neq 0°$, the best design is the one of the Feriba-3, for which the cable configuration is independent of the end-effector orientation. Besides, the design of the Feriba-3 gives the highest and most uniformly distributed performances. The CDDR proved an effective design as far as $\theta_e = 0°$ (which is actually the nominal orientation of the device). The useful workspace area of the CDHD and the allowable range for the end-effector orientation turned out to be far smaller than the nominal values, as the analysis revealed that the device is almost uncontrollable when $\theta_e \neq 0°$.

These results confirm that the performance of cable-based devices are highly affected by cable orientation with respect to the end-effector, suggesting that particular attention must be paid in the design to avoid a loss of performance in relevant portions of the workspace. In the next chapter, a novel approach is proposed to overcome this issue.

Chapter 3

Adaptive Cable-based Devices

In this Chapter, a novel design method for the development of cable-based systems is presented. In traditional designs employing fixed pulley-blocks, the structure matrix $\boldsymbol{A}$ *- which describes the cables configuration - changes with the pose of the moving platform. Since the performances are heavily influenced by* $\boldsymbol{A}$ *(Chapter 2), this results in a considerable variability of the robot capabilities throughout the workspace.*

Design requirements usually impose a minimum threshold of a given performance inside a reference workspace. Thus, once the most favorable layout has been identified, designers have to rely on other parameters to comply with the specifics (motor size, layout scaling, etc.). Consequently, the optimized solutions are often badly-tailored to the requirements.

In order to obtain more effective designs, the optimal configuration of cables w.r.t. the goal performance index should be guaranteed within the whole workspace. This can be achieved by introducing one or more moving pulley-blocks (i.e., additional DOFs in the system). In the following, this idea is formalized into a systematic design methodology. The effectiveness of the method is then validated through two simple case-studies.

3.1 A novel design approach

Several systematic approaches have been developed for the optimal design of cable-based systems. Global indices are usually employed to quantify the effectiveness of a specific design inside a reference region of the workspace. The performances at the moving platform are strictly related to cables configuration which, in turn, depends on the pose of the moving platform. As a result, traditional designs are characterized by high variability of performances within the workspace, and are often *badly-tailored* to the design goals.

In [76], G. Rosati & D. Zanotto proposed a novel method for the design of cable driven systems. The main idea relies on the introduction of one or more moving pulley-blocks (or trolleys) to optimize cable configuration according to current end-effector position. By properly moving the pulley-blocks, the workspace can be on-line modified to always keep the end-effector in the best part of the working space, thus enhancing robot capabilities without the need for additional cables. In this Chapter, we formalize this idea into a systematic design methodology [75]. Based on a total or partial decoupling between cables disposition and end-effector pose, this methodology allows to achieve *well-tailored* design solutions for a given design requirement. The resulting systems are here defined as *Adaptive Cable-Driven Systems*.

Cable-based robotic devices where the cables disposition can be reconfigured as a function of the end-effector pose have already been developed in the past years. Cable-based high-speed manipulators, for example, consist of hybrid parallel designs where some of the rigid links are replaced with cables [4, 2]. Crane-type manipulators may adopt moving trolleys or auxiliary robotic arms as well, either to control the location of the winches [90, 91, 92] or to directly act on one extremity of fixed-length cables [93]. Unlike previous works, we propose the introduction of moving pulley-blocks on completely and redundantly restrained systems to optimize the device capabilities within a given reference workspace.

In general, the performance indices employed in the optimization methods are function of several *design parameters* - relevant to the particular design problem - and of the *configuration variables*. The former may be discrete as well as continuous sets of geometrical or inertial parameters, typical of a unique design geometry and, therefore, independent of the end-effector pose. Whereas, the latter are the quantities that define the pose of the end-effector or moving platform. Examples of design parameters are: the number of employed cables, the disposition of cable entry points at the base and at the end-effector, the acceptable ranges of variability for cable tensions and lengths, the dimensional and inertial characteristics of pulleys, motor shafts and end-effector. Configuration variables may be expressed either in joint space (pulley wrap angles or cable lengths) or in task space (position and orientation of the end-effector). Anyway, as far as robot performance is concerned, the configuration of the moving platform may be synthesized in the *structure matrix* $\mathbf{A}$ [76].

Traditional optimization methods seek to find the best tuple of design parameters within a given range of variability [9, 21, 56, 94]. The optimal design is the one that yields the highest values of a certain performance index, inside a selected region of the task space. Even though *global* performance indices have been proposed (i.e., quantities that measure robot performance in the whole workspace), almost all of them are obtained from the elaboration of the values assumed by a certain *local* variable (i.e., a configuration-dependent quantity) inside a reference region. For this reason, the resultant optimal geometry is usually characterized by a high variability of performance as measured by the local variable, so the design goal may be achieved with a solution very *badly-tailored* to it.

Conversely, by allowing and controlling the movement of one or more pulley-blocks (i.e., the cable entry points at the base of the device) a total or partial decoupling between the end-effector pose and the disposition of cables can be obtained. In this way, the cable configuration can be kept close to the optimal one, regardless of the pose of the end-effector. This improvement of performance is obtained with no increment in the number of cables, thus reducing the risk of cable interference. By adopting this solution, the focus of the design process becomes the definition of a set of acceptable cable dispositions (with respect to the end-effector) satisfying a given performance goal. Once the acceptable set has been defined, the main objective of the design becomes to find a suitable way of moving the pulley-blocks (in terms of sliding surfaces and trajectory planning), with the aim of keeping the actual cable configuration within the desired set throughout the workspace.

This new approach implies a drastic change with respect to the traditional design process. Rather than defining a design criterion in the form of a *global* cost function, and then evaluate which geometry, among the acceptable ones, leads to the maximum global performance, the proposed method starts with the definition of a *local*, configuration-dependent performance index. Sufficient and - if possible - necessary conditions on cable configuration are then derived to guarantee a target level of the performance index. Finally, the movements of the pulley-blocks are studied, which allow to keep the configuration of cables within the

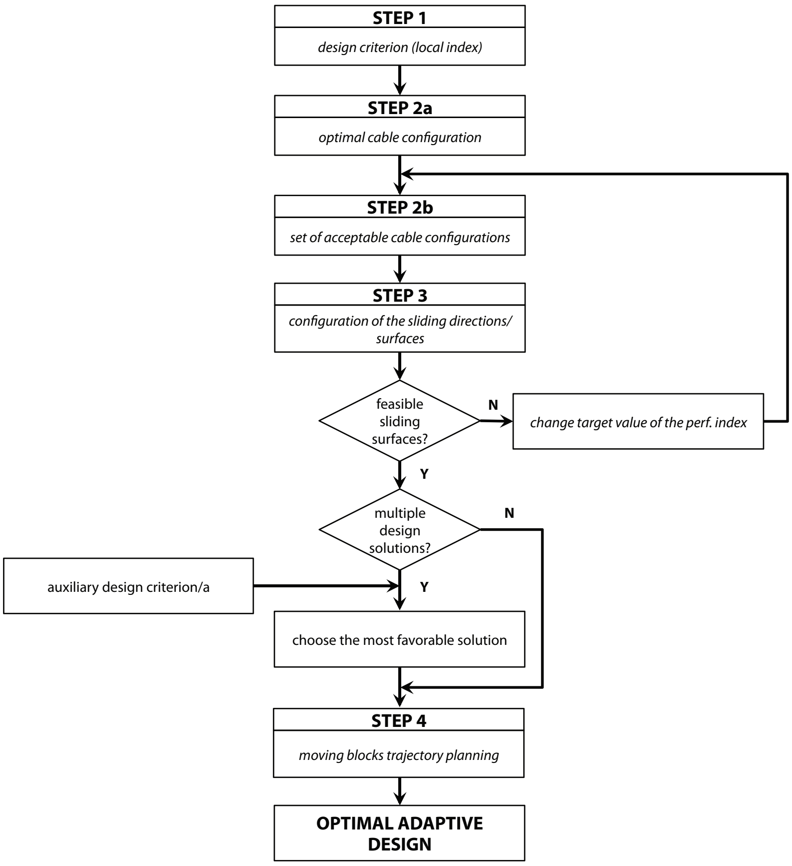

Figure 3.1: Proposed design method

acceptable set throughout the workspace. Ideally, the maximum value of the performance index could be obtained in the whole workspace. The so-obtained cable-driven system is capable of modifying the disposition of the pulley-blocks as a function of the end-effector pose. Specifically, if the system is capable of keeping the *optimal value* of the performance index in the whole workspace, it is addressed as a *Fully-adaptive Cable-Driven System*. Due to design restrictions, it may happen that the number of additional DOF is not sufficient to guarantee a complete decoupling between the pose of the end-effector and the cables configuration. In this case, the device can still be optimized to guarantee a target range of values for the performance index and, therefore, it is defined as a *Semi-adaptive Cable-Driven System*.

3.1.1 Proposed design method

The novel design methodology can be summarized in the following steps:

- **step 1:** Definition of a specific design criterion, in the form of a *local performance index*;
- **step 2a:** Derivation of the *optimal configuration of the cables* with respect to the end-effector, that yields the optimal value of the performance index defined in step 1;
- **step 2b:** Derivation of *a set of acceptable cable configurations*, that allows to achieve a *target value* of the local performance index (if the target value coincides with the

optimal value, then the acceptable set includes the optimal configuration only).

- **step 3:** Derivation of a feasible *configuration* of the sliding directions/surfaces for the pulley-blocks that allows to obtain the desired cable configurations throughout the workspace;
- **step 4:** Definition of the moving blocks *trajectory planning* as related to the trajectory planning of the end-effector.

Remark 1. In general, the outcome of **step 3** is not unique. Several design solutions may be obtained, that are equivalent from the point of view of the design criterion. In this case, one can choose the final design that yields the best values of some additional performance indices (e.g., the ratio between the useful and the total workspace volumes, the extent of pulley-blocks displacement as a function of the end-effector displacement, etc..) or by making other design considerations (e.g., possibility to maintain all the cables orthogonal to the sliding guides/surfaces to facilitate pulley-blocks position control, possibility to reach the same end-effector pose with multiple configurations of the pulley-blocks, total length of the guides or total surface area of the sliding surfaces, etc..).

Remark 2. Let us assume that each pulley-block could be approximated by a (dimensionless) moving point. For every pose of the end-effector, the optimal configuration of the cables imposes a constraint on the location of each pulley-block (namely, it must lie along a straight-line passing by the corresponding attachment point at the end-effector). Let n be the dimension of the subset of the workspace representing all the possible locations a particular attaching point can assume. Then, a set of locations for the corresponding pulley-block which satisfies the optimality constraints has dimension $n - 1$ at least and, clearly, it is not unique. Namely, one can choose between simple flat subsets (i.e. straight lines and planes) and more complex and smooth ones (curves and surfaces).

In the planar case, 1D paths are required to guarantee the desired motion of the pulley-blocks. Thus, in order to make those paths feasible, it is sufficient to design linear guides with an appropriate geometry, the simplest ones being straight lines. In the spatial case, the pulley-blocks/trolleys may be required to move on planes or complex surfaces. The latter result can be accomplished by using robotic manipulators to move the pulleys. Also, one can decide to move back to **step 2b** and change the target value of the performance index, so that the corresponding set of feasible cable configurations would be wider and, *hopefully*, achievable with simpler movements of the pulley-blocks, and, therefore, simpler surfaces.

Remark 3. The proposed design method can be thought of as an application to cable-based devices of the general framework introduced by C. M. Gosselin in [95] for *Adaptive Robotic Mechanical Systems*. Although following a similar principle, the two methods differ in that the design rules derived here are guaranteed by a proper mechanical design *and* by a proper control strategy (i.e., a particular trajectory planning of the pulley-blocks) rather than by the mechanical structure alone. In addition, the desired mechanical property is expressed here by the target value of a performance index rather than by a mathematical expression derived from a fundamental principle of mechanics. Finally, instead of using differentiation to impose the constancy of the desired property within the range of variability of the configuration parameters, a geometrical approach is employed here to derive the conditions for robot adaptiveness. Since these conditions are not explicit functions of the design parameters, the derivation of the design rules are not straightforward (i.e., a second optimization stage is required).

In Section 3.2, a simple design problem is introduced for a point-mass device. The problem is first solved by following a traditional approach, and then the novel method is applied to design a *Fully-adaptive* device and a *Semi-Adaptive* device. The output designs are compared in Section 3.2.4, showing how the adaptive solutions are the most *well-tailored* to the requirements. In a similar fashion, Section 3.3 presents a second case study, dealing with non point-mass devices. A comparison of the deign results is presented in Section 3.3.3.

3.2 First case study: Force performance of a 2-DOF device

Suppose that the following design problem was given:

Design a 2-DOF cable-based planar device, capable of exerting forces up to F_{REQ} inside a circular region with radius r_{REQ}. Assume negligible minimum cable tensions and infinitely stiff cables with negligible mass.

Since no preferential directions for the force have been defined, F_{REQ} is assumed as the value of the minimum isotropic force to be guaranteed inside the *useful workspace* of the device. Thus, a suitable performance index to perform the design optimization is the force index i_F, namely, the magnitude of the maximum force F obtainable in every direction of the workspace for a given position of the end-effector [8, 49, 76]. Hence, the design requirement is:

$$\forall \mathbf{P} \in B\left(\mathbf{O}, r_{REQ}\right) = \left\{\mathbf{P} \in \mathbb{R}^2 : d\left(\mathbf{P}, \mathbf{O}\right) \leqslant r_{REQ}\right\}, \quad i_F\left(\mathbf{P}\right) \geqslant F_{REQ} \tag{3.1}$$

where $d\left(\mathbf{P}, \mathbf{O}\right)$ is the *Euclidean distance* between a generic point $\mathbf{P}$ and the center $\mathbf{O}$ of the circle $B\left(\mathbf{O}, r_{REQ}\right)$ representing the required *useful workspace*. The following constraint must also be imposed on cable tensions: $f_i \in [0, f_{\max}]$, $\forall i = 1, 2, \ldots, n$, ($n$ being the number of cables), where $f_{\max}$ can be considered a design variable. Notice that, according to a different notation [42], condition (3.1) states that the required *useful workspace* must be a subset of the *Force Feasible Workspace* defined for a certain *Required Force-Set* (i.e., a circle with radius F_{REQ}).

3.2.1 Traditional approach

Following the traditional approach, we first define a set of candidate devices, and then try to find the most suitable one. The simplest cable-based device capable of completing the task is a planar 2-DOF, 3-cable robot with a point-mass end-effector. Since the required *useful workspace* is axially-symmetric, we choose a class of symmetric devices, whose cable entry-points P_1, P_2 and P_3 are located at the vertices of an equilateral triangle (see Fig. 3.2(a)). Let R be the radius of a circle that circumscribes the triangle, and r the radius of a concentric

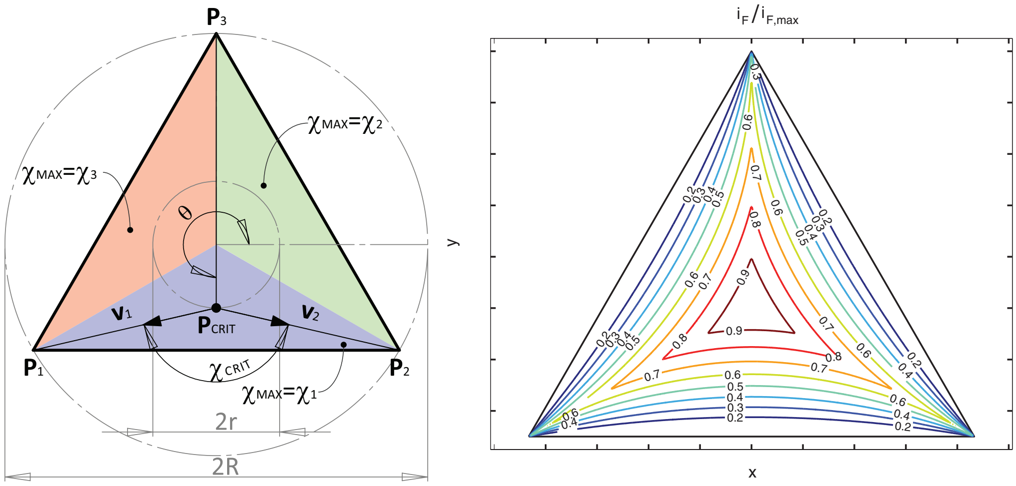

(a) (b)

Figure 3.2: Traditional design of a 3-cable, 2-DOF device (a) and the corresponding normalized force index $i_F/i_{F,\max}$ [76] (b).

circle which belongs to the *theoretical workspace*. Recall that the *theoretical workspace* of point-mass devices is the *convex-hull* of the cable entry points [52] (i.e., the triangle $\widehat{\mathbf{P}_1\mathbf{P}_2\mathbf{P}}_3$ in Fig. 3.2(a)), it must be: $r \leqslant R/2$. As a consequence, the minimum R is: $R_{\min} = 2r_{REQ}$.

Let us consider the constraints on the cable tensions: $f_i \in [0, f_{\max}]$, $\forall i = 1, 2, 3$. The polygon that represents all the feasible forces at a given position of the end-effector is obtained by drawing along each cable a vector representing the cable maximum tension $f_{\max}$, and two lines passing by the tip of that vector, parallel to the remaining cables. In Fig. 2.2(a), such vectors are denoted as $f_{\max}\mathbf{v}_i$, with:

$$\mathbf{v}_i = \frac{\mathbf{P}_i - \mathbf{P}}{\|\mathbf{P}_i - \mathbf{P}\|} \tag{3.2}$$

being the unit vector along the i-th cable.

The maximum isotropic force i_F is given by the radius of the circle centered in $\mathbf{P}$ and tangent to the polygon, which is also the minimum among the heights of the three equilateral parallelograms formed by the cable vectors. Fig. 3.2(b) depicts the contour plot of i_F for this system, where the index has been normalized to its maximum value ($i_{F,max}$), that is achieved in the centroid of the triangle [8]. It can be proved that the contour lines of i_F are arcs of circles. The best portion of the workspace is nearby the centroid, and the highest decrease of performance occurs while moving from the centroid to the sides along the heights. Let the i-th parallelogram be defined by the i-th cable vector and the adjacent cable in the CCW sense of rotation[1], and let χ_i be the angle between the same vectors. As long as $\mathbf{P}$ belongs to the *theoretical workspace*), the set of angles must comply with the following geometrical

---

[1] i.e., the $(\bmod\ (i, 3) + 1)$-th cable vector.

constraints (Fig. 3.2(a)):

$$\begin{cases} 0 < \chi_i \leqslant \pi, & \forall i = 1,2,3 \\ \sum_i \chi_i = 2\pi \end{cases} \tag{3.3}$$

Taking into account the first double inequality in (3.3), the height of the i-th equilateral parallelogram is yielded by (Fig. 2.2(a)):

$$r_i = \frac{\left| f_{\max}\mathbf{v}_i \times f_{\max}\mathbf{v}_{\bmod (i,3)+1} \cdot \mathbf{k} \right|}{\left\| f_{\max}\mathbf{v}_i \right\|} = f_{\max}\left|\sin\chi_i\right| = f_{\max}\sin\chi_i \tag{3.4}$$

where $\mathbf{k} = \{0,0,1\}^T$. Hence:

$$i_F = \min_{i=1,2,3} r_i = f_{\max}\min_{i=1,2,3}\left(\sin\chi_i\right) = f_{\max}\sin\left(\chi_{\max}\right) \tag{3.5}$$

To prove the last equivalence in (3.5), one may first notice that, if $\chi_{\max} = \max_{i=1,2,3}(\chi_i)$, conditions (3.3) imply that $\chi_{\max} \geqslant \pi/2$, while the remaining angles cannot be both strictly less than $\pi/2$. Then, if both the remaining angles are greater than $\pi/2$, the equivalence is proved by the fact that $\forall x \in [\pi/2, \pi]$ the function $\sin x$ is decreasing. Otherwise, the first double inequality implies that the smallest angle $\chi_{\min}$ must satisfy: $\chi_{\min} \geqslant \pi - \chi_{\max}$, which again proves the equivalence.

It is clear that, for given $f_{\max}$, i_F takes the optimal value $i_{F,\max}$ when each side of the polygon is tangent to the circumference, therefore when $\sin\chi_1 = \sin\chi_2 = \sin\chi_3$, or, taking into account (3.3), when $\chi_1 = \chi_2 = \chi_3 = 2\pi/3$. By substituting into (3.5), the expression for $i_{F,\max}$ is derived:

$$i_{F,\max} = \left(\sqrt{3}\big/2\right) f_{\max} \tag{3.6}$$

Let us consider the previously introduced class of devices, whose cable attachment points lie on the vertices of an equilateral triangle: the workspace can be split into three regions, each characterized by a different $\chi_{\max}$ (Fig. 3.2(a)). Within each region, i_F depends on a specific χ_i, namely, on the disposition of a specific pair of cables: however, given the symmetry of the cable entry-points, the same distribution of i_F has to be expected inside each region. The points having the minimum i_F among those belonging to $B(\mathbf{O}, r)$ are the ones with the greatest χ_i (e.g., the *critical point* $\mathbf{P}_{CRIT}$, shown in Fig. 3.2(a)). The corresponding i_F is:

$$i_{F,CRIT} = f_{\max}\sin\chi_{crit} = i_{F,\max}\frac{1-2(r/R)}{(r/R)^2-(r/R)+1}, \quad (r/R) \in \left[0, \tfrac{1}{2}\right] \tag{3.7}$$

A detailed proof of the previous assertion is provided in Section A.1, together with the derivation of (3.7).

By imposing that $i_{F,CRIT} = F_{REQ}$ and $r = r_{REQ}$ in (3.7), the optimal geometry of the device for a given $f_{\max}$ can be computed, namely, the largest (r_{REQ}/R) for which (3.1) holds:

$$(r_{REQ}/R)_{opt} = \left(\tfrac{1}{2} - \tfrac{1}{k}\right) + \sqrt{\tfrac{1}{k^2} - \tfrac{3}{4}}, \quad k = \frac{F_{REQ}}{i_{F,\max}} = \frac{2F_{REQ}}{\sqrt{3}f_{\max}} \tag{3.8}$$

The function $(r_{REQ}/R)_{opt}$ is depicted in Fig. 3.3 (solid line). Notice that it is a monotonically decreasing function of the parameter k, which is the ratio between the minimum (i.e., the required) and the maximum force performances inside the *useful workspace*.

The traditional method for the optimization problem can be summarized as follows:

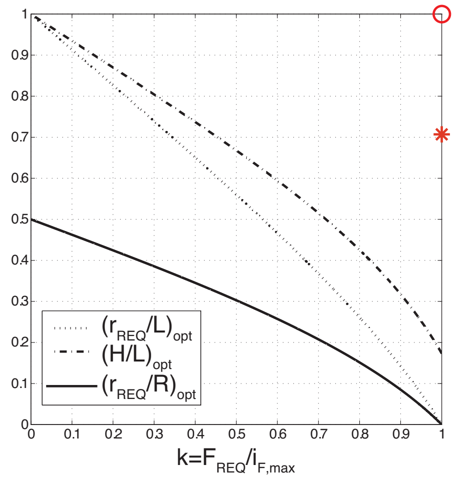

Figure 3.3: Correlation between layout geometry and force performances for the *traditional design* (solid line), the *Semi-adaptive design* (dashed lines), the *adaptive triangular design* (red asterisk) and the the *adaptive circular design* (red circle).

1. Choose an acceptable value for $f_{\max}$, s.t. $k < 1$;
2. Use (3.8) or Fig. 3.3 to compute $R_{opt} = r_{REQ} \Big/ \left(r_{REQ}/R\right)_{opt}$
3. If the resulting design is too cumbersome, increase $f_{\max}$ and return to step 2;

To sum up, we have shown that the force capabilities of this class of devices *are strictly related* to the disposition of the cable entry points: this correlation is expressed in (3.8) by using non-dimensional variables. In particular, it has been demonstrated that it is impossible to design a device which is compact (i.e., $\left(r_{REQ}/R\right)_{opt} \to 1/2$) and tailored to the force requirements (i.e., $k \to 1$) *at the same time*. The practical designs will be hence characterized by intermediate values of $\left(r_{REQ}/R\right)_{opt}$ and k, which do not fully exploit neither the *theoretical workspace*, nor the maximum force capabilities.

3.2.2 Fully-adaptive designs

We assume that there are no design restrictions on the number of installed actuators. Thus, by following the steps outlined in Section 3.1.1, we get:

step 1: Local performance index: i_F, design criterion: $i_F = F_{REQ}$.

step 2a: Optimal configuration of the cables, yielding $i_F = i_{F,\max}$: $\chi_1 = \chi_2 = \chi_3 = 2\pi/3$ (see Section 3.2.1).

step 2b: We regard the *optimal* configuration as the only acceptable configuration.

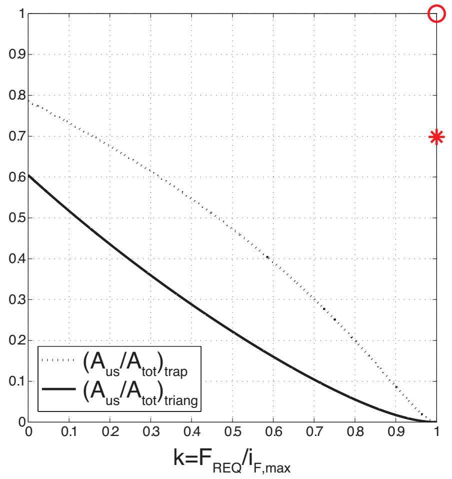

Figure 3.4: Correlation between $(A_{us}/A_{tot})_{opt}$ and force performances for the *traditional design* (solid line), the *Semi-adaptive design* (dashed line), the *adaptive triangular design* (red asterisk) and the the *adaptive circular design* (red circle).

step 3: By properly moving the cable entry points, the aforementioned configuration must be kept throughout the required workspace. Even though this goal may be achieved with different degrees of kinematic redundancy, it seems reasonable to add a single DOF to each pulley-block, so as to limit the system complexity. Thus, the motion of each pulley-block will be constrained over a fixed plane curve. To fix the ideas, two design solutions will be taken into account.
The simplest curve one can think of is a *straight line*. Let us use three linear guides to form an equilateral triangle. By moving the pulley-blocks so as to keep orthogonality between each cable direction and the corresponding guide, the optimal cable configuration can be achieved inside the whole triangle. This choice has the advantage of minimizing the disturbance effect of cable tensions on pulley-blocks position control. In addition, since the required workspace is a circle of radius r_{REQ}, the length of each guide can be reduced to $2r_{REQ}$, giving the final layout shown in Fig. 3.5(a).

A second design solution relies on a single *circular* guide: again, the optimal cable configuration may be kept throughout the circle by properly moving the pulley-blocks, as shown in Fig. 3.5(b). Since both the aforementioned designs are capable of keeping the optimal cable configuration within the whole workspace, we refer to those designs as *Fully-adaptive designs*.

The optimal values for the geometrical design parameter R may be immediately deduced in both the devices: $R_{opt,T} = \sqrt{2}r_{REQ}$ and $R_{opt,C} = r_{REQ}$. Likewise, deriving $f_{\max,OPT}$ is straightforward: since the values of the force index are constant throughout the workspace (namely, $i_F = i_{F,\max}$), we impose $i_{F,\max} = F_{REQ}$ in order to fulfill the requirements with the smallest actuator sizes, and find $f_{\max,OPT} = 2F_{REQ}/\sqrt{3}$ from (3.6).

It should be noticed that, thanks to the *adaptiveness* of the devices, R_{opt} is no longer related to $f_{\max}$: hence, the resulting designs are the most compact and the most *well-tailored* to the requirements, *at the same time*.

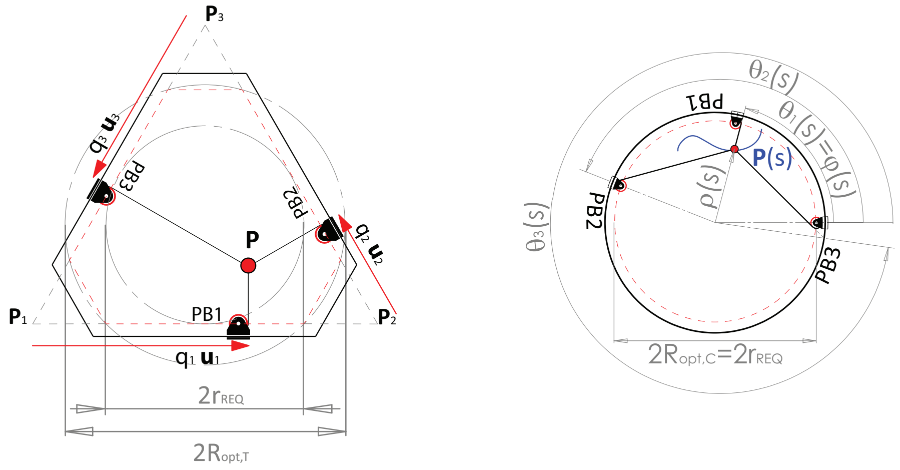

(a) (b)

Figure 3.5: Fully-adaptive designs with linear (a) and circular (b) guides.

step 4: The next step of the design process consists in the definition of the pulley-blocks trajectories for a given end-effector trajectory. Let $\mathbf{P}(s)$ be a plane curve, entirely contained inside the workspace:

$$\mathbf{P}(s) = \{x(s), y(s)\}^T, \quad s \in [0, L], \tag{3.9}$$

where L is the length of the curve. For the first design solution (*straight-line guides*), there exists a *one-to-one* relationship between the position of the end-effector and those of the pulley blocks that yield the optimal cable configuration, so that the derivation of the *i-th* pulley-block trajectory is straightforward:

$$\begin{cases} q_i(s) = \mathbf{u}_i \cdot (\mathbf{P}(s) - \mathbf{P}_i) \\ \dot{q}_i = \mathbf{u}_i \cdot \dfrac{d\mathbf{P}(s)}{ds}\dot{s} \\ \ddot{q}_i = \mathbf{u}_i \cdot \left(\dfrac{d\mathbf{P}(s)}{ds}\ddot{s} + \dfrac{d^2\mathbf{P}(s)}{ds^2}\dot{s}^2\right) \end{cases} \tag{3.10}$$

where $\mathbf{u}_i$ is the unit vector along the *i-th* linear guide, $\mathbf{P}_i$ is the position vector of the *i-th* vertex of the triangle, and q_i is the configuration variable of the *i-th* pulley-block (Fig. 3.5(a)).

As to the second design solution (*circular guide*), there is a set of ∞^1 optimal configurations of the pulley-blocks for any given position of the end-effector, since any configuration of the cables can be rigidly rotated without changing the relative angles χ_i[2]. One may take advantage of this feature by choosing a favorable configuration: for example, by requiring that the direction of one of the cables be always radial (i.e., orthogonal to the circular guide), the loading of the corresponding pulley-block actuator will be reduced (Fig. 3.5(b)).

---

[2] Theoretically, this is true also for the first design solution, if we do not impose the orthogonality constraint between each cable and the corresponding guide. In practice, however, the straight-line arrangement limits the motion of each trolley to a single guide.

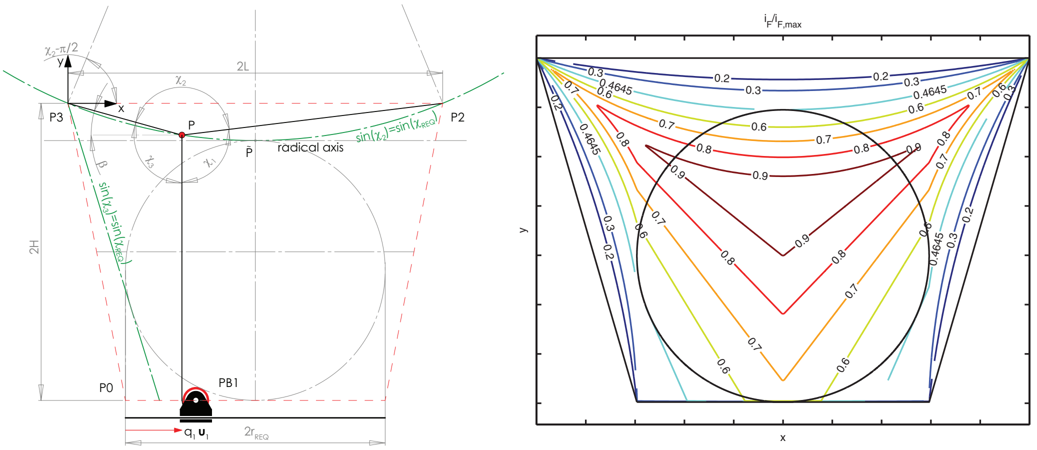

(a) (b)

Figure 3.6: Semi-adaptive device: derivation of the optimal design for given k (a) and the corresponding normalized force index $i_F/i_{F,\max}$ [76] (b).

Under this constraint, suppose that the trajectory of the end effector is known in polar coordinates $(\rho(s), \varphi(s))$, with $\rho \in (0;\ r]$, $\varphi \in [0;\ 2\pi)$. The corresponding pulley-block trajectories are:

$$\boldsymbol{\vartheta}(s) = \left\{ \begin{array}{c} \vartheta_1(s) \\ \vartheta_2(s) \\ \vartheta_3(s) \end{array} \right\} = \left\{ \begin{array}{c} \varphi(s) \\ \varphi(s) + 2\pi/3 - \arcsin\left(\frac{\sqrt{3}\rho(s)}{2r}\right) \\ \varphi(s) - 2\pi/3 + \arcsin\left(\frac{\sqrt{3}\rho(s)}{2r}\right) \end{array} \right\} \tag{3.11}$$

where $\boldsymbol{\vartheta}(s)$ is the vector of the polar angles of the pulley blocks. Whenever the end-effector passes through the center of the circle (i.e., $\rho(s) = 0$ for some values of s) a step discontinuity $\pm\pi$ is introduced in $\varphi(s)$ and, therefore, in all the components of $\boldsymbol{\vartheta}(s)$. Thus, for the planning criterion described by (3.11), the value $\rho = 0$ is not feasible.

By deriving (3.11) we get the following expression for the angular velocities and accelerations of the pulley blocks:

$$\dot{\boldsymbol{\vartheta}} = \mathbf{J}(s) \left\{ \begin{array}{c} \frac{d\rho(s)}{ds} \\ \frac{d\varphi(s)}{ds} \end{array} \right\} \dot{s}, \quad \ddot{\boldsymbol{\vartheta}} = \mathbf{J}(s) \left\{ \begin{array}{c} \frac{d\rho(s)}{ds} \\ \frac{d\varphi(s)}{ds} \end{array} \right\} \ddot{s} + \left(\mathbf{J}(s) \left\{ \begin{array}{c} \frac{d^2\rho(s)}{ds^2} \\ \frac{d^2\varphi(s)}{ds^2} \end{array} \right\} + \frac{d\mathbf{J}(s)}{ds} \left\{ \begin{array}{c} \frac{d\rho(s)}{ds} \\ \frac{d\varphi(s)}{ds} \end{array} \right\} \right) \dot{s}^2 \tag{3.12}$$

where $\mathbf{J}(s)$ is the Jacobian matrix with respect to $\rho(s)$ and $\varphi(s)$.

3.2.3 Partially-adaptive design

Suppose the number of actuated joints be constrained to 4. With less than 6 actuators, it would be impossible to develop a Fully-adaptive design satisfying the design problem (3.1). Taking into account the introduced design restrictions, the application of the novel design approach leads to new steps 2b-4:

step 2b: The optimal configuration of the cables cannot be maintained over the whole reference workspace. However, we can choose for i_F the widest range of values satisfying the design problem (3.1) (i.e., $i_F(\mathbf{P}) \in [F_{REQ}, i_{F,\max}]$) and derive the corresponding set of cables configuration from (3.5) and (3.6):

$$\sin(\chi_{REQ}) \leqslant \sin(\chi_{\max}) \leqslant \sqrt{3}/2 \tag{3.13a}$$

$$2\pi/3 \leqslant \chi_{\max} \leqslant \chi_{REQ} \tag{3.13b}$$

Thus, χ_{REQ} must be regarded as the greatest acceptable value that $\chi_{\max}$ can take inside $B(\mathbf{O}, r_{REQ})$. Also, from the definition of k in (3.8):

$$\sin(\chi_{REQ}) = k\sqrt{3}/2 \tag{3.14a}$$

$$\chi_{REQ} = \pi - \arcsin\left(k\sqrt{3}/2\right) \tag{3.14b}$$

step 3: For the sake of simplicity, we restrict the analysis to a family of candidate devices, namely, the ones wherein the additional DOF is employed to move one pulley along a *straight-line path*, keeping orthogonality between the path and the corresponding cable.

Let us consider the generic prototype belonging to the aforementioned family (Fig. 3.6(a)), with two upper attachment points ($\boldsymbol{P}_2$ and $\boldsymbol{P}_3$) and a bottom pulley-block that can slide along a straight-line guide (defined by point $\boldsymbol{P}_0$ and by the unit vector $\mathbf{u}_1$). The length of the line connecting the upper attachment points is $2L$, the guide is parallel to the line and the distance between the line and the guide is $2H$. The resulting design shows one vertical axis of symmetry. The origin of the reference frame coincides with the point $\mathbf{P}_3$ (Fig. 3.6(a)). The trapezoidal theoretical workspace is given by the union of the convex hulls of the cable attachment points, obtained as the lower trolley spans its entire range of motion.

Following the introduced methodology, we now derive the optimal geometry and disposition of the sliding guide. This, in turn, will also define the optimal design for the candidate device. In order to achieve this target, we must be able to find the largest circle for which the conditions (3.13) hold.

Let us first consider the loci of points $\boldsymbol{P}$ such that $\sin(\chi_i)$ has a constant value. These loci gives the contour lines of $\sin(\chi_{\max})$ whenever $\chi_i \equiv \chi_{\max}$. The loci having $\sin(\chi_2) = \text{const}$ are actually *arcs of circles*. Consider the points $\mathbf{P_2}$ and $\mathbf{P_3}$, and a point $\mathbf{P}$ located *below* the segment $\overline{\mathbf{P}_2\mathbf{P}_3}$ (Fig. 3.6(a)). Basic trigonometric observations guarantee that the set of points yielding the same value of χ_2 as $\mathbf{P}$ coincides with the arc of the circle passing through $\mathbf{P}$, $\mathbf{P}_2$ and $\mathbf{P}_3$ [3]. The radius of the circle and the coordinates of its center can be easily determined from χ_2 and L:

$$\mathbf{C} = L\left\{\begin{matrix} 1 & \sqrt{\frac{1}{\sin^2\chi_2} - 1} \end{matrix}\right\}^T; \quad r = \frac{L}{\sin\chi_2} \tag{3.15}$$

Besides, the sets of points having $\sin(\chi_3) = \text{const}$ are straight lines passing through the origin (Fig. 3.6(a)):

$$\sin\chi_3 = \cos\beta = \frac{x}{\sqrt{x^2+y^2}} \xrightarrow{y<0,\ x>0} y = x\cot\chi_3 \tag{3.16}$$

---

[3] Actually, this is true as far as the center of the circumference lays above the line segment $\overline{\mathbf{P}_2\mathbf{P}_3}$

Finally, the loci having $\sin(\chi_1) = \text{const}$ (although unnecessary for the following analysis), may be computed from (3.16) by using the conditions of symmetry. Notice that χ_1, χ_2 and χ_3 decrease towards the center of the workspace. Thus, as in the traditional design, each of the three regions wherein a certain $\chi_i = \chi_{\max}$ is bounded, and the boundaries themselves can be easily derived by computing the intersection points of the previous loci as a function of χ.

Indeed, the boundary between the two regions characterized by $\chi_2 = \chi_{\max}$ and $\chi_3 = \chi_{\max}$ can be computed by first substituting the expression of x from (3.16) into the parametric equation corresponding to the circumference (3.15):

$$\begin{cases} y = -2L\cos(2\chi)\cot(\chi) \\ x = -2L\cos(2\chi) \end{cases} \tag{3.17}$$

and then eliminating the dependence on χ:

$$\begin{gathered} \cot^2(\chi) = \frac{1-\frac{x}{2L}}{1+\frac{x}{2L}} = \frac{2L-x}{2L+x} \\ y^2 = x^2\frac{2L-x}{2L+x} \xrightarrow{y<0,\ 0<x<2L} y = x\sqrt{\frac{2L-x}{2L+x}} \end{gathered} \tag{3.18}$$

Again, the boundary between the two regions characterized by $\chi_2 = \chi_{\max}$ and $\chi_1 = \chi_{\max}$ (although unnecessary for the following analysis) may be computed form (3.18) by applying the conditions of symmetry. The last boundary is evidently a straight line segment belonging to the perpendicular bisector of $\overline{\mathbf{P}_2\mathbf{P}_3}$.

The previous analysis provides the close-form expressions for the contour lines of the function $\sin(\chi_{\max})$. Therefore, for any k, the corresponding $\sin(\chi_{REQ})$ is first derived, and then the largest circumference for which (3.13a) holds is computed. Indeed, due to the symmetry, this circumference is tangent to the contour line $\sin(\chi_{\max}) = \sin(\chi_{REQ})$ in three points, and has its center in $x = L$. The latter condition, in turn, implies that the circumference is tangent to (3.15) in the point $\tilde{\mathbf{P}}$ (Fig. 3.6(a)):

$$\tilde{\mathbf{P}} = L\left\{\begin{matrix} 1 & -\cot\left(\frac{\chi_{REQ}}{2}\right) \end{matrix}\right\}^T \tag{3.19}$$

the common tangent being $y = y_{\tilde{\mathbf{P}}}$.

Let us consider the set of circumferences passing through $\tilde{\mathbf{P}}$ and having the aforementioned line as the radical axis:

$$(x-L)^2 + \left(y - y_{\tilde{\mathbf{P}}}\right)^2 + \tilde{\alpha}\left(y - y_{\tilde{\mathbf{P}}}\right) = 0, \quad \tilde{\alpha} \in \mathbb{R} \tag{3.20}$$

The largest circumference is found by imposing on (3.20) the condition of tangency with the boundary of the set (3.16) corresponding to $\sin(\chi_3) = \sin(\chi_{REQ})$:

$$\alpha = \frac{\tilde{\alpha}}{2L} = (2 + \sec\chi_{REQ})(\tan\chi_{REQ} - \sec\chi_{REQ}) \tag{3.21a}$$

$$(r_{REQ}/L)_{opt} = \alpha \tag{3.21b}$$

$$(\mathbf{C}_{REQ}/L)_{opt} = \left\{ \begin{matrix} 1 & -\left(\cot \frac{\chi_{REQ}}{2} + \alpha\right) \end{matrix} \right\}^T \tag{3.21c}$$

The smallest design containing this circumference is the one having a $2r_{REQ}$ long linear guide, which is tangent to the circumference (Fig. 3.6(a)). Therefore, the normalized distance H/L is given by:

$$(H/L)_{opt} = \frac{1}{2}\cot\frac{\chi_{REQ}}{2} + \alpha \tag{3.22}$$

Finally, the following identities are applied to rewrite (3.21) and (3.22) in terms of $k = F_{REQ}/i_{F,\max}$:

$$\tan\chi = \frac{-3k}{\sqrt{12-9k^2}}; \quad \sec\chi = \frac{-2}{\sqrt{4-3k^2}}; \quad \cot\frac{\chi}{2} = \frac{2-\sqrt{4-3k^2}}{k\sqrt{3}} \ ; \tag{3.23}$$

Notice that equations (3.21-3.23) define the optimal design *as a function of* k, and must therefore be regarded as the counter part of (3.8) for this particular class of Semi-adaptive devices.

Figure 3.3 provides a graphical representation of (3.21b) and (3.22) written in terms of k. Figure 3.6(b) shows the contour lines of k for an optimal *Semi-adaptive* design. In this example case, the value of $k \approx 0.4645$ has been chosen to give a good compromise between force performance and compactness ($(A_{us}/A_{tot})_{opt} \approx 0.5$). Notice that the contour lines $\sin(\chi_3) =$ const and $\sin(\chi_1) =$ const keep a straight line shape as long as cable 1 is orthogonal to the linear guide. However, when x is such that $(x - x_{\mathbf{P}_0}) < 0$ or $(x - x_{\mathbf{P}_0}) > 2r_{REQ}$, the trolley $PB1$ is stationary in one of the *dead points* of its stroke, thereby the contour lines become circle arcs as in the case of $\sin(\chi_2) =$ const.

step 4: Given a path $\mathbf{P}(s)$ as defined in (3.9), the trajectory planning of the lower trolley can be easily written as follows:

$$q_1(s) = \begin{cases} 0 & if \quad l_1 < 0 \\ l_1 & if \quad 0 \leqslant l_1 \leqslant 2r_{REQ} \\ 2r_{REQ} & if \quad l_1 > 2r_{REQ} \end{cases} \tag{3.24a}$$

$$\dot{q}_1(s) = \begin{cases} 0 & if \quad l_1 < 0 \\ \mathbf{u}_1 \cdot \frac{d\mathbf{P}(s)}{ds}\dot{s} & if \quad 0 \leqslant l_1 \leqslant 2r_{REQ} \\ 0 & if \quad l_1 > 2r_{REQ} \end{cases} \tag{3.24b}$$

$$\ddot{q}_1(s) = \begin{cases} 0 & if \quad l_1 < 0 \\ \mathbf{u}_1 \cdot \left(\frac{d\mathbf{P}(s)}{ds}\ddot{s} + \frac{d^2\mathbf{P}(s)}{ds^2}\dot{s}^2\right) & if \quad 0 \leqslant l_1 \leqslant 2r_{REQ} \\ 0 & if \quad l_1 > 2r_{REQ} \end{cases} \tag{3.24c}$$

where $l_1 = \mathbf{u}_1 \cdot (\mathbf{P}(s) - \mathbf{P}_0)$.

3.2.4 Comparison of the design results

Figures 3.3 and 3.4 sum up the results from Sections 3.2.1, 3.2.2 and 3.2.3. The former diagram shows the dependence of the robot dimensions on the parameter k, which measures how *well-tailored* a device is to the force requirements. The latter diagram depicts the ratio A_{us}/A_{tot} as a function of the same parameter. A_{us} is the surface area of the *useful workspace*, whereas A_{tot} is the area of the whole *theoretical workspace* of the device. Their ratio gives a measure of the compactness of a design.

The Fully-adaptive designs are the most *well-tailored* to the force requirements (red asterisk and red circle in Fig. 3.3), whereas to reach the same level of force performance, the traditional and the Semi-adaptive designs would require an infinite workspace area (i.e., $R \to \infty$ or $L \to \infty$). The most compact design is the Fully-adaptive circular design, while the Fully-adaptive triangular design presents slightly lower indices (i.e., $(r_{REQ}/R_{opt}) = 1/\sqrt{2}$ and $(A_{us}/A_{tot}) = 2\pi/9$) due to unused peripheral areas[4]. The partially-adaptive design is a good compromise between simplicity and performance, while the traditional design is the most cumbersome, even in the best condition ($k \to 0$, i.e., ideal tensioning motors, $f_{\max} \to \infty$).

The presence of a single moving trolley is clearly not sufficient to decouple the cable disposition and the pose of the end-effector. As a consequence, in the Semi-adaptive device depicted in Fig. 3.6(a), the optimal design parameters are still determined by the force performances, and the more compact the design, the less well-fitted to the force requirements. As compared to the traditional one, however, this design allows a better exploitation of the total workspace area for each value of k, as shown in Fig. 3.4. As a further advantage, for all the devices belonging to this subclass, it is possible to increase the value of H beyond the optimal value without affecting the force performance inside the reference workspace, thereby allowing to arbitrarily choose the vertical position of the useful workspace.

To fix the ideas, let us consider the following design example: $r_{REQ} = 300\text{mm}$, $F_{REQ} = 50\text{N}$. By following the traditional design, let's say we tested several values of k and concluded that $k = 0.25$ can be an acceptable compromise between compactness and force requirements. Thus, we get $R \approx 741\text{mm}$ and $f_{\max} \approx 231\text{N}$. By applying the novel design method, the same requirements may be fulfilled with a Fully-adaptive triangular design with $R \approx 424\text{mm}$ and $f_{\max} \approx 58\text{N}$, or with a Fully-adaptive circular design with $R = 300\text{mm}$ and $f_{\max} \approx 58\text{N}$. When it is not possible to use 6 actuators, a compromise design solution may be found in the Semi-adaptive device: for $k = 0.5$, it yields $L \approx 506\text{mm}$, $H \approx 353\text{mm}$ and $f_{\max} \approx 124\text{N}$.

Hence, even though the Fully-adaptive designs are more complex and require the installation of additional actuators, this drawback may be fully compensated by the reduction in the size of the tensioning motors and in the size of the structure. An alternative traditional design could employ the same number of additional actuators to add more cables (6-cable traditional device). However, in this case, we would still get a greater R with respect to the adaptive designs, with a dramatically increased risk of cable interference.

Among the Fully-adaptive devices, the triangular design involves a simpler structure,

---

[4] Clearly, this result may not hold for different shapes of the required *useful workspace*.

simpler pulley-blocks trajectory planning and smaller size of the pulley-blocks actuators (since the cables are kept orthogonal to the sliding directions, the work of cable tensions due to the motion of pulley-blocks is always null). The circular design, on the other hand, is more compact. Semi-adaptive solutions may represent an advantageous compromise whenever redundant actuation is an issue.

3.3 Second case study: Dexterity of a 3-DOF device

Let consider this optimization problem, dealing with the kinematic isotropicity of 3-DOF planar devices:

Design a 3-DOF cable-based planar device whose dexterity, as described by the inverse Jacobian condition number, is greater than κ_{REQ}^{-1} *inside a circular region with radius* r_{REQ}*. Assume negligible minimum cable tensions and infinitely stiff cables with negligible mass.*

Equations (2.2), (2.13) and (2.16) describe how to determine the normalized structure matrix $\bar{\mathbf{A}}$, from which the dexterity index $\kappa\left(\bar{\mathbf{A}}\right)^{-1}$ can be computed (Section 2.3). Additionally, equations (2.15) allow to derive the isotropic configurations of a device (this result is required for the development of the adaptive designs in Section 3.3.2). Assuming $L_{\mathrm{A}} \neq 0$, we subtract the first two equations and rewrite the last three equations in a more suitable way:

$$\sum_{i=1}^{n} \cos\left(2\beta_i\right) = 0; \quad \sum_{i=1}^{n} \sin\left(2\beta_i\right) = 0; \tag{3.25a}$$

$$\sum_{i=1}^{n} c_i \mathbf{u}_i = \mathbf{0} \tag{3.25b}$$

where β_i is the angle between a given x axis and the i-th cable, measured in the CCW direction.

For $n = 4$[5], it is easy to verify that (3.25a) imposes the existence of (at least) two disjoined pairs of mutually orthogonal cables (i.e., $\beta_j = \beta_i \pm \pi/2$ and $\beta_l = \beta_k \pm \pi/2$). Equation (3.25b) depends on c_i, namely, the projection along the z axis of the moment applied by the i-th cable subjected to a unitary tension. In general, the c_i terms vary with the *shape* and *orientation* of the moving platform. However, if we choose a *circular platform* and let the wires *wrap* around its sides as shown in Fig. 3.7(a), the absolute value of c_i constantly equals the radius of the end-effector r (despite the orientation of the platform), and (3.25b) takes this simpler form[6]: $\mathbf{u}_1 + \mathbf{u}_3 = \mathbf{u}_2 + \mathbf{u}_4$. Under those hypotheses, it can be easily proven that the only isotropic configurations are those wherein *all the adjacent cables are orthogonal.*

3.3.1 Traditional approach

Before performing the design optimization, we make two further assumptions. Instead of passing through a fixed attaching point to the ground, each cable is directly wound onto a

---

[5] The simplest cable-based device capable of controlling 3-DOF employs 4 cables (completely restrained design).

[6] This leads to the same traditional design as the one presented in Section 2.5.1

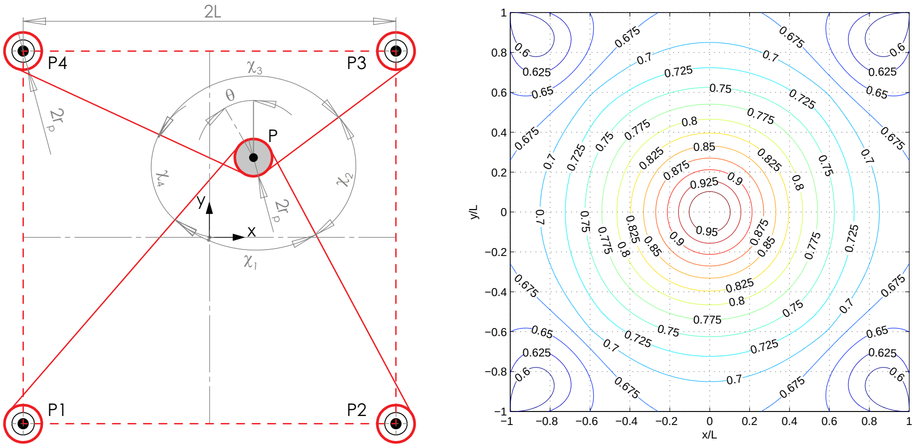

(a) (b)

Figure 3.7: Traditional design for a 4-cable, 3-DOF device [37] (a) and the corresponding dexterity index $\kappa(\bar{\mathbf{A}})^{-1}$ (b).

pulley [37]. Given the symmetry of the required useful region, the 4 pulleys are arranged on the vertexes of a square with side length $2L$. Also, the pulleys radius r_p is the same as the one of the moving platform, so that the configuration of the cables is independent of r[7] (Fig. 3.7(a)). This way, the only design parameter to be taken into account is L.

Figure 3.7(b) shows the contour lines of $\kappa(\bar{\mathbf{A}})^{-1}$ for the chosen subclass of devices. Intuitively, symmetries are due to the dexterity index being a function of the relative dispositions of the cables (as described by the angles χ_i in Fig. 3.7(a)). Indeed, symmetric poses share the same set of angles[8].

Moreover, we notice that the dexterity index decreases by increasing the distance from the workspace center. Thus, as in the traditional 2-DOF design, it is possible to consider the set of circumferences with center in the origin of the axes and radius $r \in [0, L]$, and, for each circumference, derive the *critical point* (i.e., the one yielding the minimum value of the index).

In this way, the relationship between $\kappa\left(\bar{\mathbf{A}}\right)^{-1}_{\min}$ and $(r_{REQ}/L)_{opt}$ can be portrayed on a *design diagram* as the one shown in Fig. 3.8(a). This diagram has been computed numerically, taking advantage of the symmetries of the system. Notice that Fig. 3.8(a) represents the counterpart of Fig. 3.3 for the 3-DOF system (with the new performance index $\kappa\left(\bar{\mathbf{A}}\right)^{-1}_{\min}$). Also notice that, being $(r_{REQ}/L)_{opt} \leq 1$, the value of $\kappa\left(\bar{\mathbf{A}}\right)^{-1}_{\min}$ is lower bounded.

The optimization problem can be summarized as follows:

---

[7] This is clear, since the direction of each cable would be parallel to the straight line connecting the center of the end-effector to the center of the corresponding pulley.

[8] From a geometrical point of view, each pair of normalized matrices $\bar{\mathbf{A}}$ corresponding to points that are symmetrical with respect to the x axis (or to the y axis) can always be rewritten in terms of two rotated frames with mutually symmetrical x' and y' axes (the remaining axes z' being opposite). The new representations of those matrices are the same (column permutations excepted), thus ensuring that the corresponding $\bar{\mathbf{A}}\bar{\mathbf{A}}^T$ are similar and, therefore, yield the same eigenvalues. With the same reasoning, it can be proved that the matrices $\bar{\mathbf{A}}\bar{\mathbf{A}}^T$ are similar even in the case of points being symmetric with respect to the bisectors.

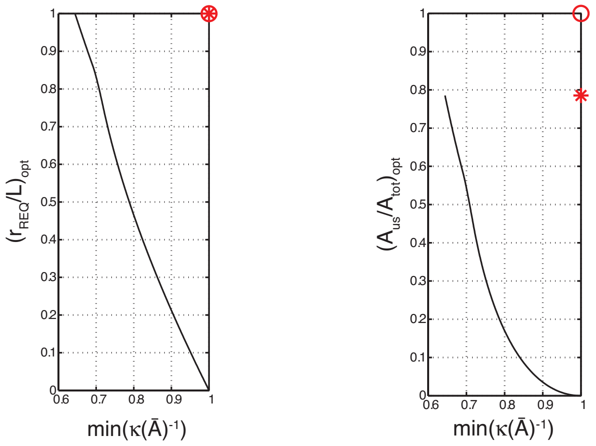

(a) (b)

Figure 3.8: Correlation between $\kappa\left(\bar{\mathbf{A}}\right)^{-1}_{\min}$ and $(r_{REQ}/L)_{opt}$ (a) and between $\kappa\left(\bar{\mathbf{A}}\right)^{-1}_{\min}$ and $(A_{us}/A_{tot})_{opt}$ (b). The corresponding data for the adaptive designs are represented by the red asterisk (square-like design) and by the red circle (circular design).

1. Use the diagram in Fig. 3.8(a) to compute $(r_{REQ}/L)_{opt}$ from the assigned value κ^{-1}_{REQ}
2. From the assigned value r_{REQ}, derive the design parameter: $L_{opt} = r_{REQ}\Big/(r_{REQ}/L)_{opt}$

The pulley radius r_p, not included in the optimization process, can then be chosen with additional considerations (e.g., the desired force performance for given actuators, the actual region of the workspace reachable by the centroid of the end-effector without colliding with the pulleys, the maximum desired impedance at the end effector, etc.).

In conclusion, we showed that the dexterity index is strictly related to the disposition of the cables. For this class of devices, the pulley axes of rotation being fixed, the only way to fulfill the design requirements is to opportunely scale the value of L. In this way, high values of κ^{-1}_{REQ} will result in *cumbersome* and *bad-tailored* designs.

3.3.2 Novel approach

We follow the steps outlined in Section 3.1.1.

step 1: Local performance index: $\kappa\left(\bar{\mathbf{A}}\right)^{-1}$; design criterion: $\kappa\left(\bar{\mathbf{A}}\right)^{-1} \geqslant \kappa^{-1}_{REQ}$

step 2a: Optimal configuration of the cables, yielding $\kappa\left(\bar{\mathbf{A}}\right)^{-1} = 1$ (i.e., isotropic design): $\chi_1 = \chi_2 = \chi_3 = \chi_4 = \pi/4$ (see Section 3.3).

step 2b: Target value for the performance index: $\kappa\left(\bar{\mathbf{A}}\right)^{-1} = 1$

step 3: The optimal configuration of the cables can be maintained in the whole workspace by means of two additional DOF. The simplest design solution is portrayed in Fig. 3.9(a). Each additional DOF provide the translation of a pair of opposite pulley-blocks along a coordinate axis, keeping the corresponding cables perpendicular to the coordinate axis. The minimum feasible length for each guide is $2r_{REQ}$. Therefore, if we neglect pulley/end-effector interferences, the ratio between the overall theoretical workspace and the useful one is $\left(A_{us}/A_{tot}\right)_{opt} = \pi/4$.

A better exploitation of the workspace is made possible with the device sketched in Fig. 3.9(b). Two orthogonal scissors mechanisms are employed to provide motion of both the pairs of pulleys along the same circumference of radius r_{REQ}. Notice that each mechanism can be actuated either at the slider (with a linear actuator) or at the pin joint (with a rotary actuator). The ratio between A_{us}/A_{tot} is now unitary, even though the length of each linear guide has to be $4L$.

step 4: The derivation of the pulley blocks trajectories for a given end-effector trajectory is straightforward. In fact, since the rotation of the end-effector has not effects on the motion of the pulley-blocks, only the trajectory of the centroid $x\left(s\right)$ and $y\left(s\right)$ must be taken into account (i.e., the planar curve described by (3.9)). Thus, for the adaptive device with a *square-like* workspace, the trajectory planning of the trolleys is written as:

$$\begin{cases} q_1\left(s\right) = x\left(s\right) \\ q_2\left(s\right) = y\left(s\right) \end{cases} \tag{3.26}$$

whereas, for the adaptive device with *circular* workspace, the trajectory planning is:

$$\begin{cases} q_1\left(s\right) = 2x\left(s\right) \\ q_2\left(s\right) = 2y\left(s\right) \end{cases} \tag{3.27a}$$

$$\begin{cases} \gamma_1\left(s\right) = 2\arccos\left(x\left(s\right)/r_{REQ}\right) \\ \gamma_2\left(s\right) = 2\arccos\left(y\left(s\right)/r_{REQ}\right) \end{cases} \tag{3.27b}$$

where (3.27a) and (3.27b) hold for the case of linear actuators and rotary actuators, respectively. The velocity and accelerations of the input variables q_i (or γ_i) can be calculated by following the same approach as the one presented in Section 3.2.2.

3.3.3 Comparison of the design results

In this design problem, we studied the dexterity of planar 3-DOF cable-based devices. Given the symmetry of the required workspace, we restricted the set of candidate designs to a subclass of traditional devices, having a square-like workspace. Moreover, to further simplify the design, a circular moving platform having the same radius as the pulleys was chosen. Under these assumptions, the configuration of the cables (and, therefore, the selected performance index) is not affected by the rotation of the end-effector.

With the traditional approach, for any given pair $\left(r_{REQ}, \kappa^{-1}_{REQ}\right)$, there exists a minimum value L_{opt} of the design parameter L satisfying the requirements. The dexterity of

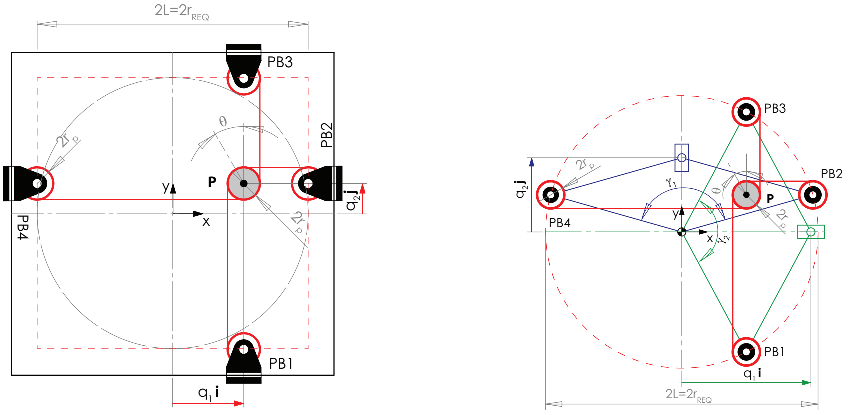

(a) (b)

Figure 3.9: Adaptive designs with *square-like* (a) and with *circular* (b) workspaces.

the device decreases with the distance from the center of the workspace - where the device is isotropic - following an almost linear relationship. Therefore, as the required degree of isotropy increases, say, from $\kappa_{REQ}^{-1} = 0.8$ to $.9$ (i.e., half the way to the maximum unitary value), the corresponding initial $(r_{REQ}/L)_{opt} \approx 0.465$ is approximately halved (Fig. 3.8(a)) and the corresponding initial $(A_{us}/A_{tot})_{opt} \approx 0.170$ is approximately reduced to one quarter (Fig. 3.8(b)).

Conversely, by adding two DOF, the resulting adaptive devices can be made kinematically isotropic over the required workspace, thus satisfying the condition $\kappa(\mathbf{A})^{-1} \geqslant \kappa_{REQ}^{-1}$. Indeed, the resulting Full-adaptive devices *are* isotropic, even when the required level of dexterity is moderate. In those cases, one additional DOF (i.e. only one pair of moving pulley-blocks) may be sufficient to satisfy the design requirements. Thus, one could design a Semi-adaptive device by following a similar method as the one described in Section 3.2.3. For the sake of brevity, this example is not reported here.

One final remark: even though both the adaptive designs yield $(r_{REQ}/L)_{opt} = 1$, the *circular* device gives the highest $(A_{us}/A_{tot})_{opt}$ ratio, as a consequence of the shape of the required workspace (Fig. 3.8(b)). However, this conclusion must be taken with caution, since it does not account for the space required for the motion of the sliders, which translate along two orthogonal, $4L$ long linear guides. Also, the *square-like* design is preferable for its simplicity, as opposed to the circular one which, for example, requires specific design solutions to avoid collisions between the scissor mechanisms.

3.4 Conclusion

In this Chapter a systematic methodology for the optimal design of a novel subclass of cable-based devices was described. This novel subclass, defined here as *Adaptive Cable-Driven Systems*, leads to more *effective* solutions for given design requirements. The main contribution of this work is to change the design criterion from a *global* performance index to a configuration-dependent *local* index. Here the term *adaptive* refers to the capability of modifying in real-time the configuration of the cable entry points to maximize the local index throughout the workspace. If a complete decoupling between the end-effector pose and the (optimal) cables configuration is achieved, the devices is defined as *Fully-adaptive*. If, on the other hand, the disposition of the cables can only be kept inside an acceptable set, the device is defined as *Semi-adaptive*.

Most of the kinematic and inertial properties reduced to the end-effector are strictly dependent on the structure matrix $\boldsymbol{A}$, which is configuration-dependent. For this reason, the existing design methods, which measure the effectiveness of a design solution based on global indices (or local indices averaged over a reference region of the workspace), usually fail to obtain *well-tailored* design solutions.

To obtain more effective designs, by following the method proposed here one must deduce the feasible set of cable configuration first (i.e., the one yielding acceptable values of a given local performance index), and then keep the actual cable configuration inside this set throughout the whole required workspace. This goal is achieved by choosing a suitable set of *sliding directions or surfaces* for the pulley-blocks, and by implementing a proper trajectory planning algorithm to adapt their configuration to that of the moving platform, thus making the system *adaptive*.

Two simple case-studies have been inspected with the aim to emphasize the advantages of the proposed method over the traditional one. It is believed that the complexity brought into the system by the introduction of additional active DOFs might be entirely balanced by the reduction in the required sizes of the pulley motors and in the dimensions of the device.

The proposed design method can be thought of as an application to cable-based devices of the general framework introduced by Gosselin in [95]. The novel method differs from the previous one in that it accommodates for the specific features of cable-based systems. Following the related Literature, the design goal is defined here through a specific performance index. The conditions for adaptiveness are inferred through a geometric approach and, in general, do not show explicit dependence on the design parameters. Therefore, deriving the design rules is the hardest step of the design process, and involves both an optimization of the mechanical structure and a proper planning and control strategy.

This work presented only proof-of-concept results related to the application of the new design approach. Further inspection needs to be carried out, especially on the derivation of feasible design rules for complex designs with non-point-mass end-effectors. The solution to this process may not be unique and it highly relies on the designer's skills and experience. It is expected that, as the number of DOFs required at the end-effector increases, a certain level of adaptiveness should also be provided at the end-effector to reduce the overall complexity of the system.

This methodology was first validated through the development of the *Sophia-3* prototype. This device is described in detail throughout the following chapters.

CHAPTER 4

Design of Sophia-3

The Sophia-3 (String Operated Planar Haptic Interface for the Arm-rehabilitation) is a planar, point-mass cable-driven device, with a tilting working plane. The prototype is conceived as a rehabilitation robot to be employed in the decentralized health-care treatment of chronic post-stroke patients. Thus, cost-effectiveness, ease of use and transportability are the key points of the prototype.

Sophia-3 is actually an evolution of a previous prototype, named Sophia-4 [72, 73], with which it shares many features. Nonetheless, several significant improvements have been introduced in the new design, such as the variable inclination of the working plane, the elimination of the fixed attaching points at the base and the introduction of a moving pulley-block, which allows Sophia-3 to achieve similar force capabilities as those of Sophia-4, despite having one less cable installed.

From the design point of view, Sophia-3 is the first example of Semi-adaptive cable-based device. Indeed, its layout has been determined following the methodology described in Chapter 3, and taking the isotropic force i_F as the optimization criterion. The resulting design is highly integrated: all the dimensions of the device have been optimized to increase compactness while still guaranteeing easy accessibility to the patient [96].

In this Chapter, a detailed description of the prototype is given, dealing with layout definition, mechanical design and electrical design.

4.1 Definition of the layout

In Section 3.2 a Semi-adaptive design with trapezoidal layout was recognized as a good compromise between force performances/compactness and design complexity. As a matter of fact, introducing a single auxiliary DOF into the system (i.e., the translation of the lower pulley-block along a straight line) brought about some significant improvements in the robot performances (Fig. 3.3, and Fig. 3.4). In the development of Sophia-3, the Semi-adaptive design was preferred to the Fully-adaptive ones, since the aim was to build a *cost-effective* and *compact* rehabilitation device.

Clearly, the trapezoidal configuration is not the only possible choice for a planar translational semi-adaptive design. For example, one could choose a different shape and/or a different disposition for the linear guide. Moreover, the geometrical constraints outlined in Fig. 3.3 are likely to be modified in the development of a real prototype, since the designer has to cope with other, more stringent limitations (e.g., motor housings, patient's workspace, accessibility and usability of the machine, etc.). For these reasons, a software was implemented (Fig. 4.3(a)) which allowed to study the force performance deriving from arbitrary layouts.

In this software, the algorithms for calculating the manipulability index i_F were slightly

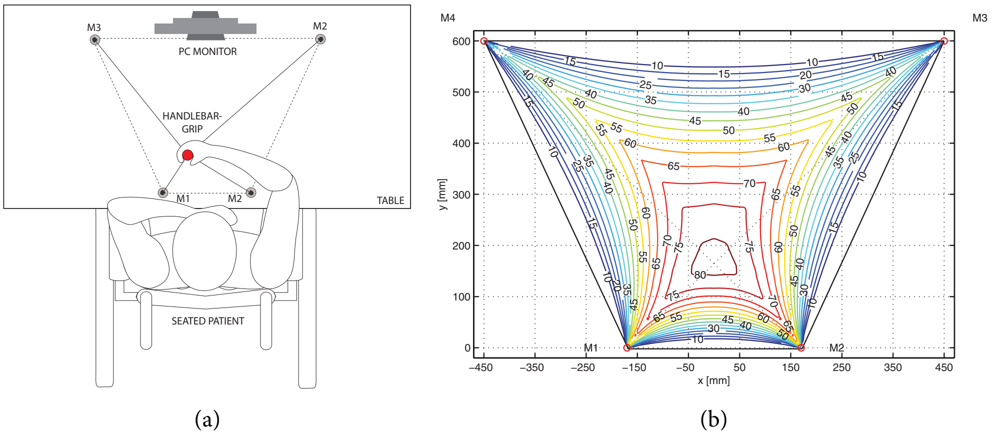

Figure 4.1: Layout of Sophia-4 (a) and contour plot of the force index i_F [N], calculated with $f_{\max} = 87N$ and $f_{\min} = 5N$ (b). The maximum isotropic force is greater than 60N inside most of the workspace.

modified to allow for non-zero values of $f_{\min}$ and arbitrary $f_{\max}$[1]. The use of this software allowed to compare the force performance of Sophia-4 with those of the new prototype. The design of Sophia-3 was therefore optimized so as to guarantee similar force capabilities as those of Sophia-4. In this way, not only the best layout, but also the set of motors yielding the desired force performances were identified. Not surprisingly, it turned out that this *semi-adaptive* configuration leads to further advantages, even over the design of Sophia-4 (i.e., the standard design with one 4 cables), in terms of compactness, workspace exploitation, cable interference, perceived mass, power dissipation and kinematic isotropy [76]. In the following, the results of the aforementioned layout analysis are briefly discussed.

Fig. 4.1(a) and Fig. 4.2(a) show concept drawings of the Sophia devices. In both systems the patient, while sitting on a wheelchair, holds a handlebar-grip that can be moved over a flat horizontal surface. The driven cables are all attached to a single point of the end-effector, so the devices are capable of exerting only pure forces on the patient's hand. The handlebar-grip itself is mounted on the base of the end-effector by means of a ball bearing, in such a way that no moment can be transmitted to the patient's hand along the axis orthogonal to the base. The output force is computed in real-time by a high-level controller, while the end-effector position and the cable tensions are calculated by a low-level controller. The data on the status of the current exercise, together with a real-time visual feedback, are displayed on a PC monitor in front of the patient.

In the case of planar cable-driven point-mass devices, the statics workspace coincides with the *convex hull* of the cable attachment points [52] (see Section 3.2.1). Therefore, once the number of cables has been decided, the position of the pulley-blocks can be adjusted to match the patient's reachable workspace. However, as already pointed out in the previous chapters, force performances are also dependent on the end-effector position within the stat-

---

[1] In real devices, a minimum value $f_{\min} > 0$ must be imposed to prevent cable slackening due to motor accelerations and non modelized friction effects. Also, defining specific values of $f_{\max}$ for each motor may be useful to moderately adjust the performances of the robot once its layout has already been defined.

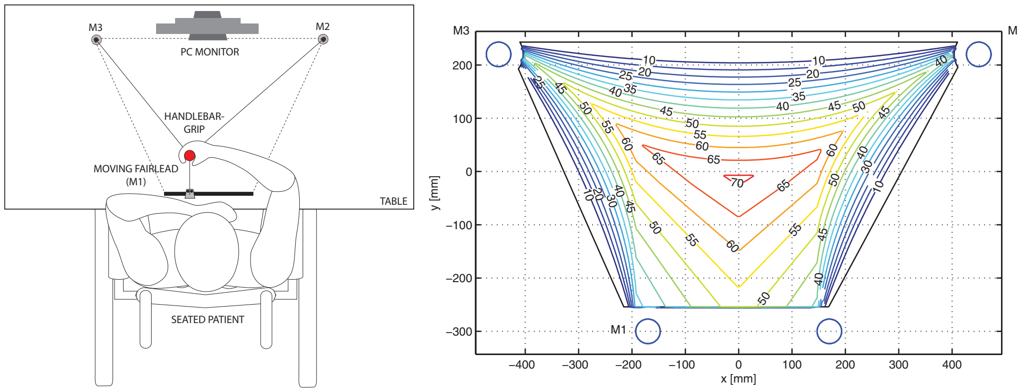

(a)

(b)

Figure 4.2: Layout of Sophia-3 (a) and contour plot of the force index i_F [N] (b). The reduced number of actuators yields smaller i_F as compared to Sophia-4. Yet, a static force greater than $50N$ is still obtained inside most of the workspace.

ics workspace, thereby the useful workspace[2] may be significantly smaller than the theoretical one. For planar point-mass devices, we have already introduced the module of the maximum isotropic force i_F (Section 2.1) to quantify the force capabilities all through the workspace. This performance index is particularly significant in the development of interacting robots, since the force the device will produce during the execution of a rehabilitation exercise is not predictable, as it depends not only on the implemented exercise but also and mainly on patient's behavior.

Figure 4.1(b) shows the contour plot of i_F and the layout of pulley-blocks for Sophia-4, with the following constraints on the tensions in cables: $f_{\text{min}} = 5N$, $f_{\text{max}} = 87N$. Comparable force capabilities can be maintained even with 2 upper pulley-blocks and one lower pulley-block, provided that the latter can be moved according to the position of the end-effector [76]. The final design of Sophia-3 takes advantage of this concept: the lower pulley-blocks have been substituted with a moving pulley-block, whose range of motion equals the length of the lower base in the previous design. The height of the trapezium has been reduced in order to move the most favorable region of the workspace closer to the patient. The dimensions of the workspace are similar to those of Sophia-4 (Tab. 4.1).

Figure 4.2(b) shows the resulting i_F diagram, obtained by moving the lower pulley block to track the x position of the end-effector. In this way, the lower cable is kept orthogonal to the guide, unless an extremity of the travel is reached (Section 3.2.3).

By comparing figure 4.1(b) and figure 4.2(b), it can be noticed that the useful region of the workspace (i.e., $i_F \geq 50N$), even though slightly smaller in Sophia-3, is still suitable. The second scheme is preferable in that the lower portion of the workspace is much better in terms of force capabilities. Indeed, the boundary effect caused by the alignment of the lower cables is totally eliminated near the linear guide. Moreover, the reduced number of cables allows for more free motions of the patient's arm in the same portion of the workspace, with

---

[2] In this contest, we indicate as the useful workspace the region of the statics workspace wherein the force index i_F is greater than a given threshold, i.e., $i_F \geq 50\text{N}$.

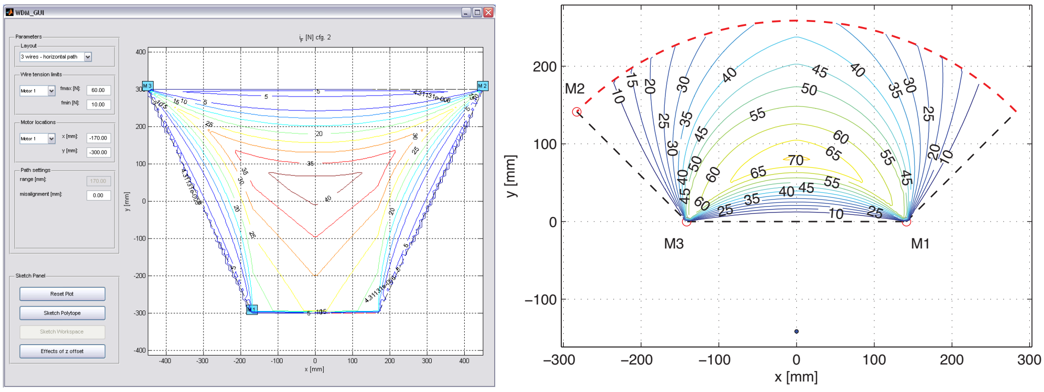

Layout: 3 wires - horizontal path
Wire tension limits: Motor 1, fmax [N]: 60.00, fmin [N]: 10.00
Motor locations: Motor 1, x [mm]: -170.00, y [mm]: -300.00
Path settings: range [mm]: 170.00, misalignment [mm]: 0.00

(a) (b)

Figure 4.3: The GUI of the software employed to study different layout solutions (a) and contour plot of the force index i_F [N] for a circular guide(b).

no possibility of cable-arm interference.

Moving the lower pulley-block along a straight-line guide does not represent the only possible choice. Thanks to the simulation software, several shapes and dispositions for the moving platform were studied. One of the possible alternative layout is depicted in Fig. 4.3(b). The guide (dashed red line) is located opposite to the patient, and consists in an arc of circle. As in the case of the straight-line guide, the moving-block follows the position of the end-effector while keeping orthogonality between the guide and the corresponding cable (therefore, the cable is always aligned in a radial direction). The disposition of the contour lines is approximately circular, with the concavity being oriented towards the patient (Fig. 4.3(b)). Hence, the workspace of the machine is similar to the operator's one, thereby allowing for a more effective use of the device capabilities. In addition, the location of the circular guide allows the moving pulley-block to keep the wire in a radial direction for each pose of the end-effector within the workspace. The force polytopes (see Section 1.3) are approximately regular, especially in the central region, which indicates a better isotropy in the force capabilities than the previous layouts.

On the other hand, the drawbacks are the small values of the force performances as compared to those of the trapezoidal layout, the complexity of the design and the necessity for the operator to seat in front of the fixed pulley-blocks, thereby reducing his/her free movements.

In conclusion, from the performed layout analysis the Semi-adaptive design with trape-

Table 4.1: Overall dimensions of Sophia-4 and Sophia-3

	Sophia-4	Sophia-3
Lower base [mm]	340	340 (travel of P-B1)
Upper base [mm]	900	900
Height [mm]	600	500

zoidal workspace proved to be the best compromise between performances and ease of design. However, all the other design parameters being equal, having 3 cables installed instead of 4 implies a reduction in the force performances. To partially compensate for this problem, the brushed DC motors installed in Sophia-4 have been replaced by larger brushless motors in the new prototype.

4.2 Sophia-3: design overview

Figure 4.4: The Sophia-3 prototype

The mechanical structure of Sophia-3 consists of a wooden table supported by an aluminum frame (Fig. 4.4). The aluminum frame is made of commercially available modular elements, with the aim of reducing costs and weights. To facilitate the displacements of the device, wheels have been installed on the bottom of each table leg. The compact, integrated design lets the device be easily moved inside houses and hospital corridors.

The table can rotate around a fixed longitudinal axis, located under the table, next to the patient's legs. Table orientation can be varied in the range $0 - 60°$ to change the kinematics of the exercises: the patient can be exercised in moving the hand over a rising surface. For this purpose, two parallel four-bar linkages are installed underneath the table, whose dimensions have been calculated through numerical optimization.

An aluminum handbar-grip can be moved on the table surface, sliding on low-friction PTFE discs. To further reduce friction, a PTFE cover is to be mounted over the wooden surface, and pulley blocks have been eliminated. As a consequence, pulleys and motors have been moved upward, next to the plane of motion. Three cables are connected to the same point in the axis of the end-effector, such that no moments can be exerted at this interface. Also, the grip of the end-effector is connected to the base element via a rolling bearing, so as to avoid transmission of dumping moments. More powerful DC brushless motors actuate the pulleys. The linear motion of the lower pulley block is achieved through a miniature ball screw. Optical encoders are used for forward kinematics, while the tension in each cable is controlled by commanding the winding current.

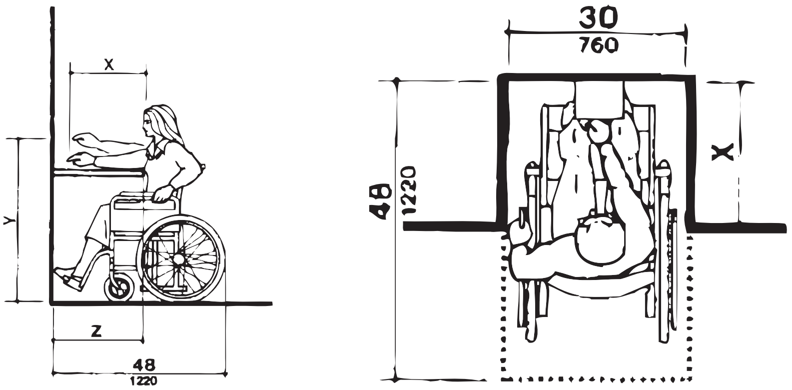

(a) (b)

Figure 4.5: Minimum required space according to the Uniform Federal Accessibility Standards [96]: front (a) and top (b) dimensions.

The electric cabinet has been integrated between the right legs of the structure. Power and feedback wirings pass through a plastic cable carrier and reach the bottom of the table. All the other components are mounted on the bottom surface of the table, or partially embedded in it. All dimensions have been chosen to guarantee accessibility to the subject, according to the UFAS requirements [96].

4.3 The main frame

The prototype has been conceived to be easily usable by patients seated on a wheelchair. Thus, the guidelines published by the *Uniform Federal Accessibility Standards* (UFAS [96]) have been adopted to identify the critical dimension that could potentially hinder the patient from safely using the machine. Even though these standards apply to architectural features, the identified requirements were found to be very close to the designer's needs.

The shortest side of the table is set to 620 mm. Given the value of x (Fig. 4.5(a)), the Federal Standards suggest to choose z such that $z \leq x$. After a brief survey on commercially available wheelchairs, the aforementioned value was chosen.

Fig. 4.5(b) describes the minimum free surface required by a seated patient to easily approach an object (frontally or laterally). The suggested surface (760 × 1220 mm) has been slightly reduced, since in this application the subject should approach the table only frontally.

Fig. 4.6(a) shows the final sizes of the main frame. It should be noticed that the corner support elements limit the available free space under the table. Since commercially available wheelchairs are less than 500 mm wide, if we choose $a = b$ to have the patient centered in the workspace, the resulting constraint is $a, b \leq 302$ mm. With $a = b = 250$ mm, the patient's legs are sufficiently far from the fixed pulley-blocks, thus preventing any contact between the upper motors and the patient. As for the table height, [96] suggest that the distance between the table and the floor should be $750 \div 800$ mm for the upper surface and should be $720 \div 730$ mm at least for the bottom surface.

Fig. 4.6(b) show a CAD plot of the main frame. The structure is composed of modular

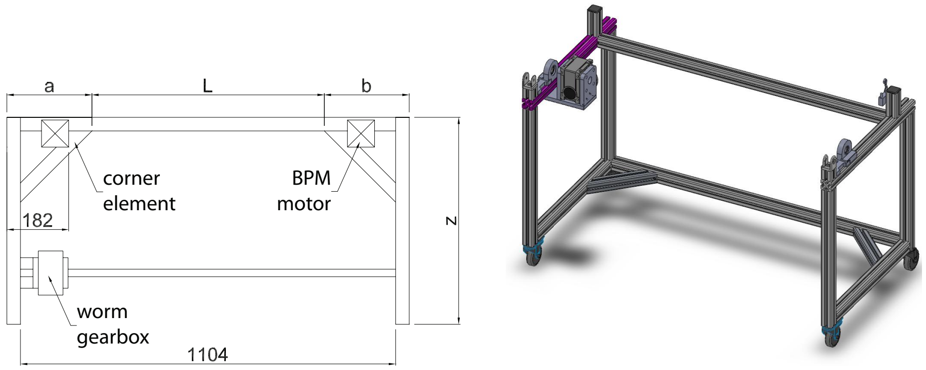

(a) (b)

Figure 4.6: Top view (a) and CAD rendering of the main frame (b).

profiles (Item Industrietechnik GmbH) made of hardened aluminum alloy, whose mechanical properties are outlined in Tab. 4.2. Static Finite Element analyses based on overestimated loads were carried out to verify the cross-section of the profiles.

4.3.1 Fixed pulley blocks: motors sizing & selection

The cable-based robot is controlled by four BPM (brushless permanent magnet) motors. Two motors are located in the upper corners of the workspace, whereas the motor controlling the lower pulley can translate along a straight line guide thanks to the fourth motor, acting on a ball screw. As compared to brushed DC motors with similar performances, BPM motors are characterized by lower rotor inertia, since the rotor carries the magnets and the windings are located at the stator. Other advantages are the almost horizontal torque/speed curve, a good dynamic response and a reduced weight. Choosing BPM motors helps to reduce the equivalent inertia seen at the end-effector and to decrease the weight of the tilting table. On the other side, higher design costs have to be expected. The servomotors produced by LS Mecapion were identified as a good compromise between performances and cost.

Fig. 4.2(b) shows the disposition of the upper pulleys. To choose a suitable size for those motors, we verified that the worst working condition falls inside the continuous operating region of the motor. Thus, the motor will be able to withstand the highest estimated loads for long time intervals, without thermal issues. Although this may imply motor oversizing, we adopted this approach since the static and dynamic loads acting on each motor cannot be determined precisely, being highly dependent on the patient's skills. The characteristics of

Alloy	R_m	$R_{p0.2}$	ρ	A_5	E
	$[MPa]$	$[MPa]$	$[\frac{kg}{dm^3}]$	$[\%]$	$[MPa]$
Al Mg Si 0.5 F 25	245	195	2.7	10	70

Table 4.2: Mechanical properties of the extruded profiles

P_n	M_n/M_{max}	n_n/n_{max}	J_m	mass
$[kW]$	$[N \cdot m]$	$[rpm]$	$[kg \cdot cm^2]$	$[kg]$
0.45	2.15/ 6.44	2000/ 3000	1.092	2.52

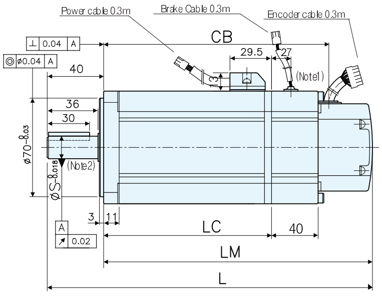

Figure 4.7: Main characteristics of the APM SC05D servomotor

the BPM motor chosen for the upper pulleys (APM SC05D) are outlined in Tab. 4.7. Being the pulley radius equal to $r_p = 23\ mm$, the servomotor is capable of providing a continuous static tension $f_{\max} = 94\ N$ on the corresponding cable, thus guaranteeing slightly higher values of the manipulability index i_F than those depicted in Fig. 4.2(b). Also, if we consider a maximum linear speed $v = 1\ ms^{-1}$ at the end effector, the corresponding rotational speed ($\approx 415\ rpm$) lets the working point fall into the continuous operating region of the motor.

From the design point of view, the pulleys have been brought to the top surface of the table, with the axes of rotation being orthogonal to the plane of motion. As compared to the design of Sophia-4, where the motors were located underneath the table (Fig. 1.12) and cables have to pass through two idle pulleys before reaching the working plane, the new solution has the great advantage of reducing friction. However, having removed the fixed attaching point to the ground, the kinematics of the device becomes more complicated, as it will be illustrated in Section 5.6.1.

To increase compactness, the fixed pulley blocks are partially embedded in the table through a *drawer-like* fixture (Fig. 4.8). The servomotor is first fixed to an aluminum flange, and then the whole assembly slides into the wooden table, and is secured by means of screws. All the fillets are made on the metal plate, so that the whole assembly may be unmounted without problems. A wooden cover is finally used to hide the flange, so that only the driven pulley emerges from the working plane. As it is shown in Fig. 4.8, the servomotors are equipped with an optical encoder (2500 P/R) and a brake. The latter has the function of prevent cable slackening when the device is turned off. Also, the brakes act as safety devices, since they are activated whenever a fault is detected. The flange and the fasteners have been statically verified. Being the safety coefficients very large, no fatigue analysis were conducted on these components.

4.4 The moving pulley-block subassembly

The moving pulley-block subassembly is depicted in Fig. 4.13. This subassembly is mounted on the wooden surface by using the same *drawer-like* concept described previously (Fig. 4.8). The moving pulley-block is composed of a pulley ($r_p = 23\ mm$), a worm gearbox (GYSIN GSR 25) a servomotor (APM SA01A) and a custom-made carriage made of 7075 aluminum alloy (*Ergal*). The nut of a recirculating ball screw (SKF 12.7x12.7R) and the carriage of a profiled linear guideway (SCHNEEBERGER MN9) are mounted on the same aluminum element. The linear motion is provided by another servomotor (APM SB02A) that actuates the

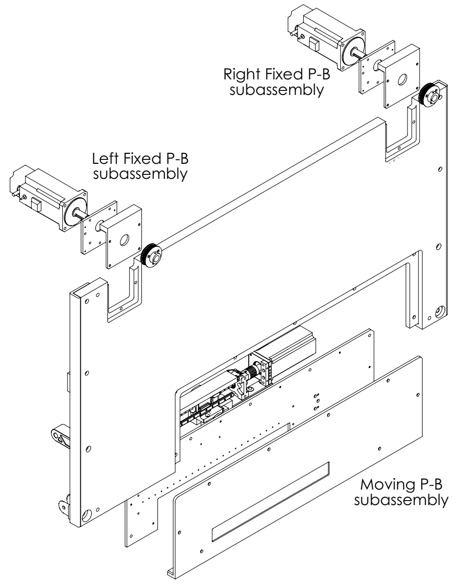

Figure 4.8: Drawer-like design solutions for the fixed pulley-block and the moving pulley-block subassemblies

screw. An elastic coupling (R+W MK1/45 miniature bellows coupling) reduces the effects of the misalignments between the shaft of the motor and the screw. The linear guideway has the function of reducing the radial loads acting on the screw. In the following, we will briefly describe how the single elements have been selected.

As standard power screws, ball screws translate rotational motion to linear motion. A threaded shaft which acts as a precision screw provides a spiral raceway for ball bearings. Ball screws are able to apply high thrust loads with minimum internal friction. Depending upon their lead angle, ball screws can be *back-driven*. The precision ball screws used in robotics usually show an efficiency $\eta \geq 90\%$. In high-precision applications, ball screws can operate with some preload, whose function is to eliminate backlash. To select the most suitable ball screw, one must consider the following key-points:

- Dynamic axial load capacity C_a
- Static axial load capacity C_{0a}

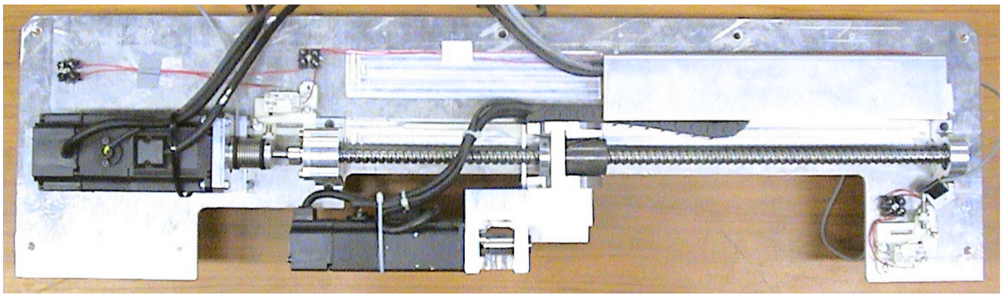

Figure 4.9: Bottom view of the moving pulley-block subassembly

designation	d_0/ P_h	C_a/C_{0a}	play
	$[mm]$	$[kN]$	$[mm]$
SH 12,7 x 12,7 R	12.7/ 12.7	5.3/ 9.0	0.03

Figure 4.10: SKF miniature screw specifications

- Radial loads
- Stiffness
- Axial tip load P_B
- Critical speed n_k
- Speed limit $n_{\max}$

In our application, the axial load is almost null, except when the pulley-block is stationary at one of the extreme points of the linear guide. Still, in the latter condition the axial loads are quite low (simulations indicates $F \simeq 34N$). For this reason, the first two points and the axial tip load have been neglected. Ball screws are not meant to withstand large radial loads. Yet, radial forces up to $0.05C_a$ may be applied. This issue was addressed by installing a linear guideway.

Stiffness is a major concern in precision positioning, because it strongly reduces the backlash when reverting the direction of motion. In principle, stiffness can be increased by installing *preloaded units* (e.g., nuts with oversized spheres or two opposed semi-nuts). However, this approach also increases the friction drag torque and thereby the wear. For this reason, the selected nut has a reduced play ($0.03mm$) without preload.

To increase the critical speed, we adopted a *fixed-supported* configuration (i.e., a pair of rolling bearings in back-to-back configuration for the motor side of the screw and a floating bearing on the opposed side). In this way, we obtained $n_k \approx 5900rpm$, which is far greater than the expected operating speed ($\approx 3550rpm$, which corresponds to a linear velocity of $0.75ms^{-1}$).

When the rotating balls reach one extremity of the nut, they are conveyed inside a special raceway called *liner*. The passing of the balls inside the liner generates an axial acceleration and, thereby, corresponding inertial loads. For this reason there is an upper bound in the maximum feasible speed. Indeed, this is the limiting factor for this application, which forced to select a large value for the pitch. At the same time, the diameter of the screw should be limited to reduce the inertial loads on the motor. For this reason, we selected a ball screw with $p = 12.7mm$ and $d_0 = 12.7mm$ (SKF 12.7X12.7R, Fig. 4.10). With this design, we get $n_{\max} \approx 3940rpm$, which is sufficiently greater than the expected operating speed. The total length ($550mm$) allows to handle a maximum displacement of $490mm$, which is larger than the required one ($340mm$).

Radial loads have to be expected due to the tension carried by the lower cable. A linear low-friction guideway (SCHNEEBERGER MINIRAIL MN9) was selected to sustain these loads

designation	$C_0/\ C$	$M_{0Q}/M_{0L}/M_Q/M_L$
	$[N]$	$[Nm]$
MN 9	2770/1690	12.9/10.2/7.9/6.2

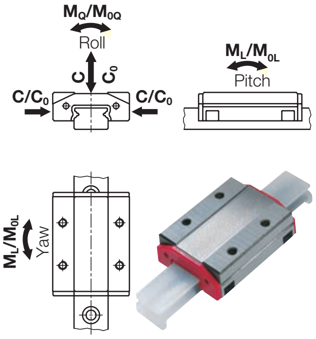

Figure 4.11: Schneeberger minirail specifications

(Fig. 4.11). The centroid of the corresponding carriage is approximately aligned with a plane orthogonal to the direction of motion and tangent to the left side of the lower pulley (i.e., the plane that contains the lower cable in nominal conditions). Thus, the loads acting on the carriage are reduced, and can be withstood by a single unit. A preloaded carriage (grade V1) was selected to improve stiffness, position accuracy and loading capability. For a nominal travel of $340mm$, the G1 accuracy class limits the transversal deviance to $4\mu m$, which is far enough for our application. For the mounting of the carriage and the guideway on the corresponding housings, reference surfaces were predisposed.

Similarly to the fixed pulley-block assemblies, the moving pulley-block assembly uses a compact *drawer-like* mounting. Thus, the occupied vertical space is strongly reduced and there is no chance for the moving trolley to hurt the patient. In order to compensate the axial radial and angular misalignments between the screw and the shaft of the servomotor, an elastic coupling was inserted (Fig. 4.12).

It turned out that it was impossible to support the ball screw by means of a pair of angular contact bearings mounted in opposition. Indeed, to guarantee the minimum axial load they would have needed to be mounted with preloaded springs, which are not suitable for precision positioning. Therefore, we chose a *fixed-supported* configuration, where a floating ball bearing sustains the extremity of the screw which is far from the servomotor. The other extremity must provide an axial constraint. Double-row, angular contact axial bearings are available for this purpose (e.g., ZKLN1034 - 2Z). However, they generate high drag torques, such that the screw servomotor had to use approximately $1/3 \times M_n$ only to oppose friction. Thus, we decided for a pair of radial ball bearings (638-2RZ) mounted in *back-to-back* configuration. In this way, however, the maximum allowable axial load decreases as well as the drag torque. The custom-made aluminum housing assembly is depicted in Fig. 4.13 (right side): the outer rings of the bearings are axially constrained by means of a separate cover and a shoulder realized on the main housing. The inner rings, on the other side, are constrained by a shoulder realized on the screw and by a spacer which is kept in place by a custom made nut. As for the floating

designation	$M_{\max}$	k_τ	$\Delta_{ax}/\Delta_{lat}/\Delta_{ang}$
	$[Nm]$	$[Nm/rad]$	$[mm]/[deg]$
MK1 45	45	7000	0.7/0.2/1.5

Figure 4.12: R+W miniature bellows coupling specifications

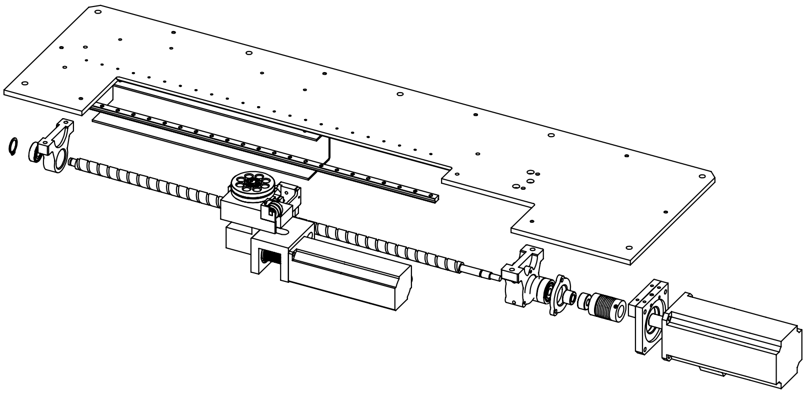

Figure 4.13: Moving pulley-block subassembly, exploded view

support, needle bearings could not be installed for space issues. Thus, we chose a radial ball bearing (608-2Z) whose inner ring has been forced on the axially free extremity of the screw. All the supports were verified by imposing the worse loading conditions.

4.4.1 Recirculating ball-screw servomotor

Through the *Principle of virtual work* one derives the following estimate of the torque required at the beginning of each motion:

$$c_m = \ddot{x}\left[J_m \cdot k_s + (J_s + J_j) \cdot k_s + \frac{m_{tot}}{k_s}\right] + C_a + M_{RLl} + M_{RLr} \tag{4.1}$$

where J_m, J_s, J_j are the moment of inertia (w.r.t. the axis of rotation) of the servomotor, of the screw, and of the elastic coupling, respectively. C_a is the drag torque due to a possible preload of the screw, M_{RLl} and M_{RLr} are the friction torques due to the left and right ball bearings. With a raw estimate of the translating mass ($m \approx 1.5kg$) and having set the nominal operating linear acceleration to $\ddot{x} = 7.5m/s^2$, the result is $c_m = 132mNm$. As for the fixed pulley-block servomotors, we selected the BPM motor so that the worse-case working point fell inside the continuous operating region of the motor characteristic curves. The main characteristics of the selected device (APM SB02A) are reported in Fig. 4.14

4.4.2 Moving pulley servomotor

To reduce the occupied volume and the translating mass as much as possible, the servomotor actuating the lower pulley-block was initially equipped with a worm gearbox. Clearly,

P_n	M_n/M_{max}	n_n/n_{max}	J_m	mass
$[kW]$	$[N \cdot m]$	$[rpm]$	$[kg \cdot cm^2]$	$[kg]$
0.2	0.637/ 1.912	3000/ 5000	0.182	1.08

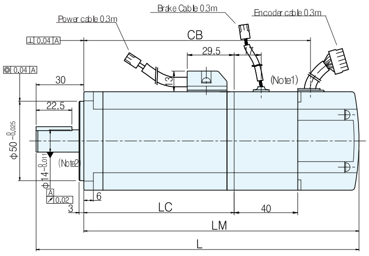

Figure 4.14: Main characteristics of the APM SB02A servomotor

P_n	M_n/M_{max}	n_n/n_{max}	J_m	mass
$[kW]$	$[N \cdot m]$	$[rpm]$	$[kg \cdot cm^2]$	$[kg]$
0.1	0.318/ 0.955	3000/ 5000	0.045	0.5

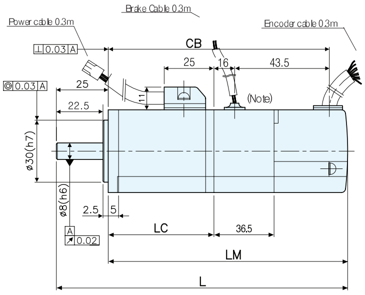

Figure 4.15: Main characteristics of the APM SA01A servomotor

the introduction of a reducer increases the equivalent inertia perceived at the end-effector, so that the reduction ratio should be kept as small as possible. Also, the worm gear introduces backlash and additional friction in the device. In the fixed pulley-blocks, the winding current is used to estimate the force exerted in the corresponding cable, thereby the motors can be controlled in current/torque mode. This approach is feasible as long as the pulley is directly keyed on the motor shaft. As it will be discussed in the following chapter, the use of the gearbox was accepted, under the hypothesis that the lower pulley could be controlled in position mode (Section 5.6). However, first experimental tests showed that this hypothesis was completely wrong, so that the lower pulley-block assembly was partially redesigned. In the following, a brief description of the old and the new designs is reported.

To choose a suitable pair motor+gearbox we impose that the lower pulley-block has comparable characteristics as those of the fixed pulley block (i.e., $f_{\max} = 94\ N$). The servomotor APM SA01A (Fig. 4.15) is sufficiently small and light to be mounted on a moving trolley. With the usual pulley ($r_p = 23\ mm$) the required $f_{\max}$ is approximately achieved with a reduction ratio of 7:1. The installed worm gearbox (GSR 25, Fig. 4.16) was chosen for its compactness and for the capability to withstand high radial loads. The entire gearmotor is fixed on the custom-made moving trolley by means of three screws. We also verified that the gearmotor is capable of exerting the required force in the cable in the worst dynamic conditions ($\dot{x} = 0.75ms^{-1}$, $\ddot{x} = 7.5ms^{-2}$).

After the device was assembled, first experimental tests proved that the lower pulley-block could not be controlled in torque mode. Therefore, this subassembly was partially redesigned. Fig. 4.17 shows a picture of the new design solution. The previous moving trolley was kept, while the worm gearbox was substituted by a custom made housings made of 7075 aluminum alloy (*Ergal*) whose size are approximately the same as those of the gearbox.

The motor shaft acts on a custom-made screw ($p = 1.5mm$, $d_0 = 16mm$) whose nominal diameter was chosen so as to enhance the feasible range of tensions in the cable. The latter is wound on the screw, passes through a idle pulley which guides the cable to the upper surface

designation	k	η	$M_n/M_{\max}$	$n_n/n_{\max}$	$F_{r,\max}$
	[1]	[1]	$[Nm]$	$[rpm]$	$[N]$
GSR 25	7	0.80	5/10	4000/6000	150

Figure 4.16: Main characteristics of the Gysin worm gearbox

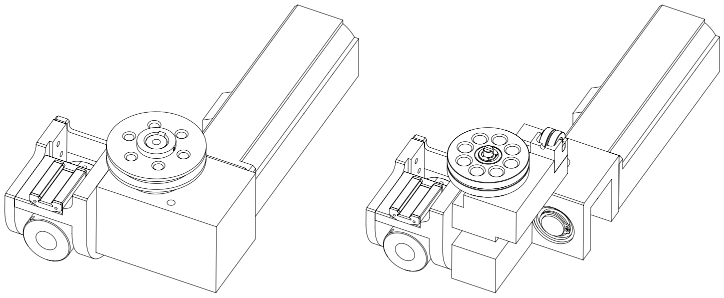
(a) (b)

Figure 4.17: Moving pulley-block: previous design (a) and new design (b)

of the table and finally reaches the main pulley (Fig. 4.17). A ball bearing supports the screw (61902), whereas a single needle roller bearing is forced on the main pulley (NKI 6-12 TN). A roller bearing without inner ring (RNAO 5x10x8 TN) was employed for the small idle pulley. As compared to the gearmotor assembly, friction is strongly reduced. However, the installed motor is capable of guaranteeing the worst working conditions by a limited amount of time. With this arrangement, the travel of the lower pulley remains approximately the same.

4.5 The four bar linkage

To change the kinematics of the exercises, the table orientation should be varied in the range $0 \div 60°$, so that the patient can be trained in moving the hand over a rising surface. For this purpose, two parallel *four-bar linkages* were designed. During the motion, all the links remain underneath the table, so as to avoid collisions with obstacles located around the table. The kinematic chain was been designed through an optimization algorithm implemented in MATLAB, with the aim of minimizing the RMS torque required at the crank.

To get an estimate of the required torque, we considered the gravitational contributes given by the table and all the devices mounted on it (fixed pulley-blocks assemblies, moving pulley-block assembly, drives, etc). We also considered the patient's hand and forearm as additional weights to be supported. As for the biomechanical data, the patient's model was assumed as the average adult male [71]. Finally, as the reference movement used to estimate the inertial loads, we consider a complete motion of the table (range $0 \div 60°$) to be completed in $\Delta t = 10s$ with a trapezoidal (symmetric) velocity profile[3].

Fig. 4.19 show the kinematic scheme of the four bar linkage: $a1$ is the crank length, $a2$ is the connecting rod length, $t1$, $t2$ and $t3$ form the rocker (which is fixed to the wooden table), while Dx and Dy define the relative position of the pin joint connected to the main frame.

The optimization algorithm uses $a1$ and $t1$ as fixed parameters, and defines the optimal set of link lengths that minimizes the RMS of the required torque. All the link lengths are allowed to vary inside a specific feasible range of values. Thus, the design of the kinematic

---

[3] Although this trajectory planning is arbitrary, it was useful to give insight on the relative importance of the inertial contributions in the resistive torque. It turned out that inertial loads are negligible if compared to the gravitational contributions.

Dx	Dy	$t1$	$t2$	$t3$	$a1$	$a2$
131.2	30	25	55	185	60.7	114.7

Figure 4.18: optimized link lengths [mm]

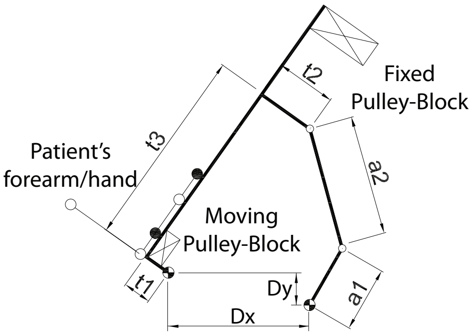

Figure 4.19: kinematic scheme

chain was turned into a *constrained optimization problem*, where the constraints are the feasible range of values for each link length and the cost function is the RMS of the resistive torque (for a complete movement $0 \div 60°$). Additionally, we imposed the alignment of the crank and the connecting rod both at the starting and at the goal position, thereby guaranteeing the maximum reduction ratio in these configurations. The solutions corresponding to unmountable linkages were automatically discarded by the optimization algorithm.

The value of $t1$ was imposed to guarantee easy accessibility to the patient at each orientation. Instead, $a1$ was considered as an independent variable, whose value was determined by assembly constraints. Indeed, the crank rotates approximately $275°$ during a complete motion of the table, thereby its length should be chosen carefully to avoid collisions with the adjacent motor housing. After performing few iterations, the size of $a1$ was chosen as the largest one compatible with the motor gearbox. As a matter of fact, the size of the DC motor assembly (which actuates the four bar linkages) and the link lengths are mutually dependent. For this reason, an iterative algorithm was developed to determine the final design (Fig. 4.23). In Fig. 4.23, the interconnections between link lengths, motor dimensions and motor force capabilities are highlighted. In Fig. 4.18, the link lengths of the optimized linkage are outlined.

In Fig. 4.20(a) the gravitational contributes to the resistive torque as a function of the crank angle are portrayed. Fig. 4.20(b) describes the magnitudes of the internal (F_1, F_2) and the external (R_1, R_3) forces interchanged between the links (included the ground frame). In these diagrams, forces and torques correspond to a single linkage[4]. The horizontal straight line in Fig. 4.20(a) represents the RMS value of the required torque. As it will be clarified in the following, we used those data to compute the cross sections of the links and to select the bearings.

Fig. 4.21(a) shows the assembled left linkage. Notice the metallic angular reinforcements fixed on the short sides of the wooden table, the particular shape of the connecting rod (required to avoid collisions with the driving shaft acting on the cranks) and the pair of angular elements fixed to link $t2$ in order to reduce the lever effect when the table stands in almost-horizontal configurations. Fig. 4.21(b) shows the aluminum element inserted in the wooden table to ensure a strong fastening between link $t1$ and the table.

---

[4] We hypothesized that the total load is always equally distributed between the two linkages.

4.5.1 Four bar linkage motor sizing & selection

4.5.1.1 Worm gearbox

To actuate the four bar linkages a worm gearbox and a brushed DC motor (CM040 and EC100.120 by TRANSTECNO) were selected. The installed non-back drivable gearbox is sufficiently strong to withstand the resistive torques required by the application. As already stated in the previous Section, the selection of this element was mainly based on assembly requirements (i.e., the necessity to have compatible sizes between link $a1$ and the worm gear). Also the rated torque at the output of the gearbox played a role in the process.

Since the resistive torque at the driving shaft (C_{rL}) varies as a function of the crank angle, two conditions were considered to estimate the torque requirements: the peak (MAX) and the (RMS) values of the torque during a full movement $0 \div 60°$ (Fig. 4.22). The sizing procedure is portrayed in Fig. 4.23, where the labels in the flowchart have the following meanings:

- STEP 1: definition of $a1$ (first guess) and first link length optimization;
- STEP 2: computation of the resistive torque C_{rL} (RMS and MAX);
- TEST: mechanical check (is the gearbox capable of withstanding the resistive torques?) and dimensional check (can the gearbox and the linkage be assembled together?)
- STEP 3: new definition of $a1$ and new link length optimization;

This procedure allows to identify the optimal geometry of the linkage and a class of gearboxes (having the same external dimensions) capable of withstanding the required resistive torques. The final mounting pose for the selected gearbox is the opposite of the one shown in Fig. 4.25. In this way, the distance between the output shaft and the lower surface of the table is minimized, and the compactness of the design of Sophia-3 is preserved. Additionally, by adopting this configuration, the worm gearbox is lubricated for the EOL (expected operating life). Fig.4.24 shows the maximum static and dynamic torques that can be applied to the output shaft of the gearbox. For the estimated rotational speed of the crank ($n_c = 5.7\ rpm$)

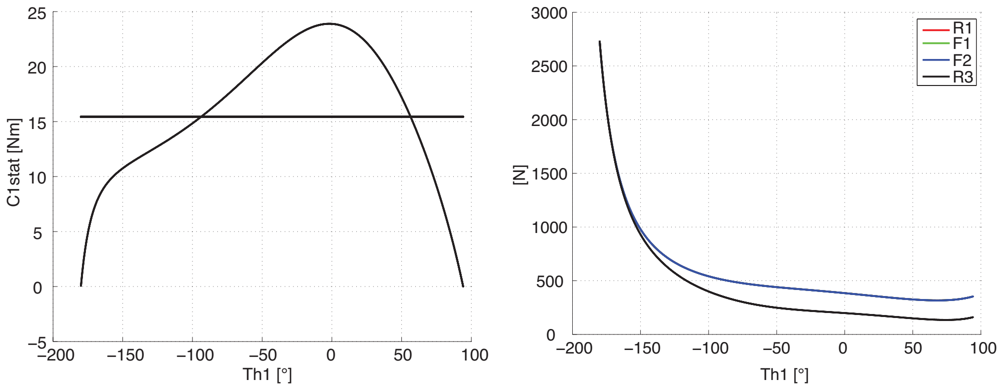

(a) (b)

Figure 4.20: Resistive gravitational torque (a) and magnitudes of the internal/external forces acting on the linkage (b) as a function of the crank angle.

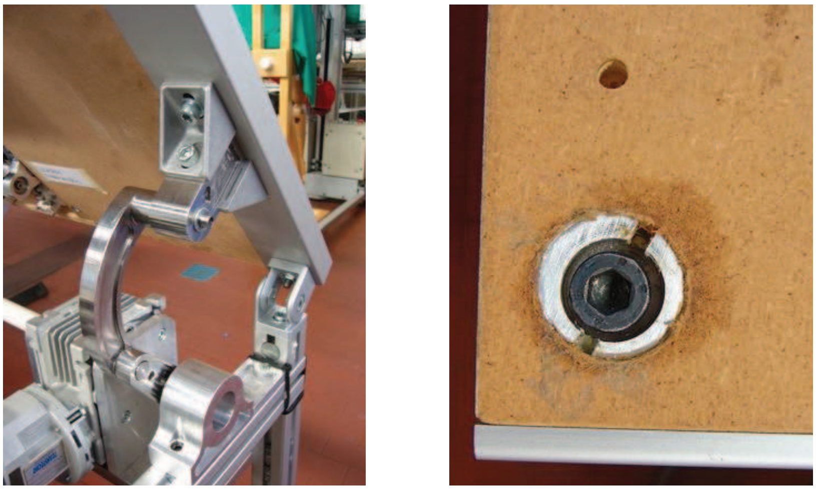

(a) (b)

Figure 4.21: Final design of the linkage (a) and metallic insert use to mount the $t1$ element on the wooden table (b).

it can be verified that the expected torques (Fig. 4.22) fall in the allowable range. As a further advantage, the selected family of gearboxes allows the insertion of a driving shaft whose diameter is sufficient to support the expected torsional stresses.

4.5.1.2 Brushed DC motor

The torques required to drive the worm gearbox are provided by a brushed DC motor (EC100.120). We decided to install motor and gearbox produced by the same manufacturer to eliminate the need for additional flanges. In this Section, the procedure followed in the selection of the motor is described. The choice of the most suitable family of worm gearboxes was determined based on assembly issues (Section 4.5.1.1). Now, a suitable reduction ratio for the worm gearbox and the size of the DC motor are to be selected. It turned out that

	$C_{rL,dyn}$ $[Nm]$	$C_{rL,grav}$ $[Nm]$	C_{rL} $[Nm]$
RMS	0.055	34.2	34.25
MAX	0.05	47.8	47.83

Figure 4.22: Estimated values for the resistive torque

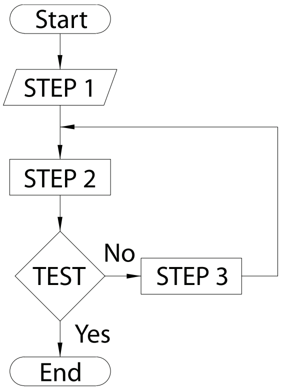

Figure 4.23: linkage/gearbox selection procedure

Speed [rpm]	3000	500	200	0
$c_{\max}$ [Nm]	$22 \div 32$	$35 \div 45$	$42 \div 70$	$85 \div 290$

Figure 4.24: Rated torques

Figure 4.25: CM 040 worm gearbox

the optimal reduction ratio was too large to be provided by a single gearbox. Therefore, an additional spur gearbox was inserted between the motor and the worm gearbox[5].

Given the function of this DOF, we initially decided to control the motor with a manual selector that applied $+12V/0V/-12V$ to the terminals of the windings by means of a H-bridge consisting of two relays (Fig. 4.43). Early tests showed that this solution introduced strong vibrations in the system, primarily due to the non-back drivability of the transmission and to the discontinuities in the input voltage. Hence, a custom-made drive was developed where a 16-bit microcontroller (dsPIC30F3011) provides trapezoidal profiles for the input voltage and manages the inputs from the manual selector and the limit switches located at the extremities of the travel. This open-loop control scheme proved to be suitable for manual positioning, where accuracy is not a concern.

The size of the DC motor was chosen by estimating the required drive torque in the most severe operating conditions[6]. From the Principle of virtual work we get:

$$C_m \delta\theta_m - J_m \ddot{\theta}_m \delta\theta_m - \frac{J_1}{\eta_1}\ddot{\theta}_1 \delta\theta_1 - \frac{J_2}{\eta_1\eta_2}\ddot{\theta}_2 \delta\theta_2 - \frac{C_{rL}}{\eta_1\eta_2}\delta\theta_2 = 0 \tag{4.2}$$

where C_m is the driving torque, C_{rL} is the resistive torque (Fig. 4.20(a)), $\delta\theta_m$, $\delta\theta_1$ and $\delta\theta_2$ are the virtual displacements of the motor shaft, of the spur gearbox output shaft and of the worm gearbox output shaft, respectively. Since all the reduction ratios are constant, (4.2) may be rewritten so as to isolate the crank angular acceleration $\ddot{\theta}_2$:

$$C_m = \left(J_m k_1 k_2 + \frac{k_2}{k_1}\frac{J_1}{\eta_1} + \frac{1}{k_1 k_2}\frac{J_2}{\eta_1\eta_2} \right)\ddot{\theta}_2 + \frac{1}{k_1 k_2}\frac{C_{rL}}{\eta_1\eta_2} \tag{4.3}$$

Where k_1 and k_2 are the reduction ratios of the spur gearbox and of the worm gearbox, respectively. By applying (4.3), the maximum required driving torque was computed for different choices of the gearbox unit. Fig. 4.26 and Fig. 4.28 illustrate the main characteristics of the selected components. In Fig. 4.28, k_t is the motor torque constant, R is the winding resistance and V is the nominal input tension. M_n and I_n are the rated torque and the rated winding current, respectively.

---

[5] Being located coaxially to the DC motor, the auxiliary gearbox did not introduce assembly issues.

[6] Friction torques were not considered directly in these computations, instead, efficiency coefficients were adopted as suggested by the manufacturers. Also, to compensate for unmodeled loads, we imposed a fictitious precautionary operating condition wherein the maximum estimated speed and the maximum estimated resistive load are reached at the same instant.

$k = k_1 \cdot k_2$	η_{stat}	η_{dyn}
300	0.24	0.403

Figure 4.26: Specifications of the combined reducer ($\eta = \eta_1\ \eta_2$)

Figure 4.27: Assembled gearmotor unit

J_m	M_n	k_t	R	V	I_n
$[g\,cm^2]$	$[Nm]$	$[Nm/A]$	$[\Omega]$	$[V]$	$[A]$
2700	0.43	0.035	0.096	12	16.8

Figure 4.28: Specifications of the EC100.120 brushed DC motor

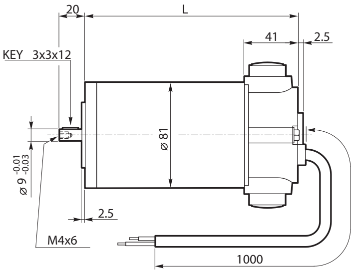

It is expected that the orientation of the table will be modified once per therapeutic exercise. Therefore, the usage frequency of the motor will be quite low, and each operation will last few seconds. Under these assumptions, selecting the motor size based on the rated torque would be too conservative, since the possibility to reach the winding thermal limits ($T \approx 155°C$) is remote. Conversely, the major limitations are due to electromagnetic issues. By incrementing the winding current, the intensity of the generated electromagnetic field is increased proportionally. This intensity must be limited to prevent demagnetization of the permanent magnets mounted on the stator. This, in turn, places a limit to the maximum torque available for short time intervals: $M_{demagn} \approx (3 \div 4)\ M_n$.

To compute the worse-case operating loads, we assume that the maximum estimated resistive torque C_{rL} and the maximum estimated speed are reached at the same instant[7]. Friction forces in the gearboxes have been taken into account by introducing suitable efficiency coefficients η_1 and η_2[8]. The static value in Fig. 4.26 (i.e., the one corresponding to the starting conditions) has been considered in the calculations. Indeed, when operating the linkage the initial and final positions of the table may assume any value inside the interval $0 \div 60°$. Thus, in the worst case, the table starts moving upward from the configuration corresponding to the maximum resistive torque (Fig. 4.22).

The computed data are shown in Fig. 4.29. $C_{m,\max,req}$ is the maximum resistive torque as seen from the motor shaft, n_{mot} is the maximum rotational speed of the motor shaft, $C_{m,avail}$ is the peak torque of the motor and M_{demagn} is the torque limit due to demagnetization effects. Since $M_{demagn} > C_{m,\max,req}$, the selected gearmotor is suitable for our application.

Finally, the electric loads corresponding to the worse-case operating condition have been estimated (Fig. 4.30). $P_{el,\max}$ and $P_{el,\mathrm{RMS}}$ are the peak value and the square mean root of the electric power required to complete a full movement ($0 \div 60°$). These data have been

---

[7] This condition corresponds to $\theta_{table} \approx 35°$ and $n_{crank} \approx 5.7\ rpm$.

[8] From a technical point of view this choice is questionable, since efficiency coefficients are defined for steady-state conditions. However, the followed approach is the one suggested by the manufacturer for dimensioning purposes.

n_{mot}	$C_{m,\max,req}$	$C_{m,avail}$	M_{demagn}
$[rpm]$	$[Nm]$	$[Nm]$	$[Nm]$
1718.7	0.689	2.163	0.99

Figure 4.29: Mechanical data @ the reference working point

$I_{a,\mathrm{RMS}}$	$I_{a,\max}$	$P_{el,\mathrm{RMS}}$	$P_{el,\max}$
$[A]$	$[A]$	$[W]$	$[W]$
12.96	19.69	155.5	236.2

Figure 4.30: Electrical data @ the reference working point

used in the selection of the power supply (Section 4.8.2). It can be noticed that the estimated peak current is rather large. This value would have been greatly increased without the spur gearbox, thus implying more expensive power supplies.

4.5.2 Static verification/fatigue analysis

All the custom-made components have been statically verified through FEM analysis. Fatigue verifications have been carried out on critical elements (e.g., the driving shaft, the links of the four bar linkage, the pins, etc) according to the UNI 7670 standards. Specifically, for the fatigue verifications, the reference load history has been assumed as a sequence of full upward and downward movements of the table. The forces/torques acting on each link are those estimated in the previous sections. As an example, Fig. 4.31(a) show the estimated equivalent stress in the critic point of the crank, as a function of the crank angle. The stress/strain diagram of the crank corresponding to the configuration Ain Fig. 4.31(a) is depicted in Fig. 4.31(b).

4.5.3 Rolling bearings selection

In the following, a brief description of the installed bearings will be given. Since all the involved rotational speeds are low (e.g., $n_c \approx 5.7\ rpm$ in the maximum estimated speed of the crank), and since the table will be kept in a fixed position for most of the EOL, the static load coefficient C_0 was utilized in the calculations.

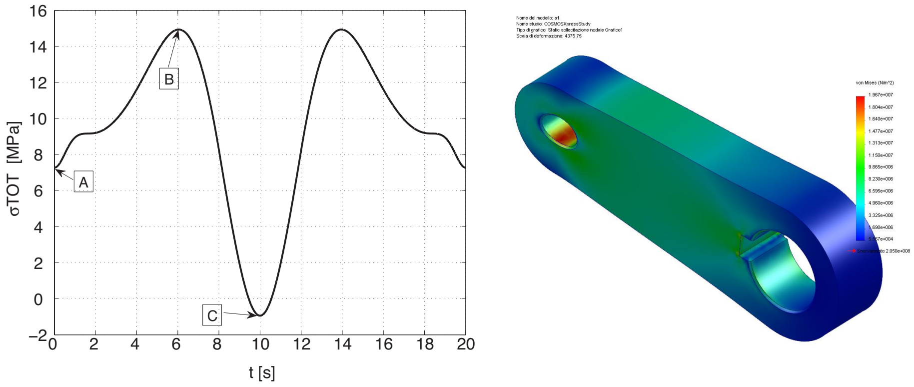

(a) (b)

Figure 4.31: σ_{EQ} in the critical point of the crank, as a function of the crank angle (a). Stress/strain diagram (as derived from static FEM analysis) corresponding to configuration A (b).

	R_A	R_B	R_C
	$[N]$	$[N]$	$[N]$
Left	1830.2	903.8	1186.2
Right	62	2672	81.3

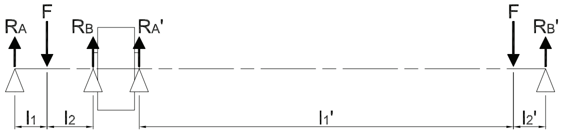

Figure 4.32: Estimated radial loads on the driving shaft

The two rolling bearings that supports the driving shaft are fundamental for the functionality of the four-bar linkage. Their housings are located at the two extremities of the shaft that oppose the gearbox. Looking at the forces illustrated in Fig. 4.32, we selected two 61904, whose static coefficient is $C_0 = 3650N$.

For the four-bar linkage, a set of needle rolling bearings was selected to reduce friction torques when links rotates w.r.t. the adjacent ones. Fig. 4.33 illustrates the top view of the right linkage: notice the housings designed for the three rolling bearings. Since the available space for the housings is quite reduced, needle bearings without the inner ring were preferred to standard ball bearings. These models are characterized by reduced radial encumbrance and high load capabilities, and must be forced inside the housing. The selected model (HK0810) has $C_0 = 4050\ N$ and should withstand a maximum radial load of $2734\ N$.

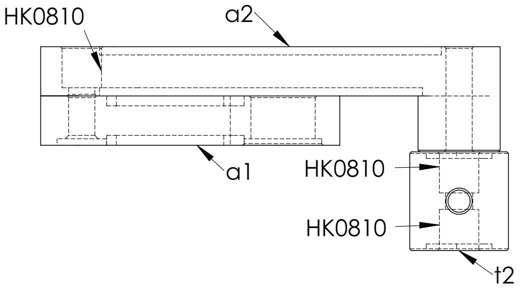

Figure 4.33: Locations of the bearings installed in the linkage *cambiare*

4.6 End-effector

The end-effector of Sophia-3 consists of a joystick that is grasped by the patient during the therapy. Four main aspects were taken into account in the design of this device:

- reduction of friction forces to improve haptic transparency.
- possibility to choose different grips according to the patient's specific needs.
- minimization of the overall dimensions, so as to reduce the unreachable regions of the workspace.
- ease of replacing the grip.

The final design is composed of a cross-like aluminum base and a interchangeable grip. The former can slide over the table on four small PTFE disks (one for each leg) aimed to reduce

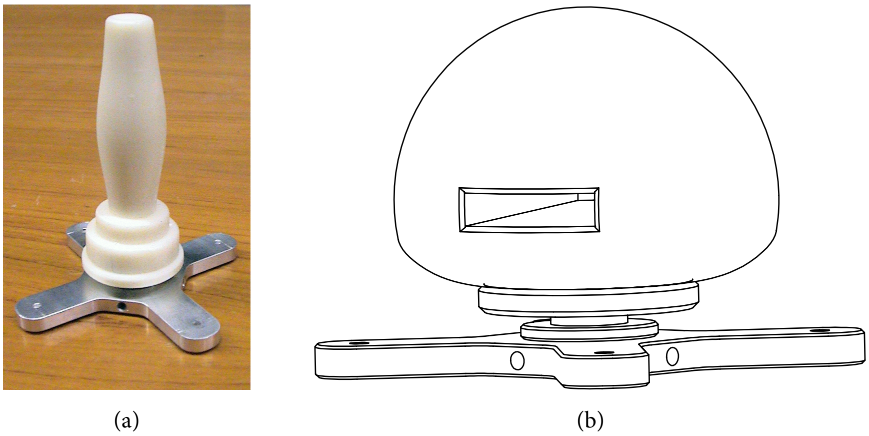
(a) (b)

Figure 4.34: Current end-effector and CAD rendering of the alternative design for the handle.

friction. The grip assembly is composed of a shaft, the grip itself and a cover used to constrain the axial movements of a ball bearing. The quick fastening device consists of four rolling-ball tip set screws that are fastened on the base element and act on a circumferential slot made on the shaft. The outer ring of the bearing (61900) is forced on the housing and its axial movements are prevented by a cover. Both the cover and the grips were realized in *ABSplus* by means of a fast prototyping device (3D printer). The wires are connected to the shaft by means of simple eyelets. The selected wire (made of *Dyneema* fiber) is quite thin ($d_0 \approx 0.6mm$) and can handle large loads (up to $25kgf$ in static conditions). Impulsive forces are also well tolerated. Two grip assemblies were designed (Fig. 4.34). The hemispherical geometry of the grip in Fig. 4.34(b) aims to settle the hands of those patients who find it difficult to use the vertical grip. The rectangular slot inside the grip should be used to arrange a *Velcro* strip, useful to fasten the patient's hand.

4.6.1 Rolling bearing selection

Given the small loads acting on the joystick, the static verifications of the parts is not required. To select a suitable rolling bearing, an axial and radial loads are assumed as $F_r = 205N$ and $F_a = 80N$, respectively. The equivalent static load is defined as:

$$P_0 = X_0 F_r + Y_0 F_a$$

Therefore, for $X_0 = 0.6$ and $Y_0 = 0.5$, we get $P_0 = 205N$. With a safety coefficient of 1.5, the required C_0 is $307.5N$. The 61900 deep groove bearing has $C_0 = 850N$ and is therefore suitable for this application.

4.6.2 Spring selection

In the first version of the prototype, the upper motors were controlled in torque mode, whereas the moving-pulley motor was controlled in position mode. This solution was adopted because of the high friction torque generated by the lower worm gearbox, which

De [mm]	d [mm]	L_0 [mm]	L_1 [mm]	P1 [N]
7	1.4	22.1	26.46	114

Table 4.3: Specifications of the T31920 model. De= external diameter, d= wire diameter, L_0= no-load length, L_1= length @ $P1$, $P1$ = max load

prevent the lower motor from being controlled in torque mode with an open loop (i.e., by monitoring the winding currents).

Therefore, an elasticity had to be introduced in the lower cable. Indeed, if the elastic behavior of the cable is known, and the position of the end-effector in known as well, then the desired tension in the lower cable may be obtained by imposing a certain position to the motor shaft.

The initial hypothesis to use the distributed elasticity of the cable was discarded, since usually this quantity is not specified in data sheets. Additionally, experimental tests showed that the selected polymeric cable (*Dyneema* fiber) has a clear viscoelastic behavior, which is difficult to model. Conversely, using high-stiffness metallic wires would have lead to a poor resolution in the force command.

Thus, a lumped stiffness was introduced by installing a linear spring in series to the lower cable, to be connected between the end-effector and the cable. Choosing the most suitable stiffness value implied a compromise between force resolution/accuracy and workspace area. Indeed, the lower the stiffness, the higher the elongation for a given tension, and therefore, the higher the resolution. On the other hand, the spring cannot be reeled on the lower pulley, that is, the vertical size of the workspace must be reduced by subtracting the spring length.

To select a suitable spring, we imposed a maximum length $l_{\max} = 30mm$, and a maximum load $f_{\max} = 120N$. The specifications of the model chosen (METERSPRINGS T31920) are outlined in Tab. 4.3. The elongation @ $P1$ is: $\Delta l = L_1 - L_0 = 4.36mm$, which corresponds to the following pulley rotation (pulley radius is $ra = 23mm$):

$$\theta_p = \frac{\Delta l}{ra} = 0.1896\ [rad] \tag{4.4}$$

and in terms of encoder pulses:

$$n_p = \theta_p\, \frac{4 \cdot 2048\ k_{red}}{2\pi} \approx 1730\ [pulses] \tag{4.5}$$

Thus, the resolution on the commanded torque is:

$$R = \frac{P1}{1730} = 0.07 \left[\frac{N}{pulse}\right] \tag{4.6}$$

this value, however, does not take into account the position accuracy of the device[9].

---

[9] First experimental tests showed that this design choice is not effective. Indeed, we realized that the position accuracy is $\approx 2mm$ throughout the workspace. This low accuracy made it impossible to control the tension in the lower cable through the aforementioned procedure. For this reason, we came back to the first design hypothesis, commanding all the motors in torque mode. This choice, in turn, implied the partial redesign of the lower pulley-block (Section 4.4.2).

APM	Rated/Max Torque [Nm]	Rated/Max RPM	Incr. Encoder [P/R]	Braking Type	$I_{q,\max}$ [A]
SC05D	2.15/6.44	2000/3000	2500	Spring	12.93
SA01A	0.318/0.955	3000/5000	2048	Spring	5.34
SB02A	0.637/1.912	3000/5000	2500	Spring	6.36

Table 4.4: Main characteristics of the installed brushless motors

4.7 Drive selection

Drives were selected based on the maximum winding currents estimated for each motor. Specifically, each drive is capable of providing continously the peak currents that characterize the corresponding motor. Once the torque constant K_t is known, the quadrature current I_q required for a given torque M can be computed as:

$$I_q = \sqrt{2} \cdot \frac{M}{K_t} \tag{4.7}$$

Tab. 4.4 sums up the main characteristics of the installed motors and shows the peak values of the quadrature currents. The installed drives belongs to the Cello series developed by ELMO Motion Control. Three Cello 15/60 were adopted for the fixed and the moving pulley-blocks, whereas a Cello 5/60 serves the screw servomotor. The main features of these drives are outlined in Fig. 4.35. $U_{\min}$, U_n and $U_{\max}$ are the minimum, rated and peak values for the input voltage, P_{max} is the maximum output power, η is the rated efficiency and I_n and $I_{\max}$ are the rated and the peak values of the output currents. All the drives are compatible with the CANopen communication standard. This protocol was employed to develop the first control architecture of Sophia-3.

Model	$U_{min}/U_n/U_{max}$	P_{max}	η	I_n/I_{max}
	$[V]$	$[W]$	$[1]$	$[A]$
CEL 15/60	10/50/59	720	0.97	15/30
CEL 5/60	10/50/59	240	0.97	5/10

Figure 4.35: Main characteristics of the Cello Drive

Figure 4.36: Cello digital servo drive and I/O ports

Motore	M_n	P_n	K_t	K_e	R	L	p
	$[N \cdot m]$	$[W]$	$[\frac{N \cdot m}{A}]$	$[\frac{V \cdot s}{rad}]$	$[\Omega]$	$[mH]$	$[1]$
SC05D	2.15	450	0.6908	0.4135	1.986	13.426	4
SB02A	0.637	200	0.1300	0.0773	0.4	1.316	4
SA01A	0.318	100	0.1397	0.0773	2.556	2.132	4

Table 4.5: Electrical specifications of the BPM motors

4.8 Power supplies selection

4.8.1 Power supplies for the BPM motors

Two major aspects were considered in the choice of the power supplies: the power that must be provided to the corresponding drive(s) and the nominal input voltage of the drive. All the installed drives should be supplied with an input voltage of $50\ V$, even though a wider range may also be acceptable ($10 \leq U_{in} \leq 59\ V$). Additionally, in order not to activate the under-voltage and the over-voltage protections, the input power required by the drive (and, in particular, the peak power $P_{\max}$) should be provided without significant voltage drops (i.e., $\leqslant 10\%\ U_{in}$). Keeping in mind the aforementioned constraints, the power required by each motor during a reference motion is first computed, and then the value is increased by the inverse of the drive efficiency in order to get an estimate of the required power. The latter is finally used to select a suitable size for the power supply. Even though this method may lead to overestimate the required power, we kept this additional *safety margin* to exploit the peak performances of the servomotors. Tab. 4.5 shows the mechanoelectrical characteristics of the installed BPM motors: K_e is the BEMF constant, R and L are the phase-to-phase values of the resistance and of the inductance and p is the number of pole pairs. The following equation yields the power drawn by a synchronous motor:

$$P_{dr} = \frac{3}{2}(U_d \cdot I_d + U_q \cdot I_q) \tag{4.8}$$

If the rotor is isotropic, the following equations hold (where R ed L are now the values pertaining a single winding):

$$M = \frac{3}{2}\,(p\,\Lambda_{mg}\,I_q) = \sqrt{2}\,K_t\,I_q \tag{4.9}$$

$$\begin{cases} U_d = R \cdot I_d - \Omega_{me} \cdot L \cdot I_q \\ U_q = R \cdot I_q + \Omega_{me} \cdot L \cdot I_d + \Omega_{me} \cdot \Lambda_{mg} \end{cases} \tag{4.10}$$

The mechanoelectrical speed Ω_{me} is obtained from the actual speed through the following expression: $\Omega_{me} = p\ \Omega_m$. The magnetic flux can be computed as: $\Lambda_{mg} = \sqrt{\frac{2}{3}} \cdot \frac{K_e}{p}$. As it can be inferred from Tab. 4.5, the following correlation holds: $K_t = \sqrt{3} \cdot K_e$. For the sake of simplicity, in the following calculations the drive is supposed to keep the motor in the conditions of *maximum torque-current ratio* (i.e., $I_d \approx 0$).

Among several operating conditions that were tested, the most severe ones were identified as the following:

APM	I_q	U_q	P_{dr}	P_{req}
	$[A]$	$[V]$	$[W]$	$[W]$
SC05D	4.40	7.91	52.21	53.83
SB02A	1.96	1.03	3.03	3.13
SA01A	3.22	9.12	44.05	45.41

Table 4.6: Estimated electrical loads in the BPM motors

model	P_{out}	U	I_{out}
	$[W]$	$[V]$	$[A]$
SP-200-48	201.6	48	4.2

Figure 4.37: Meanwell power supply specifications

- Fixed pulley-block: $M = M_n$, $n = 415\ rpm$;
- Moving pulley-block: $M = M_n$, $n = 2905\ rpm$;
- Screw: $M = 0.18\ Nm$, $n = 400\ rpm$;

$n = 415\ rpm$ corresponds to the reference linear speed $\dot{x} = 1ms^{-1}$ of the cable when the pulley ($r_p = 23mm$) is directly keyed on the motor shaft. $n = 2905\ rpm$ is the corresponding value when considering the insertion of a speed reducer ($k_{red} = 7$)[10]. For the screw servomotor, less stringent conditions were assumed in order not to oversize the power supply. The power drawn by each servomotor (P_{dr}) in the reference conditions was computed with (4.9), (4.10) and (4.8). The result is finally increased by the inverse of the drive efficiency η to get P_{req}. The results are reported in Tab. 4.6. Each fixed pulley-block is supplied by a separate unit, whereas the screw servomotor and the moving pulley-block are supplied by the same unit. Three identical power supplies were installed (MEANWELL SP-200-48). The specifications illustrated in Tab. 4.37 refer to the rated values. A peak value $P_{max} = (1.05 \div 1.5)\, P_{out}$ may also be supplied for limited time intervals.

4.8.2 Power supply for the brushed DC motor

Fig. 4.38(a) illustrates the winding current required to provide the driving torque for a full movement of the table. Assuming that the motor is to be supplied with a constant input tension $U_{in} = 12V$, the maximum required power is $P_{\max} = 252\ W$. The specifications of the selected power supply are illustrated in Fig. 4.39. As it can be easily inferred, the power supply is capable of exploiting the peak performances of the DC motor. Similarly to the other

---

[10] As explained in Section 4.4.2, this reducer was lately removed.

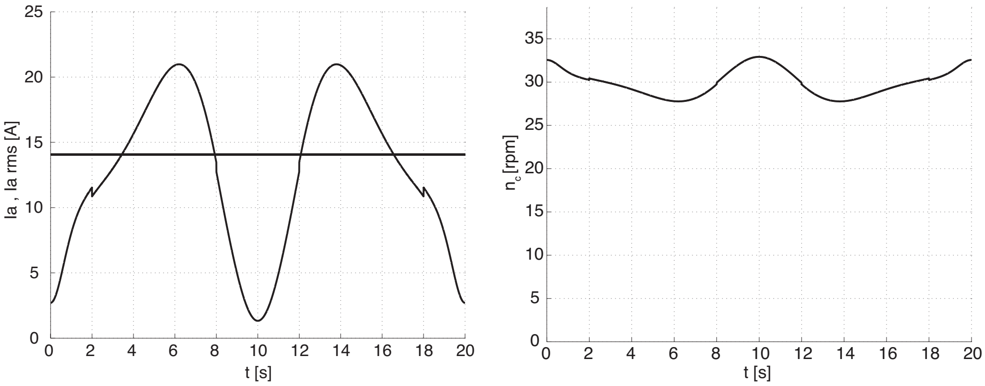

(a) (b)

Figure 4.38: Winding current (b) and crank speed (b) corresponding to the movement

models, it is possible to get $P_{\max} = 1.5\ P_{out} = 480\ W$ for limited time intervals. The corresponding peak current $I_{\max} = 40\ A$ is close to the demagnetization limit of the motor.

In Fig. 4.38(b) the crank speed for a full table movement to be concluded in $t = 10\ s$ is represented. These values have been estimated for a constant input voltage $U_{in} = 12V$. Even though the movement does not represent all the operating conditions, if was used to give insight into the velocity profile generated by applying a constant tension. As it can be noticed, the speed variation is moderate.

All the power supplies are equipped with *Power Factor Correction* (PFC). This control criterion allows to reach efficiency values (power factors) close to unity and reduces the mutual influence of the supplied devices.

4.9 Electric scheme

In the following, the main characteristics of the electric scheme designed for Sophia-3 are briefly outlined. There are three different supply voltages:

- **12V** (from SP-320-12, Fig. 4.39): serves the custom-made drive of the brushed DC motor (Section 4.10).
- **24V** (from SP-150-24, Fig. 4.40): serves the controller, the cooling fans, the brakes and the safety circuit.
- **48V** (from three SP-200-48, Fig. 4.37): serve all the CEL drives.

model	P_{out}	U	I_{out}
	$[W]$	$[V]$	$[A]$
SP-320-12	320	12	25

Figure 4.39: Meanwell power supply specifications

model	P_{out}	U	I_{out}
	$[W]$	$[V]$	$[A]$
SP-150-24	150	24	6.3

Figure 4.40: Meanwell power supply specifications

A master switch controls the mains of the electric panel. After turning the switch on, the controller and the drives are immediately turned on, however, the device remains in the *emergency* status until the start button is pressed. The *emergency* and the *ready* states are indicated by a red and a blue lamp, respectively. Once the start button has been pushed, the relays K1 and K2 are energized. Also, a NO contact of K1 gives self-supply to the safety circuit.

Unlike what is illustrated in the simplified scheme (Fig. 4.43), breaks are not directly fed by the safety circuit. Instead, each drive unblocks the corresponding brake through a dedicated digital output. Both the drives and the controller are capable of detecting the status of the device through digital inputs that are directly connected to contacts of the K1 relay. The input plug is equipped with a *line filter* to reduce the harmonics in the input/output currents. A magneto thermal switch was installed to protect against short-circuit and non short-term overloads. Additionally, all the components are protected by fuses.

The cabinet has been integrated inside the main frame, between the right legs of the table (Fig. 4.41). The power supplies and the controller are located inside the cabinet, whereas the drives are fastened to metallic insets located on the bottom surface of the table. Power and feedback wires reach the bottom surface of the table via a plastic cable carrier (KABELSCHLEPP TYPE 0180) and are conveyed inside a cable tray from which they reach

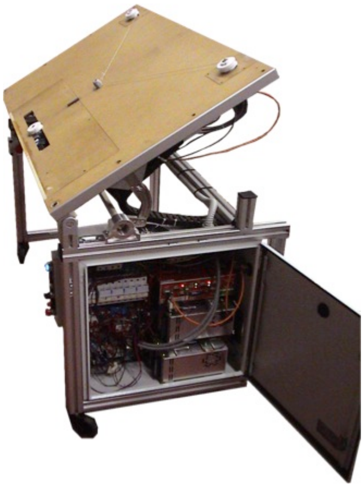

Figure 4.41: Sophia 3: electric cabinet

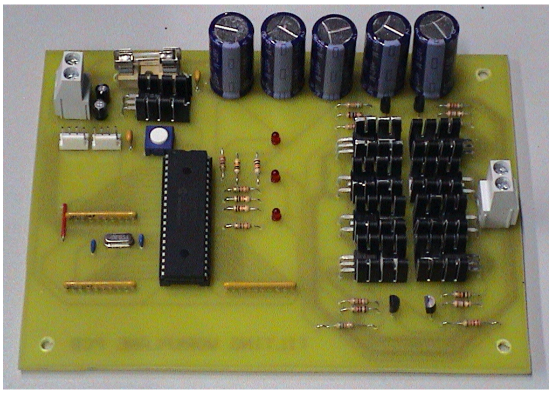

Figure 4.42: Brushed DC motor drive

the corresponding drives or PCBs.

The cooling of the cabinet is provided by two fans, one introducing fresh air and the other one drawing air out of the case. Moreover, all the drives except the smallest one are equipped with embedded cooling fans. The size of the fans was selected by first estimating the required air flow rate ([97]):

$$Q = \alpha \cdot \left(\frac{P_d}{T_i - T_e} - K \cdot S_r \right) \tag{4.11}$$

where Q is the required flow rate ($[m^3\ h^{-1}]$), P_d ($[W]$) is the overall power dissipated by the devices located inside the cabinet, T_i and T_e ($[{}^\circ C]$) are the average internal and external tempertures, respectively. K is the thermal conductivity of the cabinet ($[W\,K^{-1} m^{-1}]$), $\alpha = 4.4$ is an empirical coefficient and S_r ($[m^2]$) is the useful conductive surface. The selected cooling fans (NMB-MAT 4710KL) are capable of providing the estimated air flow ($Q \approx 200\ m^3\ h^{-1}$).

4.9.1 Safety devices

In accordance with the *CEI EN 60601-1* standard on Electromedical devices, Sophia-3 is equipped with a safety circuit that cuts the power supplied to the motors in case of fault. The safety circuit is guarded by a safety relay. By pushing one of the emergency buttons (or, equivalently, by using a dedicated digital output in the controller), the drives switch to the inhibit status and the brakes are activated. To this end, two relays (named K1 and K2 in Fig. 4.43) have been installed. Therefore, the following devices are capable of switching the machine to the *emergency* status:

- the stop button;
- the emergency buttons;
- the watchdog of the controller;
- a dedicated output of the controller
- the two limit switches of the linear guide;

Thus, the run status can be achieved only once all the previous contacts have been closed, i.e., after the controller has terminated the startup procedure and no emergency buttons have been pushed.

4.10 Operating the Brushed DC motor

As it was mentioned in Section 4.5.1.2, the four bar linkage was initially operated by applying a constant input tension $U_{in} = 12V$ by means of a manual selector. The selector also controlled the direction of motion by alternatively energizing two relays (K3 and K4 in Fig. 4.44) disposed so as to form a H-bridge. Additionally, two limit switches prevent the motor from further moving once one dead point (i.e., 0° or 60°) was reached.

After having assembled the prototype, first experimental tests showed that this kind of control was unsuitable, since it caused large vibrations at the start and at the end of each movement. This was mainly due to the *non-backdrivability* of the orthogonal gearbox. To

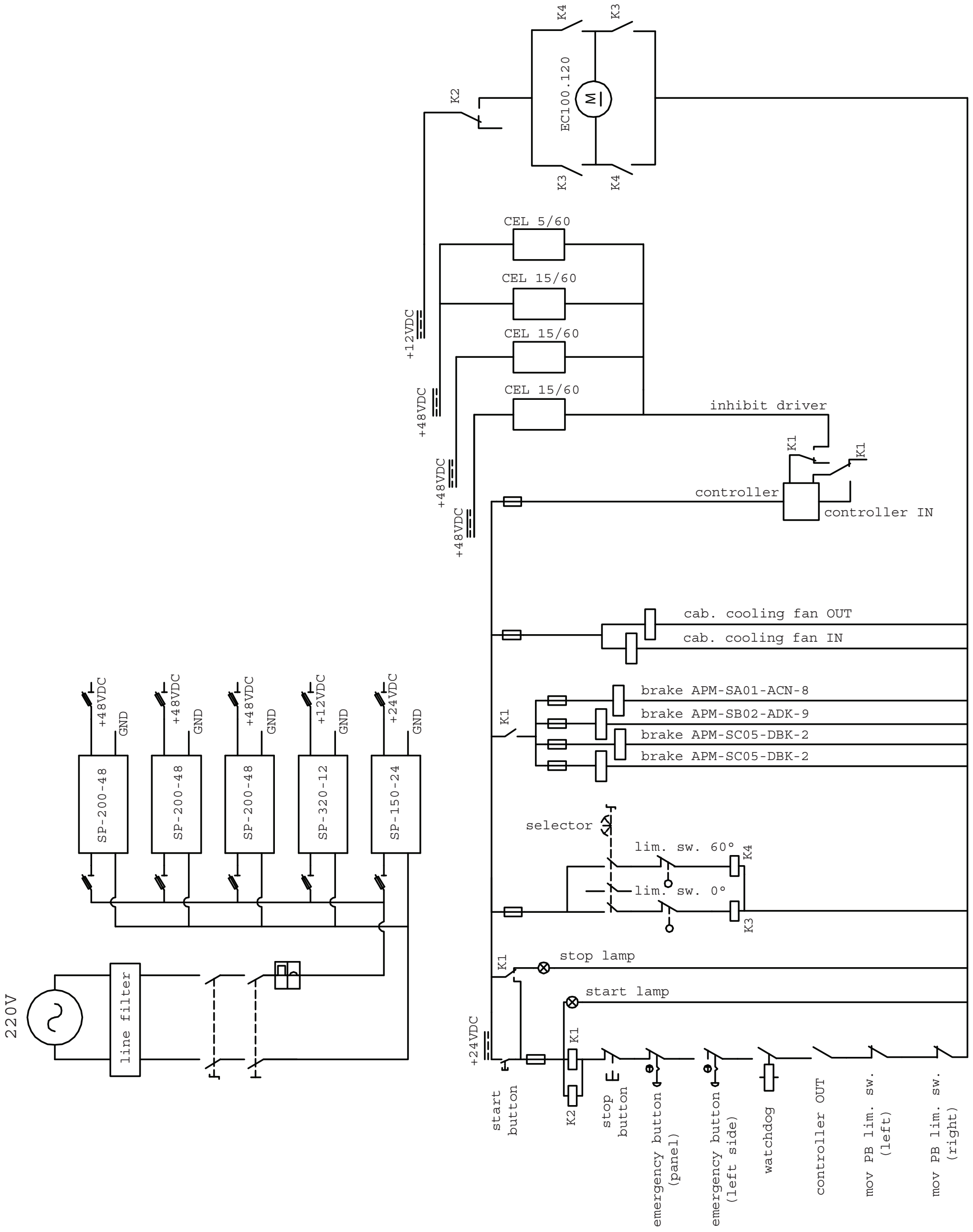

Figure 4.43: Simplified electric scheme of the Sophia-3 prototype

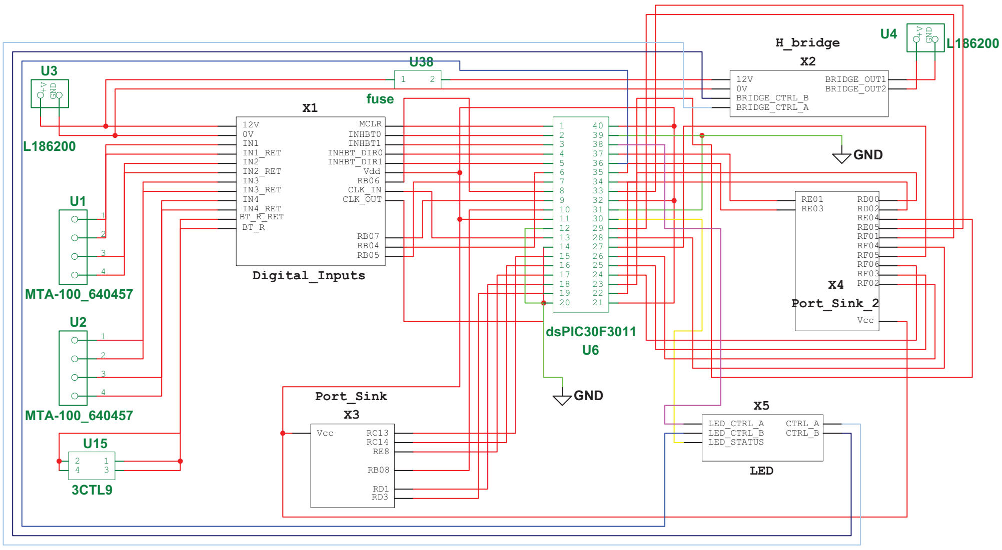

Figure 4.44: Brushed DC motor drive, PCB scheme

reduce this effect, a custom-made drive was designed that supplies a trapezoidal profile for the input tension at each movement (the acceleration/deceleration time intervals are set to $T_a = T_d = 1024ms$). In the new hardware, the H-bridge consists of four power MOSFETs which are controlled by a 16-bit microcontroller (dsPIC30F3011) via 4 bipolar junction transistors (BJTs, Fig. 4.42). The dsPIC also manages the digital input signals from the manual selector and the limit switches (i.e., the input and inhibit commands, respectively).

All the components are mounted on a PCB (Fig. 4.42). The input voltage is provided to the board through the power input terminals (L186200, label U3 in Fig. fig:schematot) and the output tension to the motor is supplied through similar terminals located on the opposite side of the board (label U4). A fuse ($I_n = 25A$, label U38) protects the device from potential overloads and a set of 5 capacitors arranged in parallel ($C_{tot} = 13.5\mu F$, labels U19-U23 and U37 in Fig. 4.45) is interposed between the power source and the H-bridge. They work as a over-voltage *snubber*, which is required (due to the inductance of the wiring) during sudden changes of the input current.

The nominal current for the EC100.120 DC motor is $I_n = 16.8A$, and the nominal voltage is $U_n = 12V$ (Fig. 4.28). Obviously, the microcontroller cannot manage those power signals directly. Indeed, its digital outputs (here used as PWM peripherals) are capable of supplying $i_{\max} = 25mA$ @ $5V$. Therefore, each of the switches of the H-bridge consists of a power MOSFET in parallel with a diode. The switches are arranged in a symmetric fashion (i.e., the upper legs are identical, and the lower legs are identical). The main current flows from an upper leg to the lower leg located in the opposite side. Therefore, these switches are controlled by the same output from the microcontroller (ctrl_A or ctrl_B in Fig. 4.45). The function of the diodes (FFPF30U60STU, labels U24-U27 in Fig. 4.45) is to protect the corresponding MOSFET from tension peaks generated by the motor.

Each of the upper switches is equipped with a MOSFET-p (STP80PF55, labels U16 and U17), which can withstand drain currents up to $I_{\max} = 80A$. When a negative potential

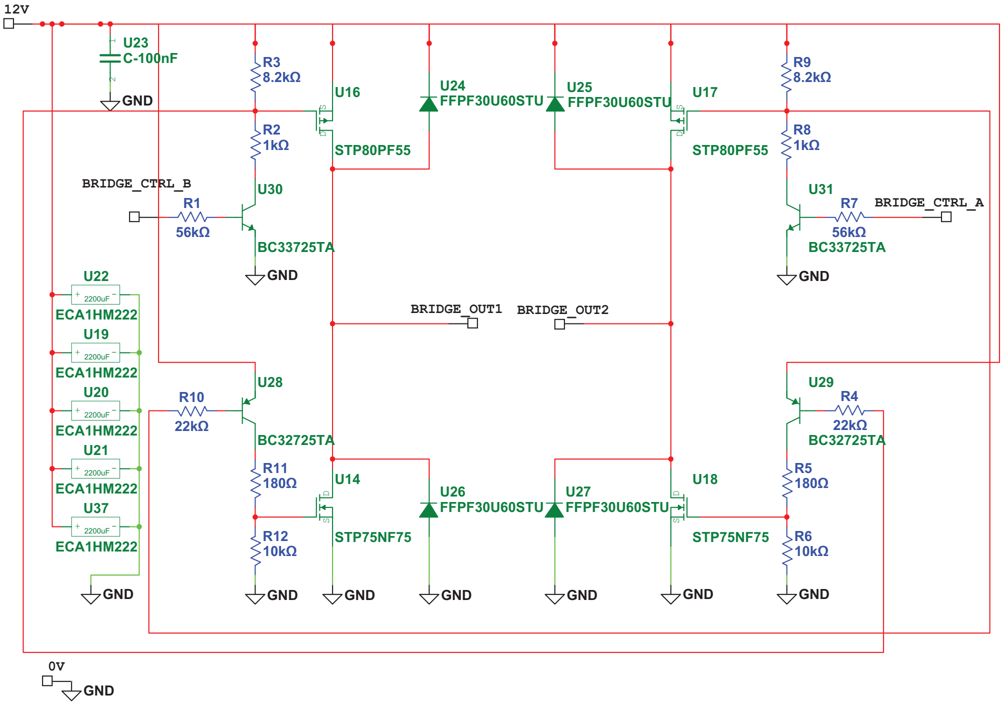

Figure 4.45: The H-bridge subsystem

difference $V_{GS} \le -3V$ is applied between the gate and the source, the MOSFET lets the current flow between the source and the drain. When V_{GS} is close to the nominal value $-10V$, the device acts as a closed ideal switch (i.e., negligible voltage drop). Conversely, when $V_{GS} \approx 0V$, no current flows between the source and the drain, and the MOSFET acts as an open contact. Each of the lower switches is equipped with a MOSFET-n (STP75NF75, labels U14 and U18) whose behavior is the opposite of the p-type (i.e., the MOSFET lets the current flow between the drain and the source when a positive potential $V_{GS} \ge 3V$ is applied, and it approximates an ideal closed contact for $V_{GS} \approx +10V$). Thus, the MOSFETs can be though of as switches that are controlled by the potential difference V_{GS}.

The voltage drops required by the MOSFETs are provided by the BJTs, which, in turn, are controlled by the digital outputs of the dsPIC. Specifically, the upper switches comprise a npn-type transistor (U30 and U31) and the lower switches comprise a pnp-type transistor (U28 and U29). Transistors can be though of as switches that are controlled by the base current i_B. In the upper legs, npn-type BJTs (BC33725TA) are installed. When the corresponding digital output is down, the base and the emitter are at the same potential, and the device acts as an open switch. Conversely, when a certain positive tension is applied between the base and the emitter, the collector current i_C flowing between the collector and the emitter is proportional to the base current i_B, the correlation being expressed by the coefficient $h_{FE} \approx 100$ (i.e., $i_C = h_{FE}\ i_B$). The same concept applies to the pnp-type BJTs installed in the lower legs (BC33725TA), except that the tension difference between the base and the emitter must be negative (and, therefore, i_B is directed outward the base). When the corresponding digital output (say, ctrl_B) is activated, current flows through R3 and R6 (Fig. 4.45), thus providing

	brake	inhibit	prox. sens.	potentiometer
left fixed PB drive	*	*		
right fixed PB drive	*	*		
moving PB drive	*	*		
screw motor drive	*	*	*	*

Table 4.7: Functionalities of the I/O PCBs

the required voltage drops to activate the MOSFETs U16 and U18. The resistors have been dimensioned to guarantee the suitable currents and the suitable voltage drops.

The control logic implemented on the dsPIC is discussed in Section 5.5. There are 4 digital inputs arriving at the dsPIC. The input port U1 receives the signals from the limit switches, while the input port U2 receives the signals from the selector (Fig. 4.44). All the signals work in negative logic. The clock signal to the microcontroller is provided by a crystal oscillator (HC49SLF). A voltage regulator (LM1085IT5) converts the $12V$ from the power supply to the $5V$ required by the microcontroller (Vcc) and by the digital inputs. In the case of fault, the device can be reset through a microswitch (3CTL9).

4.11 I/O drive

The custom-made PCBs that manage the I/O of the drives are fundamental to guarantee the functionality of the control. Indeed, those elements let the drives control the brakes, let the controller handle the *emergency* status and let the signals from various sensors be acquired.

The Cello servodrive is a digital motion controller that supports the CANopen protocol. This functionality was exploited for data interchanging between the controller (Robox μ-RMC) and the drives. Controlling a motor can be achieved through position, velocity or current loops. Fig. 4.36 shows the drive and its I/O ports, named J1 and J2. The former is capable of handling 6 digital inputs and 5 digital outputs. The latter is an input port that can manage 4 digital inputs and 2 analog inputs. The following devices/functions are controlled through the I/O ports of the drives:

- **Brake** 4.11.1. To improve safety, the brakes must necessarily be unblocked by the drives. That is, even though the machine is in the *ready* status, brakes should not be energized until all the motors are enabled and no troubles are detected by the controller. Conversely, when the status switches to *emergency*, brakes should be de-energized immediately.
- **Motor inhibit/enable** 4.11.2. The drives themselves should be inhibited, unless the machine is in the *ready* status. Pushing the stop button or one of the emergency buttons should cause the drives to switch to the inhibit status.
- **Inductive proximity switches** 4.11.3. The linear motion of the lower pulley-block is controlled in position mode by the screw servomotor. Since this motor is equipped with an incremental encoder, a homing procedure must be performed at each startup. Therefore, inductive proximity switches have been installed (SI5-C0.8 NPN NO) near

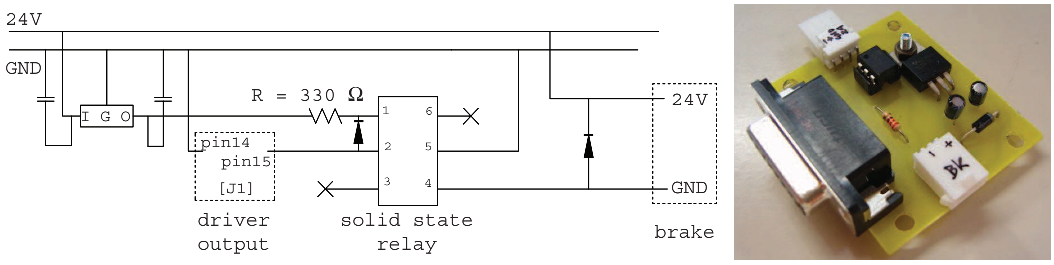

(a) (b)

Figure 4.46: Brake circuit scheme (a) and its implementation on a PCB (b)

the dead points of the travel[11]. These devices also serve as redundant safety sensors, in that they are capable of detecting potential travel overruns before the physical dead points are reached. However, limit switches have also been installed at the actual dead points of the travel which, if activated, cause the *emergency* status.

- **Potentiometer** 4.11.4. A measure of the table orientation is required to compensate the weight of the end-effector (Section 5.6.5). For this reason, a potentiometer has been installed which is coaxial with the right hinge of the table.

Table 4.7 shows the functionalities of each PCB. The PCBs are mounted on the bottom surface of the table, each next to the corresponding drive. In the following, the design of the PCBs is briefly discussed.

4.11.1 Brake

The digital outputs of the drives ($I_{out,\max} = 25mA$, $V_{\max} = 30V$) are not capable of supplying the required current to the brakes. Therefore, each brake is powered by the SP-150-24 power supply, while a digital output of the drive opens and closes the main circuit by means of a solid-state relay (AQV251). The relay, in turn, is energized by a $5V$ voltage regulator (LM7805CT). To adequately limit the current flowing though the digital input, a resistor must be placed in series with the relay LED: with $R = 330\Omega$, $I_{out} \approx 11mA$ (Fig. 4.46(a)). Two capacitors ($C_1 = 330nF$, $C_2 = 220nF$) are placed before and after the voltage regulator to guarantee tension stability in the transient states. Two diodes (1N4007GP) have also been installed. The first one, located in parallel with the internal LED of the relay, protects the LED from damage. The second one, located at the brake terminals, lets the entering currents (due to brakes inductance) reflow in the brake solenoid.

4.11.2 Drive Inhibition & controller enabling

The drives and the controller are capable of detecting the *emergency* status through dedicated digital inputs. These inputs are connected to the contacts of the relay K1. Specifically, the drives input 1 (IN1) is an inhibition command working in negative logic: it is connected to a NC contact of K1, so that the *emergency* status corresponds to a low signal. Conversely,

---

[11] Actually, only one inductive switch is required to perform the homing procedure.

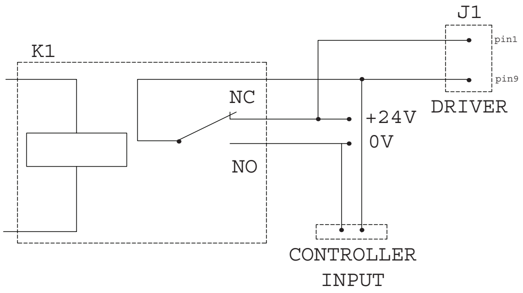

Figure 4.47: Drives inhibit and controller enable

one of the digital inputs of the controller has the function of an enable command, working in negative logic: it is connected to a NO contact of K1, so that the *emergency* status corresponds to a high signal (Fig. 4.47). The drive inhibits have been integrated into the same PCBs used for the brakes (Fig. 4.46(b)).

4.11.2.1 Controller output and watchdog

The μRMC controller (Robox Motion Control) is equipped with 8 digital input channels (PNP, 24VDC) and 8 digital output channels (PNP, 24VDC, $I_{\max} = 0.5A$). The controller possesses also a *watchdog*, i.e., a relay that is de-energized whenever the controller does not reset a dedicated counter (e.g., because of a fault in the software). To increment the safety level, the watchdog contacts have been connected to the safety circuit (Fig. 4.43).

Additionally, to allow the controller software to switch the machine to the *emergency* status, an output command (OUT1) has been employed to energize a relay (Finder 36.11.9.024.000), which has also been inserted in the safety circuit (Fig. 4.48).

4.11.3 Inductive proximity switches

The inductive proximity switches (SI5-C0.8 NPN NO) are three-cable sensors. The brown wire carries the input tension and the blue one is connected to ground (Fig. 4.50). The drive digital input must be connected between the brown and the black wires. If no ferromagnetic

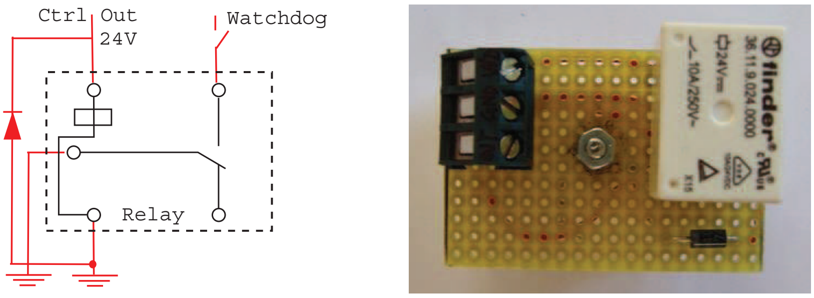

(a)

(b)

Figure 4.48: Controller watchdog and digital output scheme (a). Implementation of the circuit on a PCB (b)

$U_{\min}/U_{\max}[V]$	6/30
$I_{\max}[mA]$	150
$\Delta V_{\max}[V]$	1.4
$f_{\max}[kHz]$	2
range $[mm]$	0.8

Figure 4.49: AECO SI5-C0.8 NPN NO specifications

Figure 4.50: Electric scheme of the proximity sensor

material is detected, the circuit remains open and there is no tension drop between the brown and the black wires (i.e., the digital input is low). Conversely, if ferromagnetic material is detected, the black wire is connected to ground and, therefore, a tension drop arises between the brown and the black wires, which corresponds to a high input signal.

Fig. 4.51 shows the PCB board that has been developed for the drive controlling the screw motor. The corresponding electric scheme is portrayed in Fig. 4.52. This PCB has several I/O ports embedded: beyond the drive inhibit and the brake output (which also characterize the PCBs of the other drives), this PCBs also manages the two inductive proximity sensors and the potentiometer analog input.

The Cello servodrive is equipped with two high-speed inputs that are suitable for homing purposes (IN5, IN6). Fig. 4.52 shows how the signal from the proximity switches (connectors U8, U9) have been connected to the port J2. To prevent the digital inputs from damaging, the supply tension has been reduced to $15V$ through a voltage regulator (LM7815CT): this way, the input current is reduced to a suitable value:

$$I_{in} = \frac{V_{in} - 6.5V}{1250\Omega} = 6.8mA \tag{4.12}$$

Fig. 4.54(b) shows the arrangement of the inductive proximity sensor and of the limit switch at the left dead point of the travel. Note the thin ferromagnetic layer glued on the plastic extension of the trolley to activate the left proximity sensor.

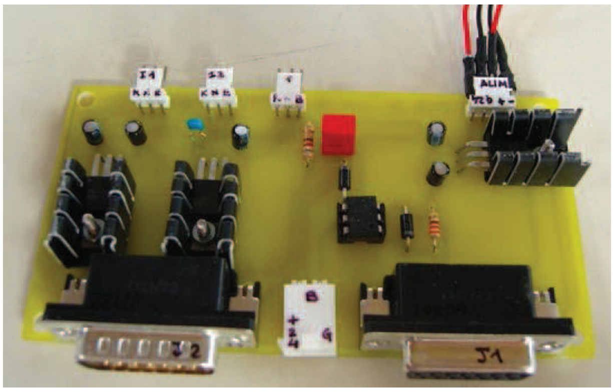

Figure 4.51: Screw servomotor I/O PCB

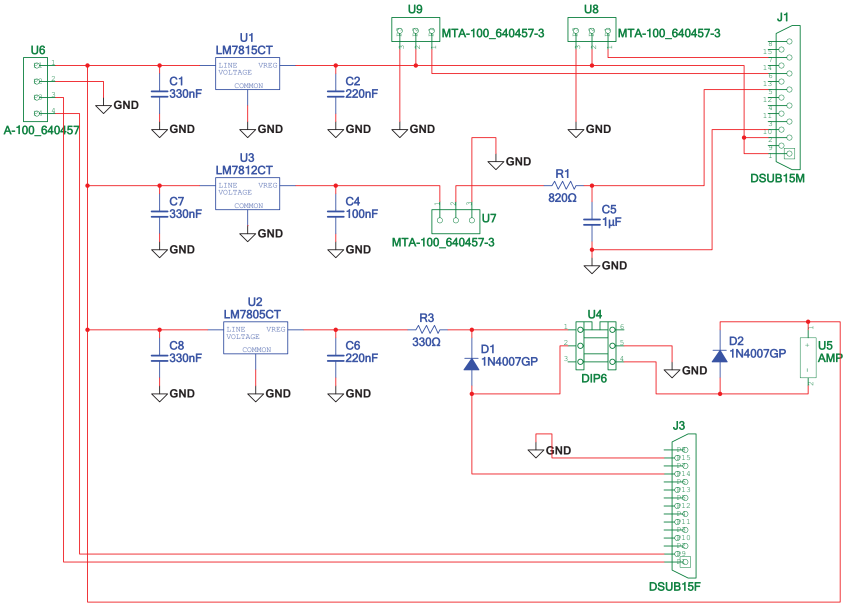

Figure 4.52: Screw servomotor I/O PCB: electric scheme

4.11.4 Potentiometer

During the therapy, the orientation of the table must be measured to compensate the weight the end-effector (Section 5.6.5). Also, this measure is required by the HMI interface that resembles in a VR environment the movements made by the patient. To this end, a potentiometer (Vishay 157 series) was installed as a cost-effective angular position sensor. The main specifications of the potentiometer are outlined in Fig. 4.53.

Fig. 4.54(a) show the support of the potentiometer, which also embeds the 60° limit switch. This support, made of ABS, was manufactured with a fast prototyping device (3D printer). The assembly is located on the right leg of the table, near the right hinge. The design of the device provides self alignment between the axis of rotation of the potentiometer and the axis of the hinge. The shaft of the potentiometer has been partially flattened to insert a lever. When the upper bound of the travel is reached, the lever pushes the limit switch. A simple support was designed also for the 0° limit switch.

The circuit that supplies the potentiometer is embedded in the screw servomotor PCB (Fig. 4.52). The analog input of the drive supports input voltages in the range $0 \div 10V$, therefore a tension regulator (LM7812CT) is employed. Before entering the input port J2, the signal is low-pass filtered with $f_c \approx 200Hz$ ($C = 1\mu F$, $R = 820\Omega$).

Accuracy	$\pm 20\%$
Linearity	$\pm 2\%$
Rotation $[deg]$	340 ± 5
Torque $[Ncm]$	≤ 0.4

Figure 4.53: Vishay 157 series specifications

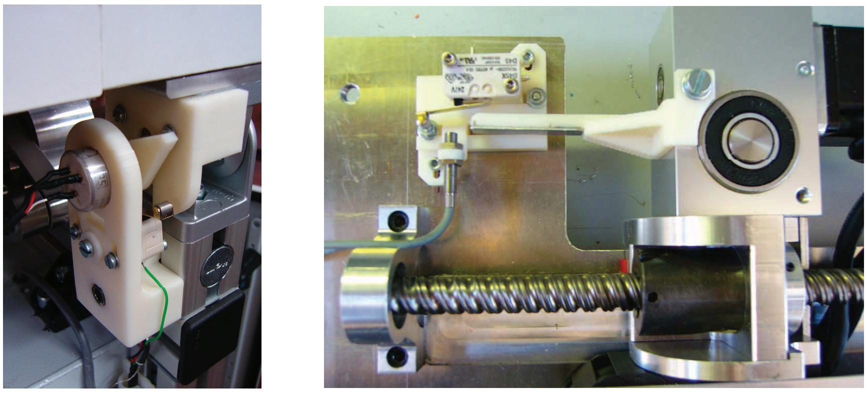

(a) (b)

Figure 4.54: Potentiometer and 60° limit switch assembly (a). Inductive proximity sensor and limit switch at the left dead point of the travel (b).

4.12 New control architecture

After first experimental tests, several issues raised with the Robox μ-RMC controller and the CANopen-based control architecture (Section 5.4). They can be summarized as follows:

- Robox μ-RMC: the CPU (Power PC @ 400MHz) is too slow to perform the required calculations in sufficiently small time cycles. The maximum allowed control frequency is $f_c = 600Hz$, which is quite low for a haptic display.
- Robox Developer Environment (RDE): the software (editor + compiler) which came with the controller had several bugs. New releases have partially fixed those issues, however, the documentation is still poor and technical assistance is not satisfactory.

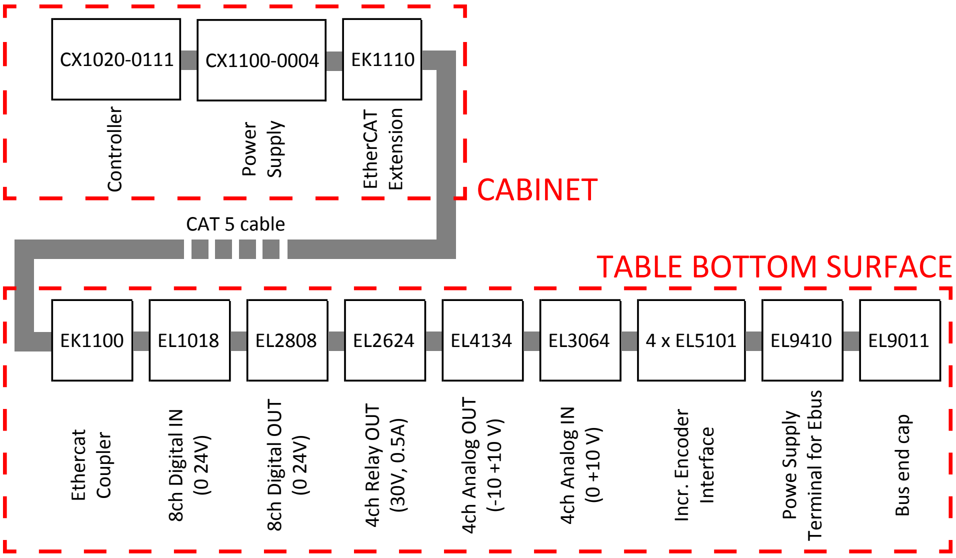

Figure 4.55: New control architecure

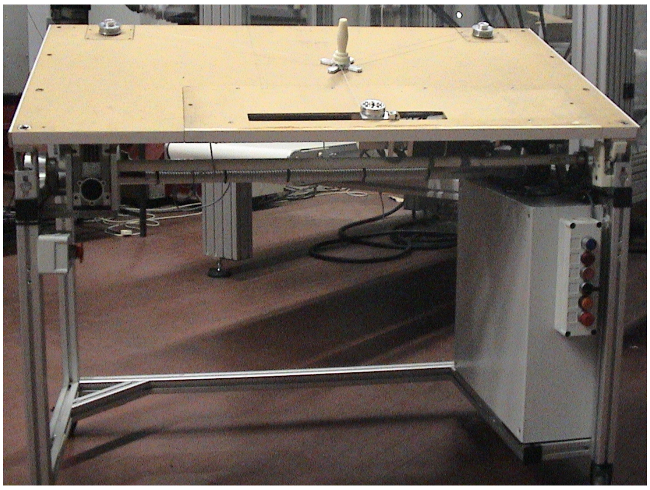

Figure 4.56: The current Sophia-3 prototype, equipped with the new controller and the new moving pulley-block

For these reason, the control hardware architecture was totally redesigned as shown Fig. 4.55. The selected hardware allows for a modular configuration of the control system. Besides the CPU unit, the hardware comprises I/O modules, encoder modules and power supplies. The new architecture is highly centralized and comprises two locations. The CPU module (BECKHOFF CX1020), the main power supply (CX1100) and the EtherCAT module (EK1110) are located inside the cabinet, while all the I/O modules are arranged on the bottom surface of the table. In the new design, we wanted to keep the same drives, which are not compatible with the EtherCAT standard. Thus, all the drives are now controlled in torque mode through analog signals provided by a 4-channel module (EL4134). All the I/O signals are directly controlled by the industrial PC, with the exception of the encoders, whose signals are redirected from the drives to 4 dedicated modules (EL5101).

The brakes are directly energized/de-energized by a relay-based module (EL2624). Signals coming from the inductive proximity switches and from the potentiometer are read by a digital input module (EL1018) and by an analog input module (EL3064), respectively. A digital output module has also been installed to allow the controller to switch the device to the *emergency* status.

All the components have been mounted, and experimental tests with the new hardware will start in a short time.

Chapter 5

Control of Sophia-3

In this chapter, the control architecture of Sophia-3 is described, focusing on the software implementation. The control is based on the CANopen communication protocol, with the controller being the master and the four drives being the slaves. A brief introduction on the CANopen standard is given, followed by an overview of the CANopen layout implemented in Sophia-3. Then, the structure of the software is described in detail.

The algorithms implemented for the low level control of the prototype are also addressed: forward and reverse kinematics, calibration and wire tension distribution and a brief description of a simple active-assistive controller to be used in the rehabilitation exercises is presented.

The last part of this chapter deals with first experimental tests with the new prototype.

5.1 The CANopen protocol

The CAN bus was initially developed by BOSH for the European automotive industry. The idea was to substitute all the wirings required to connect the electronic devices embedded in a car with a unique cable. Nowadays, the CANopen protocol is a standard communication protocol used in automation.

The Controller Area Network (CAN) was developed following a line (*bus*) topology. Data between the controller (*host*) and the *nodes* of the bus are sent in packets. Each device inserted in the bus receives all the data sent by the other devices and is allowed to send data in every instant. Several objects can be inserted in a data packet. PSOs (*Process Data Objects*) are usually employed for time-critical data (e.g., reference commands, control commands, status data, etc.). SDOs (*Service Data Objects*) are employed for non-time-critical data (e.g., configuration parameters). Additionally, there are objects for special functions and objects for controlling the net.

The OD (*Object Dictionary*) is a fundamental element which defines the CANopen architecture. All the data related to the application and those related to the communication are stored in the OD. Each object in the dictionary can be addressed through a 16-bit *index* and a 8-bit *subindex*. The OD can be thought of as a table with 6 columns (Tab. 5.1).

Index	Object	Name	Type	Attribute	M/O

Table 5.1: The CANopen Object dictionary

Index is the field that specifies the position of the object inside the dictionary. *Object* contains the symbolic name of the object. *Name* is a string that describes the object. *Type* indicates the data type (e.g., BOOLEAN, UNSIGNED8, SIGNED16, etc.), *Attribute* indicates the kind of object (e.g., Read/Write, ReadOnly, WriteOnly) and *M/O* means Mandatory or Optional.

SDOs enable accessing the OD through 5 different request/response protocols. The device sending the access request is called *client*, whereas the device whose OD is required is named *server*.

PDOs are transmitted in a non-confirmed mode. Thus, they are faster and thereby suitable for time-sensitive data interchange (e.g., motion control). There are two kind of PDO: Transmit-PDOs (*PDO Tx*) are used to transmit packets, whereas Receive-PDOs (*PDO Rx*) are used to receive data.The sending device (*producer*) sends a Transmit-PDOs with a specific identifier, which corresponds to the identifier of the Receive-PDO of one or more *consumers* (devices waiting for the data packet). Before sending PDOs, they must be mapped (i.e., objects of the OD are assigned to the PDO). Once a PDO has been mapped, there is no need to reference OD objects explicitly.

PDOs can be further classified into synchronous and asynchronous PDOs. *Synchronous Cyclic* PDOs are transmitted within the synchronous window. The number of Sync Objects between two PDO transmissions can be set in the range $1 \div 240$. *Synchronous Acyclic* PDOs are transmitted within the synchronous window and only after prior reception of the Sync Object, however, unlike the previous subclass, their activation is event-based and can therefore be non-periodic. *Asynchronous* PDOs are event-controlled as well. However, they are immediately transmitted when at least one of the process variables mapped in the PDO is altered.

In the CANopen bus, devices can be controlled via *controlwords* and *statuswords*. The former are used to command transitions between the states, therefore they are associated to write PDOs. Statuswords are used to monitor the current state of a device, therefore they are associated to read PDOs.

5.2 CANopen setup

The CANopen network of Sophia-3 comprises a *master* (Robox $\mu - RMC$ controller) and 4 *slaves* (Elmo Cello drives). Each device must be assigned to a unique ID in the range [1...127]:

- nodeID = 10, motor 1 drive (upper right pulley-block);
- nodeID = 20, motor 2 drive (upper left pulley-block);
- nodeID = 30, motor 3 drive (lower pulley-block);
- nodeID = 40, motor 0 drive (screw motor);

The baud rate must be set to the same value for all the connected devices[1]. In this application, we set the baud rate to the maximum feasible value (i.e., 1Mbit/s).

Due to the low-level control algorithms (Section 5.6) the maximum frequency of operation in this application is 600Hz, which corresponds to $\Delta t \approx 1.67ms$[2]. The time cycle for

---

[1] In principle, devices with a different baud rate can be connected as well, without generating any error message. However, only the devices with the same baud rate as that of the master will be detected

[2] This value has been determined after several tests

the communication is about $1ms$, thereby the CPU computational load is the critical issue of this application.

The CANopen setup data can be configured from a PC connected to the controller via ethernet. The data are then downloaded to the controller flash drive in the file *coc0.cfg*. This file is read by the controller during the boot-up. Data comprise the CAN-bus configuration parameters (bit rate, sync frequency, etc.) as well as the parameters of the single workstations (PDO mapping).

5.3 Driver Elmo Cello - Modes of operation

The Cello servodrives support the CANopen communication protocol. They can be set in several *modes of operation*:

- Profiled position mode
- Velocity
- Profiled velocity mode
- Torque profiled mode
- Homing mode
- Interpolated position mode

In the Sophia-3 prototype, the last three modes were utilized. A software is provided by the manufacturer which allows to set the configuration parameters and test all the functionalities of the drive through a PC and a serial interface. Specifically, the modes of operation and all the I/O functionalities can be tested. Also, a wizard procedure allows the auto-tuning of the controller gains (Current Loop, Velocity Loop, Position Loop) for the connected motor, whose shaft should be already connected to the load. The same functionalities are also available via CANopen. In the following, a brief description of the used modes of operation is given.

5.3.1 Torque profiled mode

In this mode, the drive controls the torque exerted by the servomotor, based on the current feedback. Shaft speed and position are monitored as well, so as to avoid exceeding the corresponding encoder position and velocity limits (these limits can be set through the drive configuration utility). The following parameters need to be set when operating in this mode:

- Motor max current
- Motor rated current $[mA]$
- Motor rated torque $[mNm]$
- Torque slope $[1000\ mNm\ s^{-1}]$
- Target torque

The *Motor max current* parameter is defined in thousandths of the rated current, that is, for a rated current $I_n = 3200mA$ and for a maximum current $I_{\max} = 4000mA$, this field should be set to 1250. The *Torque slope* parameter indicates the slope of the linear ramp command used to reach the target value. It must be specified in thousands of the actual slope. The object *Target torque* defines the current reference torque. Again, it must be specified in thousands of the rated torque.

This control mode is used for motors 1 and 2 (fixed pulley-blocks). Motor 3 is also controlled in torque mode until the end of the calibration process.

5.3.2 Homing mode

This operating mode should be used to reset the encoder counter at each boot up of the device. The method uses a limit (or proximity) switch that may be located either at one end of the travel or between the extremities of the travel. The objects that must be defined are:

- Home Offset [encoder increments]
- Homig Method
- Speed during search for switch $[rpm]$
- Speed during search for index $[rpm\ s^{-1}]$
- Homing Acceleration

There are different homing methods, depending on the disposition of the limit switches within the travel, on the direction of the movement, and on the position of the index pulse (when required). To reduce the overall time required for the homing process, a higher speed should be imposed when searching for the switch (coarse positioning), whereas a lower speed is to be imposed when searching for the encoder index (fine positioning). The *home offset* allows to set the actual *zero* at a given distance from the limit switch. The CANopen protocol allows to start the homing process (*statusword*) and to verify the status of the homing process (*controlword*).

5.3.3 Interpolated position mode

In the *Interpolated position* mode, reference positions are sent by the controller through the CANopen bus, either continuously or in data packs. Data are collected in a dedicated buffer, thereby allowing to send multiple points at the same time. This can be useful to save the CPU

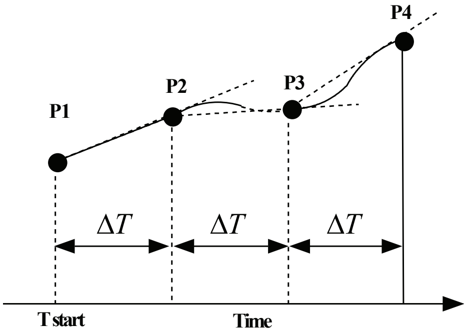

Figure 5.1: Interpolated position mode: cubic polynomial interpolation A

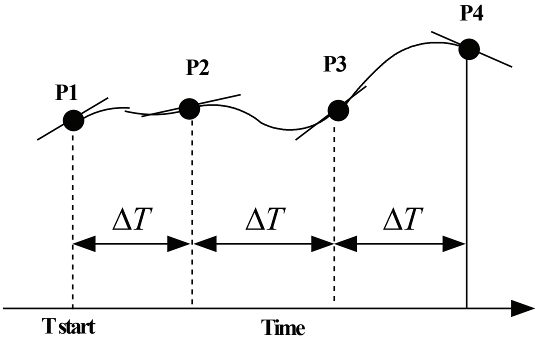

Figure 5.2: Interpolated position mode: cubic polynomial interpolation B

load when real-time is not a strict concern (e.g., positioning of the moving trolley). The data in the buffer are then interpolated by the drive, and a continuous reference law is created. The objects required by this mode of operation are the following:

- **Interpolation sub mode select:** This object defines the type of interpolation, and it can be set to -1 [Cubic spline] or 0 [Linear interpolation]. Despite the misleading names, it is easy to understand that both the interpolation modes employ third-order polynomials (Fig. 5.1, Fig. 5.2). In the former, the user must specify the velocity at each each via point, whereas in the latter the velocity at the end of each time interval is automatically set to the average velocity in the same interval.
- **Interpolation data record:** This object contains the data to be interpolated.
- **Interpolation time period:** This object consists of two data, sub_1 and sub_2, which set the interpolation time interval ΔT according to the expression:

  $$\Delta \mathrm{T} = \mathrm{sub}_1 \; 10^{\mathrm{sub}_2} \; [\mathrm{s}] \tag{5.1}$$

  thus, for $\mathrm{sub}_2 = -3$, sub_1 gives the interpolation interval in $[ms]$. This parameter should be chosen carefully to ensure a smooth trajectory.
- **Interpolation data configuration** This object describes the configuration parameters of the buffer.

The controlword and statusword are employed to enable the interpolated mode (controlword) and to verify that the drive is ready to receive the via points (statusword).

5.4 Real-time software

The programming language supported by the Robox μ-RMC controller is called *R3*. This is a compiled language, i.e., the source code needs to be converted to machine code before being downloaded into the flash memory card of the controller. Two are the main types of scripts that the compiler allows to handle: the *rules* and the *main instructions*. The former comprises all the codes that are required to describe the motion laws of the machine, while the latter contains the operative sequences of the device.

The *rules* are essentially synchronous tasks, wherein the execution time must be chosen according to the dynamics of the controlled process. When programming a rule, only linear programming is allowed. That is, event waiting and blocking/infinite loops are not allowed. The priority (and, therefore, the computational resources) assigned to the rules is greater than the one assigned to the operative instructions. Rules are used to handle the movements of the machine, including position and velocity loops, on-line trajectory planning and synchronization of several axes. Clearly, all the required operations must be processed during the *execution time*. The control frequency can be set in the range $200 \div 1000 Hz$, and it should be higher than the highest frequency of the controlled dynamics. Each cycle time is capable of handling up to 32 rules.

Main instructions describe the functioning of the machine, and allow standard real-time programming. Up to 8 different tasks may be managed by the controller. However, the user cannot set their priority manually, since all the tasks share the same priority by default. When

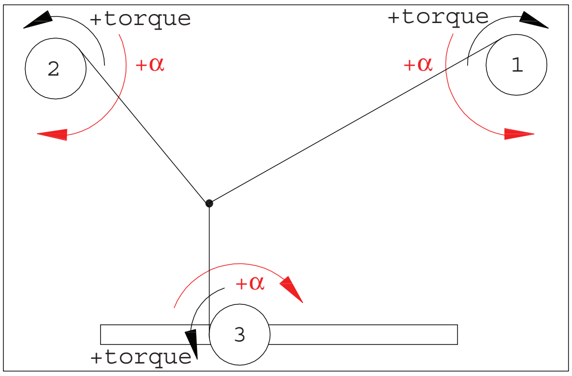

Figure 5.3: Positive directions for torques and angles

the controller is turned on, only task 1 is executed, thereby other existing tasks must be executed by task 1.

5.4.1 Structure of the code

The real-time software of Sophia-3 consists of 4 tasks:

- TASK0: *rulez*. This script contains the instructions that are related to the movements of the controlled DOFs: the functions that compute the torque/position reference values for the motors and the function that modifies the position feedback provided by the encoders (Section 5.6.3).
- TASK1: *main*. This is the most important task of the control architecture. Indeed, it manages the *finite-state machine* of Sophia-3 (Section 5.4.2).
- TASK2: *allarm*. This task guarantees a safe functioning of the device. Indeed, it performs a set of safety checks and it might switch the device to the *emergency status*.
- TASK3: *cin_dir*. This task manages the forward kinematics algorithm (Section 5.6.1) and the wire tension distribution algorithm (Section 5.6.5).

A fifth task, called TASK4, has also been hypothesized, through not implemented yet. This task is responsible for *data logging* during the therapies.

5.4.1.1 TASK0: rulez

The following rules have been implemented in this task:

- The rule *read_enc* uses an embedded function of R3 that gets data from the encoders and automatically manages the exceeding of the upper and lower limits of the counter.
- The rule *offset_enc* corrects the encoder inputs according to the offset values defined during the calibration process. Indeed, unlike the screw servomotor, for which the encoder counter is automatically reset through the homing procedure, in the other servomotors the reset procedure must be done manually. To overcome this issue, two auxiliary registers have been created: the first one contains the original encoder data in the point of calibration (*enc_Act_calib*), whereas the second one contains the values

to be assigned to the encoders at the same point, according to the notations developed in the forward kinematics algorithm (5.6.3).
Thus, if we denote as *act_pos* the feedback of a particular encoder (as provided by the rule *read_enc*), the modified position input is given by:

$$\text{encAct} = (-\text{act\_pos} + \text{encAct\_calib}) + \text{enc\_calib} \tag{5.2}$$

The minus sign is due to the raw encoder inputs increasing in the positive direction set for the torques. We set the positive directions of the torques as the ones that generate a positive tension in the cables (Fig. 5.3). However, the notation developed for the forward kinematics set the positive senses of rotation for the angles α as the ones causing the cables to unreel (Section 5.6.1). Because of this discrepancy, an increase in the encoder counts determines a reduction in the corresponding value of α, which are proportional to the corrected value encAct:

$$\alpha = \frac{2\pi}{k_{red}\, n_{CPR}} \text{encAct} \tag{5.3}$$

where k_{red} is the reducing ratio of the potentially installed reducer and n_{CPR} is the number of counts per round of the encoder.

- The rule *CoppiaMin* controls the three pulley-block servomotors in torque mode during the homing of the screw motor. In this phase, the reference torques are set to the minimum feasible value (i.e. the one corresponding to $f_{\min} = 5N$). The aim is to keep the cables stretched while the calibration of the linear axis is performed.
- The rule *PosInizVite* is enabled once the homing process has been completed. Its function is to position the lower trolley to the x coordinate corrsponding to the calibration point of motor 1 and motor 2.
- The rule *ControlloCoppia* applies to motor 1 and motor 2 only. This function provides each motor with the torque command corresponding to the cable tension computed by the wire tension distribution algorithm (Section 5.6.5).
- The rules *ControlloPos* and *ControlloVite* manage the position control of motor 3 and motor 0: they compute the interpolation data records to be feed to the drives.

5.4.1.2 TASK1: main

All the states the device can assume are implemented inside this task. The variable describing the status (*stato_robox*) may take the following values:

- *Accensione (Switching on);*
- *AttesaMarcia (Waiting for enable);*
- *AttesaCalibrazione (Waiting for calibration);*
- *Homing*;
- *AttesaOkCalibrazione (Waiting for completion of the calibration process);*
- *AttesaRilascio (Waiting for end-effector releasing);*
- *AttesaComandi (Waiting for commands);*
- *ControlloTraiettoria (Trajectory control);*

- *Arrivato (Task completed);*
- *Emergenza (Emergency);*

The task consists of a main loop containing a "switch case" structure based on the value of *stato_robox*. Thanks to this structure, the controller is capable of selecting the sequence of operations required by the current status. The finite-state machine is described in detail in Section 5.4.2.

5.4.1.3 TASK2: allarm

The task *allarm* can switch the status of the device to *Emergency* if a fault is identified. When the task is executed, if resets the alarm stack and activates a loop wherein the following checks are performed:

- **Encoder cable disconnection:** This check can be easily done for the motors 1 and 2, which are controlled in torque mode. Indeed, this modality always implies a certain variation of the encoder feedback, even when the motor is approximately stationary. Thus, by buffering the last n encoder inputs, the variance is computed: a null variance clearly indicates the cable disconnection. For motors 0 and 3 (which are controlled in position mode), the condition of fault can be detected by imposing a threshold on the tracking error.
- **CANopen cables disconnection:** This condition can be easily checked for each axis by using the embedded function: AM(axis number).
- **Failure of one of the end-effector cables:** When a cable fails, the theoretical static equilibrium is no longer guaranteed, and one motors start a free-run. This conditions can thus be detected by monitoring unfeasible results in the forward kinematics.
- **Inductive proximity switches fault:** After the calibration of the linear DOF, the corresponding encoder input can be monitored. If no signal from the inductive switches is detected when the trolley pass through the position of one of the sensors, the control switches to the *emergency* status before the trolley reaches the limit switch.

Switching to the *Emergency* status is achieved both at the software level and at the hardware level. Indeed, first the controller opens the safety circuit by means of the dedicated output (Section 4.11.2) and then it manages the system restoring process by choosing one among the possible modalities. Clearly, the chosen modality depends on the cause of the fault. In most of the cases, the restoring process can bring the machine directly to the calibration of motors 1, 2 and 3, without repeating the homing phase. Restoring the machine form the homing phase is useful whenever the cause of the fault cannot be automatically determined.

5.4.1.4 TASK3: cin_dir

The structure of the code, also reported in Fig. 5.4, can be described as follows:

- **Forward kinematics:** This section of the code implements the algorithm described in Section 5.6.1.

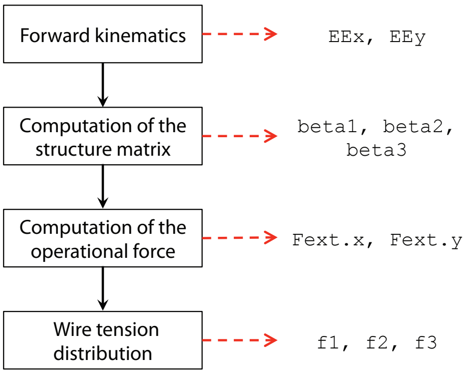

Figure 5.4: Structure of cin_dir and corresponding output variables

- **Computation of the structure matrix:** Given the angles α and θ, the structure matrix (5.40) is computed as described in Section 5.6.5.
- **Computation of the operational force:** The algorithm computes the force $\mathbf{F}$ to be exerted at the end-effector, given the current position, the current shape of the elliptical force tunnel and the orientation of the table. Thus, this chunk of code manages the impedance controller of the device (Section 5.6.4).
- **Wire tension distribution:** The set of tensions that corresponds to the desired operational force is computed as described in Section 5.6.5. This code provides the inputs for the rules *ControlloCoppia* and *ControlloPos*.

5.4.2 Finite-state machine

Fig. 5.5 depicts the UML diagram of the finite-state machine that has been implemented in Sophia-3. The labels written in RED CAPITAL LETTERS identify the states (i.e., the value assumed by the variable *stato_robox*). Labels written in *italics* represent external actions (e.g., inputs from the user, commands from the host PC, etc.). Yellow textboxes describes the state transitions, which take place whenever the expression:

```
comando= string_identifying_the_new_state
```

is executed. Finally, green textboxes indicate rule enabling.

When the device is turned on, the operating system performs a set of hardware and software checks. If no technical fault is detected, the user code named *main* - which corresponds to TASK 1 - is executed (Section 5.4.1.2). The latter, in turn, enable the rule named *allarm* (Section 5.4.1.3). The state transition to ATTESAMARCIA (*waiting for enable*) occurs automatically.

The state named ATTESACALIBRAZIONE (*waiting for calibration*) is reached once the user has pushed the start button located on the button panel of the device *and* the controller receives the string:

```
comando= abilitamarcia
```

from the host PC. In this state, the motors of the pulley-block are controlled in torque mode through the rule *CoppiaMin*. This approach is required to prevent cable slackening during the homing process and during the first phase of the calibration process. Then, the system automatically switches to the next state.

In the state called HOMING, the encoder of the screw servomotor is reset. This procedure is completely managed by the screw motor drive through a dedicated operative mode called *homing* (Section 5.3.2). The screw rotates in the prescribed direction until the trolley reaches the left proximity switch. When the corresponding digital input is turned on, the encoder is reset. Once the homing process has been completed, the rule *PosizInizVite* is activated and the trolley moves to the x coordinate of the reference point used in the first phase of the calibration process (Section 5.6.3). The next state transition ATTESAOKCALIBRAZIONE (*waiting for completion of the calibration process*) is performed automatically.

The user is now asked to position the end-effector on the reference point marked on the table surface. While the end-effector is held in position, the host PC send the instruction:

`comando=` `okcalibrato`,

which activates the calibration process. Afterwards, the encoders of motor 1 and motor 2 are correctly reset, the rule *EncOffset* is enabled for these motors and the forward kinematics task is activated as well[3] (Section 5.6.1). The state is then switched to ATTESARILASCIO (*waiting for end-effector releasing*), and the user is asked to release the joystick to enable the second phase of the calibration process.

The string:

`comando=` `ok`

enables the calibration of the moving pulley-block motor. Cable tensions are gradually increased so as to reach a new static equilibrium, then the reset of the encoder 3 is completed (Section 5.6.3). Once the calibration process is finished, the rule named *ControlloVite* is activated, whose aim is to provide the position loop of the screw servomotor with the reference input, as it is computed by the forward kinematics algorithm[4]. Thus, when moving the joystick, the trolley tracks its movements, seeking to keep orthogonality between the cable and the linear guide.

In the meanwhile, the next state, named ATTESACOMANDI (*waiting for commands*) is activated. This state, in turn, enables the rules *ControlloCoppia* and *ControlloPos*, which allow the device to start the therapy.

The command:

`comando=` `es_punto_punto`

makes the controller switch to the next state, named CONTROLLOTRAIETTORIA. (*trajectory control*). This state corresponds to a single point-to-point motion (i.e., to a single side of

---

[3] In this phase, only the feedback inputs from motor 1 and motor 2 are used to compute the current position of the end-effector.

[4] Once the second phase of the calibration has been completed, also encoder 3 is used in the forward kinematics algorithm.

the polygon defining the reaching task, see Section 5.6.4). The patient is asked to move the joystick from a starting point to an end point, while the active-assistive controller provides help, according to the assist-as-needed paradigm.

The string:

```
comando= arrivato
```

indicates that the patient has reached the target point of the current task. This command makes the controller switch to the state ARRIVATO (*Task completed*).

The next state can be either ATTESACOMANDI (*waiting for commands*) or CONTROLLOTRAIETTORIA (*trajectory control*), depending on the value of the string **comando**. The command line:

```
comando= fineterapia
```

indicates that the current exercise is terminated, therefore the controller is set in a stand-by state (ATTESACOMANDI) until a new exercise is defined. Conversely, the string:

```
comando= es_punto_punto
```

makes the controller switch to the state CONTROLLOTRAIETTORIA with an updated goal point.

Fig. 5.5 outlines the layout of the finite-state machine implemented in Sophia-3. Though not specified in the outline, the EMERGENZA (*emergency*) status can be accessed from any other status. Indeed, a dedicated task (*allarm*, Section 5.4.1.3) identifies the cause of the fault, switches the status to EMERGENZA and open the safety circuit.

Restoring the functionality of the device after a fault requires two actions. Indeed, the user must set the digital output *ripristinoemergenza* (*emergency restoring*) to the high value first, and then push the *start* button on the button panel. The former action closes the safety circuit, while the latter energizes the same circuit. Notice that two are the states that can be reached from the EMERGENZA status: if the fault requires the homing process to be performed again, then the status HOMING is selected, otherwise the status ATTESAOKCALIBRAZIONE (*waiting for completion of the calibration process*) is selected.

5.4.3 Graphic User Interface (GUI)

As described in the previous section, all the state transitions requires a certain command line to be sent from the host PC to the controller. In the near future, a GUI running on the host PC will provide a user-friendly environment wherein the therapist can interact with the machine (e.g., by simply pushing command buttons).

The graphical interface (Fig. 5.6), though already implemented, has not been connected to the controller yet. From the interface, not only the therapist will be able to set the main parameters of the therapy in an intuitive way, but also the patient will be provided with visual feedback consisting of a VR environment wherein his/her movements are reproduced.

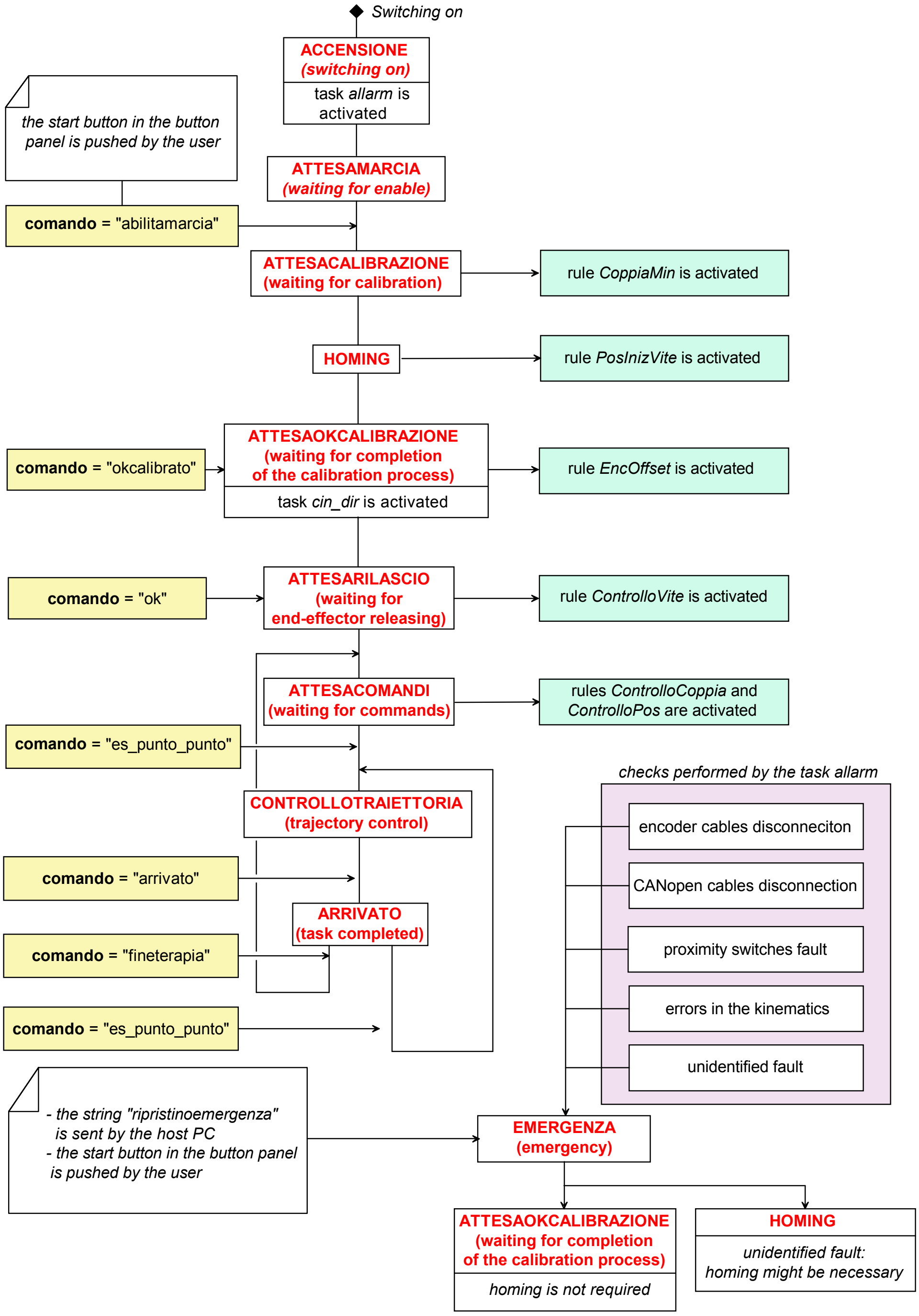

Figure 5.5: Finite-state machine of Sophia-3

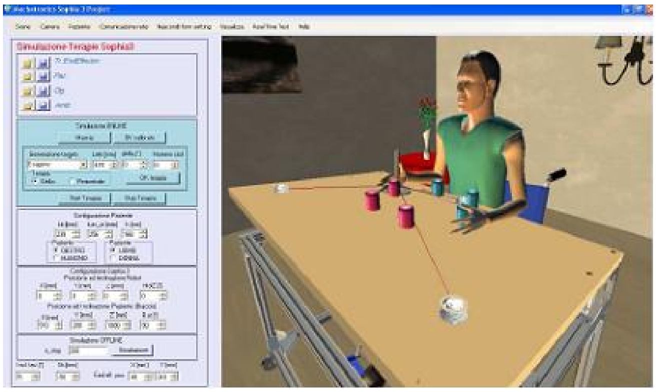

Figure 5.6: GUI snapshot

5.5 Brushed DC drive: finite-state machine

This Section deals with the realtime software that has been implemented in the custom-made drive which controls the brushed DC motor. The main objective of the drive is to provide trapezoidal input tension profiles to the BDC brushed motor. As compared to the simple on/off law (*step* input), these profiles allow for smoother movements of the table. Indeed, being the orthogonal gearbox non-backdrivable, high vibrations were generated on the table when the input tension dropped down to zero.

The microcontroller manages four digital inputs and three digital outputs. The digital inputs called INHBT0 and INHBT1(pins 2 and 3 of the dsPIC microcontroller) correspond to the limit switches at $0°$ and $60°$, respectively. A high signal means that the table has reached the corresponding extremity of the travel, thereby all the subsequent down-directed motion commands must be ignored.

The digital inputs called INHBT_DIR0 and INHBT_DIR1 (pins 4 and 5) correspond the motion commands *down* and *up*, respectively. They are set in negate logic, i.e., a low signal means that motion should start in the prescribed direction.

The digital outputs CTRL_A and CTRL_B (pins 38 and 36) are connected to two PWM output ports of the microcontroller (PWM1L and PWM2L). These ports controls the power MOSFETs of the H-bridge through the BJTs. The duty cycle of the PWM is visualized by two LEDs. The third digital output, called LED_STATUS (pin 30), is connected to the status LED. This LED gives information about the current status of the drive by blinking at different frequencies.

The code runs on the real-time OS of a 16-bit microcontroller (dsPIC30F3011, Section 4.10). It was written in C++, compiled and then downloaded into the microcontroller.

Fig. 5.7 depicts the *finite-state machine* implemented in the dsPIC. When the microcontroller is turned on, the default status is *stand-by* and the variable indicating the direction of motion is set to *WAIT*. This status reduces the power dissipated when the table is not moving (i.e, the microcontroller is idle).

A set of checks is performed at each cycle-time ($f \approx 2000 Hz$) before entering the speci-

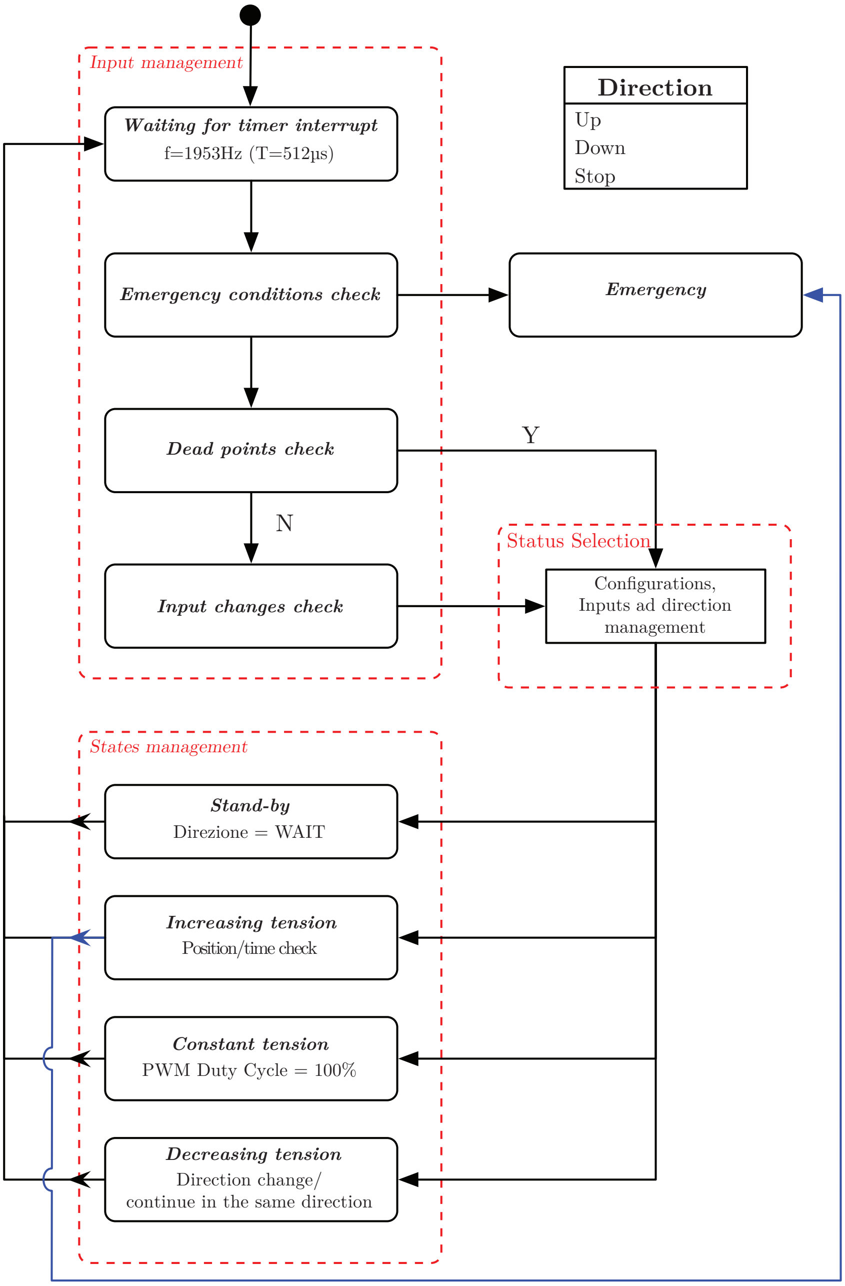

Figure 5.7: layout of the finite-state machine implemented on the microcontroller

fied status[5]. These checks comprises the *emergency conditions check*, the *dead points check* and the *input changes check*.

The *emergency conditions check* verifies potential discrepancies in the input signals (i.e., INHBT0 and INHBT1 simultaneously set to high, INHBT_DIR0 and INHBT_DIR1 simultaneously set to low). If a discrepancy is detected, then the system switches to the *Emergency*

---

[5] Since a unique task has been implemented, all the checks are performed necessarily before processing the instructions corresponding to the current status)

status: PWM signals are zeroed an deactivated, all the motion commands are inhibited and the board needs to be reset through the reset button. The status led blinks with a certain frequency, depending on the detected fault.

The *dead points check* reads the values of INHBT0 and INHBT1: if a limit is reached, the active PWM is zeroed and disabled, the status is set of stand-by and only the movements in the opposite direction are allowed.

The *input changes check* monitors the values of INHBT_DIR0 and INHBT_DIR1. If no changes are detected, the status is the same as the one in the previous cycle time.

After these checks, the motion instructions are processed. The state to be imposed in the current time cycle is determined by a dedicated control unit (*Status Selection* block in Fig. 5.7). Besides the stand-by mode, there are three different states corresponding to the three phases of the trapezoidal tension profile (*increasing tension*, *constant tension* and *decreasing tension*). As long as motion is allowed in a given direction, the tension increases linearly from zero to the maximum value (i.e., the duty cycle is $\delta = 100\%$) in a predefined time interval ($\Delta t = 1s$). If the selector is then switched to the central position, tension is progressively reduced to zero with the same slope. Changes of direction during the linear ramps are also allowed. Additionally, a position/time check is performed when departing from an extremity of the travel: if the corresponding INHBT signal does not change to low in a sufficiently small amount of time, the status is switched to *Emergency*.

5.6 Low-level control algorithms

5.6.1 Forward kinematics

In the Sophia-3 prototype there are no fixed attaching point to the base, and all the wires are directly reeled on the pulleys. Let us consider a frame attached to one of the pulleys. As the cable unrolls, the tip of the cable (as seen from the local frame) describes an involute, whose base circle coincides with the pulley. Thus, the centroid of the end-effector constantly belongs to three different involutes, and the forward kinematics may be solved by imposing the condition of congruence between the "tips" of two of these curves. In the following analysis,

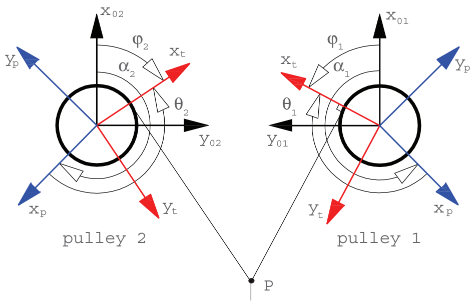

Figure 5.8: Frames used in the forward kinematics

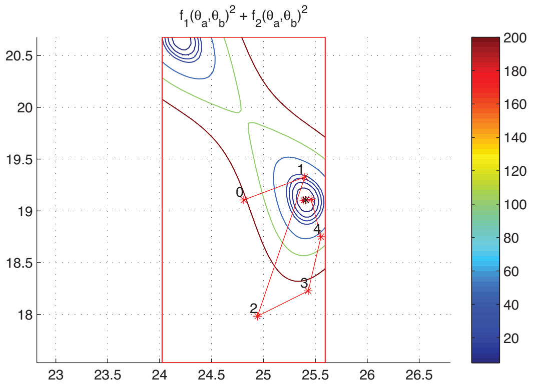

Figure 5.9: Contour lines of function (5.14) and steps of the algorithm

cables are first assumed as *massless elements* with *infinite stiffness*. Then, a method is proposed to take into account cable elasticity.

Let us consider two of the pulleys, say, the one in the upper right corner (pulley 1) and the one on the upper left corner (pulley 2). The starting point of the proposed method consists in defining three different frames for each pulley. First, we define the *fixed* frames $\{01\}$ and $\{02\}$ as in Fig. 5.8. Notice that the y axes are directed towards the centre of the adjacent pulley and the z axes identify the positive sense of rotation, which is defined here as the one causing the wire unreeling. Then, we identify the frames $\{01_t\}$ and $\{02_t\}$ as the ones obtained by rotating the fixed frames around the z-axes until the x-axes intersect the points of tangency between the pulleys and the corresponding wire. The angles of rotation are called θ_1 and θ_2. Finally, the local frames $\{01_p\}$ and $\{02_p\}$ are attached at the corresponding pulleys in such a way that, when $\theta = 0$ for a pulley, the tangent and the local frames are coincident. The orientations of these frames w.r.t. the fixed frames are defined by the angles α_1 and α_2, which are directly correlated to inputs provided by the encoders.

The forward kinematics consists in writing the position of the end-effector centroid P in each fixed frame (i.e., as a function of α and θ), converting the latter expression into the same fixed frame (e.g., $\{02\}$), and finally imposing the condition of congruency. Thus, the forward kinematics problem is turned into one involving the solution of a system of two transcendental equations in the unknowns θ_1 and θ_2.

In the generic tangent frame, the components of P are:

$$ {}^{t}P = \left\{ \begin{array}{c} ra \\ ra\;\theta \end{array} \right\} \tag{5.4} $$

with ra being the pulley radius and θ the cable wrapping angle. Through the rotation matrix ${}^{p}_{t}R$, which describes the orientation of the tangent frame with respect to the pulley frame, we get the expression of P in the pulley frame:

$$ {}^{p}P = {}^{p}_{t}R\,{}^{t}P = \left[\begin{array}{cc} cos\theta & sin\theta \\ -sin\theta & cos\theta \end{array} \right] \left\{ \begin{array}{c} ra \\ ra\;\theta \end{array} \right\} \tag{5.5} $$

In a similar fashion, through ${}^{0}_{p}R$ we get the expression of P in the fixed frame:

$$ {}^{0}P = {}^{0}_{p}R\,{}^{p}P = \left[\begin{array}{cc} cos\alpha & -sin\alpha \\ sin\alpha & cos\alpha \end{array} \right] \left[\begin{array}{cc} cos\theta & sin\theta \\ -sin\theta & cos\theta \end{array} \right] \left\{ \begin{array}{c} ra \\ ra\;\theta \end{array} \right\} = ra \left\{ \begin{array}{c} cos\varphi - \theta sin\varphi \\ \theta cos\varphi + sin\varphi \end{array} \right\} \tag{5.6} $$

where $\varphi = \alpha - \theta$. By substituting θ_1 and φ_1 (θ_2 and φ_2) into (5.6), the expression of ${}^{01}P$ (${}^{02}P$) is derived. In order to impose the conditions of congruency, the aforementioned expressions ${}^{01}P$ and ${}^{02}P$ must be converted to the same reference frame, say, $\{02\}$. Thus, by using homogeneous coordinates, ${}^{02}\left({}^{01}P\right)$ is yielded by:

$$ \left\{ \begin{array}{c} {}^{02}\left({}^{01}P\right) \\ 0 \\ 1 \end{array} \right\} = {}^{02}_{01}T \left\{ \begin{array}{c} {}^{01}P \\ 0 \\ 1 \end{array} \right\} = \left\{ \begin{array}{c} ra\;cos\varphi_1 - ra\;\theta_1\;sin\varphi_1 \\ -ra\;\theta_1\;cos\varphi_1 - ra\;sin\varphi_1 + d \\ 0 \\ 1 \end{array} \right\} \tag{5.7} $$

${}^{02}_{01}T$ is the transformation matrix describing the configuration of $\{01\}$ w.r.t $\{02\}$:

$$ {}^{02}_{01}T = \begin{bmatrix} 1 & 0 & 0 & 0 \\ 0 & -1 & 0 & d \\ 0 & 0 & -1 & 0 \\ 0 & 0 & 0 & 1 \end{bmatrix} \tag{5.8} $$

and d is the distance between the origins of $\{01\}$ and $\{02\}$. By imposing the congruency condition:

$$ {}^{02}({}^{01}P) = {}^{02}P \tag{5.9} $$

we get the following system of nonlinear (transcendental) equations:

$$ \begin{cases} cos\varphi_2 - \theta_2 sin\varphi_2 = cos\varphi_1 - \theta_1 sin\varphi_1 \\ \theta_2 cos\varphi_2 + sin\varphi_2 = -\theta_1 cos\varphi_1 - sin\varphi_1 + \dfrac{d}{ra} \end{cases} \tag{5.10} $$

Here, θ_1 and θ_2 are the unknowns, whereas α_1 and α_2 (which appear in φ_1 and φ_2) are known parameters, derived from the encoders. As shown in (5.19), determining θ_1 and θ_2 allow to find P. Since there is no close-form solution for (5.10), a numerical method must be employed. First simulations with the *Newton-Raphson* method showed numerical instability, especially when approaching the singularities. Thus, the *Newton's Method for Unconstrained Optimization* [98] was chosen, which allows to find local minimum points of a real-valued function $f(\mathbf{x})$.

Let $f(\mathbf{x})$ be a real valued function, whose local minimum point $\bar{\mathbf{x}} \in \mathbb{R}^n$ is to be determined. For $\mathbf{x}$ sufficiently close to $\bar{\mathbf{x}}$, $f(\mathbf{x})$ can be well approximated with its Taylor's expansion truncated to the second order:

$$ f(\mathbf{x}) \approx h(\mathbf{x}) \doteq f(\bar{\mathbf{x}}) + \nabla f(\bar{\mathbf{x}})' (\mathbf{x} - \bar{\mathbf{x}}) + \frac{1}{2} (\mathbf{x} - \bar{\mathbf{x}})' H(\bar{\mathbf{x}}) (\mathbf{x} - \bar{\mathbf{x}}) \tag{5.11} $$

where $\nabla f(\mathbf{x})$ is the gradient of $f(\mathbf{x})$, $H(\mathbf{x})$ is the Hessian of $f(\mathbf{x})$ and $h(\mathbf{x})$ is the real-valued quadratic function that approximates $f(\mathbf{x})$ in a neighborhood of $\mathbf{x}$. We now compute $\nabla h(\mathbf{x})$ and set it to the null vector in order to find the critical points of $h(\mathbf{x})$:

$$ \nabla h(\mathbf{x}) = \nabla f(\bar{\mathbf{x}}) + H(\bar{\mathbf{x}}) (\mathbf{x} - \bar{\mathbf{x}}) = \mathbf{0} \tag{5.12} $$

thus:

$$ \mathbf{x} - \bar{\mathbf{x}} = -H^{-1}(\bar{\mathbf{x}}) \nabla f(\bar{\mathbf{x}}) \tag{5.13} $$

The term in the right-hand side of (5.13) is usually referred to as the *Newton step*. The numerical algorithm can be summarized as follows:

- **step 0:** choose an initial guess $\mathbf{x}^0$ ($k = 0$).
- **step 1:** compute the k-th step $\mathbf{d}^k = -H^{-1}(\mathbf{x}^k) \nabla f(\mathbf{x}^k)$.
- **step 2:** if $\|\mathbf{d}^k\|$ is sufficiently small, then stop. Else continue with step 3.
- **step 3:** compute the step length α^k.

- **step 4:** compute $\mathbf{x}^{k+1} = \mathbf{x}^k + \alpha^k \mathbf{d}^k$. Increment k by one ($k = k + 1$) and go back to step 1.

Notice that this method requires $H\left(\mathbf{x}^k\right)$ to be non-singular at each iteration step. Also, in general it is not guaranteed that $f\left(\mathbf{x}^{k+1}\right) \leqslant f\left(\mathbf{x}^k\right)$. Lastly, a suitable α^k may be computed in step 3 by finding the local minimum of the auxiliary scalar function $\psi(\alpha) = f\left(\mathbf{x}^k + \alpha \mathbf{d}^k\right)$.

To use the aforementioned optimization method, we must derive a suitable real-valued function from the equations in (5.10), whose local minimum points coincide with the solutions of (5.10). The equations are first rewritten as:

$$\begin{cases} f_1(\theta_1,\theta_2) = cos(\alpha_2 - \theta_2) - \theta_2 sin(\alpha_2 - \theta_2) - cos(\alpha_1 - \theta_1) + \theta_1 sin(\alpha_1 - \theta_1) = 0 \\ f_2(\theta_1,\theta_2) \ = \ \theta_2 cos(\alpha_2 - \theta_2) + sin(\alpha_2 - \theta_2) + \theta_1 cos(\alpha_1 - \theta_1) + sin(\alpha_1 - \theta_1) - \dfrac{d}{ra} = 0 \end{cases} \tag{5.14}$$

Then, if we square both the right-hand terms in (5.14) and take the sum of the resulting expressions, we get the desired non-negative function:

$$f_1^2(\theta_1,\theta_2) + f_2^2(\theta_1,\theta_2) = 0 \tag{5.15}$$

It turns out that (5.15) possesses several local minima. Therefore, the initial guess must be chosen carefully in order to converge to the desired solution. We choose $\boldsymbol{\theta}^0 = \{\theta_{1,0}\ \theta_{2,0}\}'$ as the centroid of the range of feasible values for the solution. From geometrical considerations, the feasible values for $\varphi = (\alpha - \theta)$ are:

$$0 < (\alpha - \theta) < \frac{\pi}{2} \tag{5.16}$$

which may be rewritten in terms of θ:

$$\alpha - \frac{\pi}{2} < \theta < \alpha \tag{5.17}$$

Since (5.17) holds for both θ_1 and θ_2, we get the following expressions for the initial guess:

$$\begin{cases} \theta_{1,0} = \alpha_1 - \dfrac{\pi}{4} \\ \theta_{2,0} = \alpha_2 - \dfrac{\pi}{4} \end{cases} \tag{5.18}$$

From numerical simulations and tests on the real device, we found that the number of required iterations was reduced when the first 3 iterations were performed with the *Steepest Descent* method [98]. Also, we slightly modified the computation of α^k to constrain $\mathbf{x}^{k+1}$ inside the feasible range (5.16).

Fig. 5.9 shows how the algorithm solves a typical forward kinematics problem. The contour lines of the function $f_1^2 + f_2^2$ are portrayed together with a red broken line representing the iteration steps. The red rectangle represents the range of acceptable values for the solution. Notice that the initial guess coincides with the centroid of this rectangle.

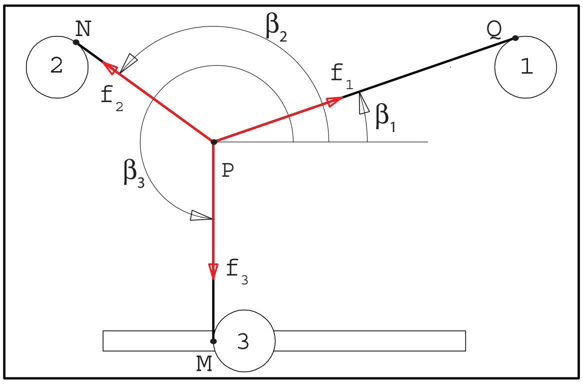

Figure 5.10: Reference points for the reverse kinematics and tension forces on each cable

Once θ_1 and θ_2 are known, the position of the end effector in the base frame can be computed[6] (Fig. 5.8):

$$P = \mathbf{x}_{M1} + ra\left(\begin{Bmatrix} -sin\varphi_1 \\ cos\varphi_1 \end{Bmatrix} - \theta_1 \begin{Bmatrix} cos\varphi_1 \\ sin\varphi_1 \end{Bmatrix}\right) \tag{5.19}$$

where $\mathbf{x}_{M1}$ is the position vector of the centre of pulley 1 w.r.t. the base frame.

5.6.2 Compensation of cable elongation

In this Section, we will briefly describe the model utilized to compensate cable elasticity. In this simple algorithm, we assume an ideal linear elastic constitutive law to model the cable[7]. Also, we assume that the cross-section of the cable does not vary under different loads, and that the unreeled cable is the only deformed portion of the cable[8]. The Hooke's law describes the correlation between strain and stress:

$$\sigma = \frac{f}{A} E\varepsilon = E \ \ln\left(\frac{l}{l_0}\right) \tag{5.20}$$

where:

- $E \approx 7000MPa$ is the Young's modulus of the cable, as it was estimated empirically.
- $A = \pi/4 \ d_0^2 \approx 0.28mm^2$ is the cable cross-section (for a diameter $d_0 \approx 0.6mm$).
- $f[N]$ is the cable tension.
- l_0 and l are the undeformed cable length and the actual cable length, respectively.

---

[6] In the base reference frame, the x axis is parallel to the largest side of the table, and directed towards the right side of the patient, whereas the y axis is parallel to the shortest side of the table and directed towards the fixed pulley-blocks.

[7] Actually, the Dyneema fiber shows a viscoelastic behavior, with the strain being a function of time. However, as far as kinematic computations are concerned, we adopted an ideal elastic model to reduce the computational load on the controller.

[8] This is equivalent to state that the friction forces between the cable and the pulley are sufficient to inhibit relative motions between the reeled cable and the pulley surface. Indeed, empirical tests showed that this assumption is not completely true.

From (5.20), one can derive the actual cable length:

$$l = l_0 \ \mathrm{e}^{\frac{f}{EA}} \tag{5.21}$$

Therefore, by substituting $\left(ra\ \theta\ \mathrm{e}^{f/EA}\right)$ to $(ra\ \theta)$ in (5.4), we get:

$$^{t}P = \left\{ \begin{array}{c} ra \\ ra\ \theta\ \mathrm{e}^{f/EA} \end{array} \right\} \tag{5.22}$$

Thus, by including this modification in the procedure outlined in Section 5.6.1, corresponding relations are derived which take into account the cable elasticity.

5.6.3 Reverse kinematics & calibration

The calibration process of Sophia-3 comprises two steps. In the first step, the end-effector is positioned in a known reference point $\{x_{cal}, y_{cal}\}'$. In this point, the right offsets are assigned to the encoder inputs, i.e., those allowing to derive α by simply applying (5.3).

Let us first consider pulley 1. For a known reference point P, the magnitude $\overline{PQ}$ (Fig: 5.10) and the angle φ_1 are computed. Additionally, since motor 1 is commanded in torque mode (a constant torque is commanded in this phase, which corresponds to $f_{\min} = 5N$), the tension f_1 is known as well[9]. $\left\|\overline{PQ}\right\|$ is written as:

$$\left\|\overline{PQ}\right\| = ra\ \theta_{def,1} \tag{5.23}$$

where $\theta_{def,1} = l_1/ra$ is the wrapping angle of the stretched cable 1 (Section 5.6.2). The corresponding cable length when $f_1 = 0$ is $l_{0,1} = ra\ \theta_{0,1}$, hence, from (5.21) we get:

$$\theta_{0,1} = \frac{\|\overline{PQ}\|/ra}{\mathrm{e}^{\frac{f_1}{EA}}} \tag{5.24}$$

Thus, the value to be assigned to the encoder 1 at the calibration point is:

$$\alpha_{0,1} = \varphi_{0,1} + \theta_{0,1} \tag{5.25}$$

The same approach is then applied to motor 2 in order to get $\alpha_{0,2}$.

The second calibration step is required for motor 3 (moving pulley-block). Once motor 1 and motor 2 have been calibrated, the user must release the joystick, the tensions in the upper wires are progressively incremented up to a certain value and, once the static equilibrium has been reached (in general, in a new point of the workspace), the tension f_3 is computed through the following expressions (Fig. 5.10):

$$f_3 \left\{ \begin{array}{c} cos\beta_3 \\ sin\beta_3 \end{array} \right\} = -\left(f_1 \left\{ \begin{array}{c} cos\beta_1 \\ sin\beta_1 \end{array} \right\} + f_2 \left\{ \begin{array}{c} cos\beta_2 \\ sin\beta_2 \end{array} \right\} \right) \tag{5.26}$$

where we assume that the table lays in the horizontal position (i.e. $\delta = 0°$) and friction between the end-effector and the table surface is negligible. Notice that, in nominal conditions,

---

[9] In principle, one should use the feedback from the current monitor instead of the commanded torque to compute the wire tension. However, this feedback requires filtration, thus introducing delays.

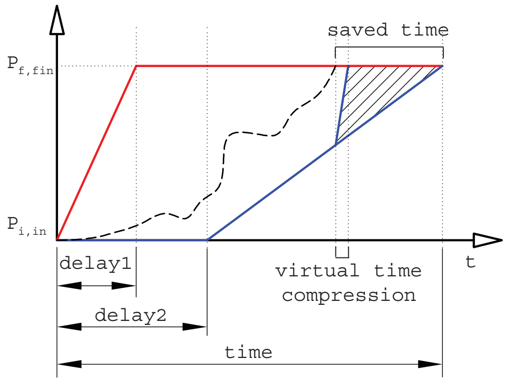

Figure 5.11: Patient's trajectory (dashed line) and trajectories of P_f and P_i (red/blue solid lines) as projected along one of the axes of the reference frame

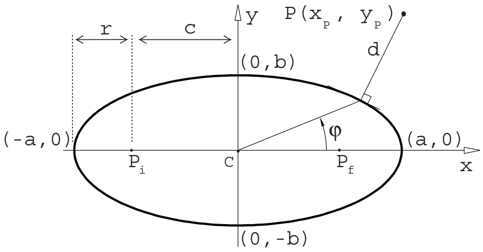

Figure 5.12: Parameters that define the ellipse

$cos\beta_3 = 0$ e $sin\beta_3 = -1$. f_1 e f_2 are computed by the torque commands and β_1, β_2 are derived from the forward kinematics performed with pulley 1 and pulley 2.

Recall that the lower cable is connected in series to an extension spring (Section 4.6.2), the total length $\left\|\overline{PM}\right\|$ may be written as:

$$\left\|\overline{PM}\right\| = ra\ \theta_{def,3} + L_0 + \frac{f_3}{k} \tag{5.27}$$

where k is the spring constant and L_0 is the spring length in no load conditions. Since $\theta_{def,3}/\theta_{0,3} = \mathrm{e}^{\frac{f_3}{EA}}$, we get the following expression of the undeformed wrapping angle:

$$\theta_{0,3} = \frac{\left\|\overline{PM}\right\| - L_0 - f_3/k}{ra\ \mathrm{e}^{\frac{f_3}{EA}}} \tag{5.28}$$

which allows to compute the value to be assigned to the encoder 3:

$$\alpha_{0,3} = \varphi_{0,3} + \vartheta_{0,3} \tag{5.29}$$

In (5.28), $\left\|\overline{PM}\right\|$ is known from the forward kinematics performed with pulleys 1 and 2, f_3 is estimated through (5.26) and the remaining terms are known constant parameters.

5.6.4 Active-assistive control

As a haptic display, *Sophia-3* is capable of reproducing real and virtual environments by exerting a variable mechanical impedance to the user's hand. The mechanical impedance perceived by the patient at the end-effector is modified by controlling the force **F** exerted by the cables. This force is computed in real-time by the host PC, which constantly monitor the state of the therapy and the patient's performance. Adaptive control algorithms that define how to compute **F** according to the specific exercise and according to the patient's performances have been recently developed and experimentally tested at the DIMEG-Robotics Research Group [74]. However, they have not been implemented in the Sophia-3 prototype yet.

At this time, a simple *impedance controller* has been implemented in the prototype, which will be described in the following. The therapeutic exercise consists in repeating *point-to-point* reaching tasks along straight line segments, wherein the start/end points are the vertexes of a regular polygon. Whenever a goal point is reached, the current goal point becomes the new starting point, and the new goal point is set to the farthest extreme of one of the adjacent sides of the polygon. A GUI will run on a host PC, allowing the therapists to set the parameters that specifies the exercise. Also, the patient can observe the current movements of the end-effector reproduced on a virtual environment (Fig. 5.6).

The main objective is to let the patient free while performing the motion task. Therefore, the control plays an active role only when the patient - due to motor impairments - is not capable of completing the task, performs *jerky* motions or moves away from the nominal trajectory. This approach is usually referred to as an *active-assistive* control, an represents one of the possible ways of implementing the *assist-as-needed* paradigm [99].

In this application, a suitable force field is realized, which takes the form of an *elliptical force tunnel* whose shape varies according to the elapsed time and according to the patient's performances. As the patient moves the end-effector inside the force-tunnel, no external forces are generated at the end-effector, except those required to compensate gravity. The boundary of the virtual tunnel acts as an *elastic virtual wall*: as soon as the patient exits the virtual tunnel, he/she senses a force whose magnitude is proportional to the distance between the elliptical wall and the current position of the end-effector, and whose direction is orthogonal to the boundary. Additionally, if the end-effector remains still for a certain amount of time, the patient perceives a force that is directed towards the goal point. As it will be clear in the following, this force is generated by the back focus of the ellipse moving towards the front focus.

The *foci* of the ellipse that define the moving virtual tunnel are named P_i and P_f (Fig. 5.12). At the beginning of the current reaching task, both P_i and P_f coincide with the current location of the end-effector (i.e., the ellipse is actually a circumference). Then, P_f moves towards the target point with a constant speed $\mathbf{v}_{Pf}$, and reaches the target point in the predefined time interval *delay1*. After a time interval denoted as *delay2*, also P_i starts moving towards the target point at a constant speed $\mathbf{v}_{Pi}$, and reaches the latter when the elapsed time is equal to the parameter *time* (again, the ellipse is a circumference). Fig. 5.11 represents qualitatively the trajectories of P_f and P_i as projected along the major axis of the ellipse.

Thus, the parameters that must be imposed by the therapist before each reaching task are the following;

- *Starting point:* This parameter coincides with the current position of the end-effector (5.19).
- *Target point:* This parameter is the end-point of the current task.
- *Wall stiffness:* This parameter changes the behavior of the virtual elastic wall.
- *time, delay1, delay2:* These are the temporal parameters defined in Fig. 5.11.
- *r:* This is the radius of the starting/end circumferences, which is also related to the shape of the moving ellipse. Indeed, it was chosen as an independent parameter since it has a more direct meaning for a therapist than the parameters commonly used to define the equation of an ellipse (e.g., the ellipse eccentricity).

Notice that the shape of the ellipse is completely known once the current foci P_i and P_f have been computed, and the parameter r has been defined. Indeed, the positions of the foci defines c (i.e., half of the focal length). Then, from r and c we may compute $a = r + c$ and $b = \sqrt{a^2 - c^2}$, which define the axes of the ellipse (Fig. 5.12).

Finally, the velocities of P_f and P_i are computed as:

$$\mathbf{v}_{Pf} = \frac{P_{f,fin} - P_{i,in}}{delay_1} \tag{5.30a}$$

$$\mathbf{v}_{Pi} = \frac{P_{f,fin} - P_{i,in}}{time - delay_2} \tag{5.30b}$$

It may be that the patient reaches the goal point before the predefined time interval denoted as $time$ (Fig. 5.11). In this case, the velocity of point P_i should be increased to speed up the setup of the next reaching task. To this aim, the trajectories of P_f and P_i have been planned on a virtual time basis, as described in (5.32). The *virtual time* et can be arbitrarily deformed according to the needs of the therapy. Let T1 be the timer object initialized at the beginning of each reaching task, and let $\mathrm{TM\_ET}\,(x)$ be the embedded function that reads the elapsed time from a timer object x. Then, the virtual time is defined as:

$$\mathrm{et} = \left(1000\ \mathrm{M}\right)\ \mathrm{TM\_ET}\left(\mathrm{T1}\right) \quad [s] \tag{5.31}$$

where M is the time distortion coefficient. Normally, the virtual time and the actual elapsed time coincide (i.e., M = 1). However, if the patient reaches the target point before the expected time interval, the value of M is increased, thereby P_i moves to the goal position more rapidly. Thus, the trajectory planning is stated as follows:

$$P_f\left(et\right) = \begin{cases} P_{i,in} + \mathbf{v}_{Pf}\ et & if\ \left(et < delay_1\right) \\ P_{f,fin} & otherwise \end{cases} \tag{5.32a}$$

$$P_i\left(et\right) = \begin{cases} P_{i,in} & if\ \left(et < delay_2\right) \\ P_{i,in} + \mathbf{v}_{Pi}\left(et - delay_2\right) & otherwise \end{cases} \tag{5.32b}$$

To model the elastic virtual wall, a closed form equation that computes the distance of an arbitrary point from the ellipse has been developed. The parametric equations of the *canonical ellipse* are:

$$\begin{cases} x = a\ cos\varphi \\ y = b\ sin\varphi \end{cases} \tag{5.33}$$

Hence, the distance between a given point $P(x_P, y_P)$ and a generic point belonging to the ellipse is:

$$d\left(\varphi\right) = \sqrt{\left(a\ cos\varphi - x_P\right)^2 + \left(b\ sin\varphi - y_P\right)^2} \tag{5.34}$$

Clearly, the distance between P and the ellipse may be computed by evaluating (5.34) for the φ corresponding to the closest point of the ellipse, i.e., the *local minimum point* of the

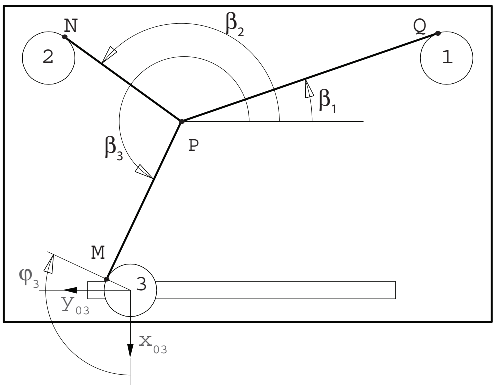

Figure 5.13: Angles defining the structure matrix

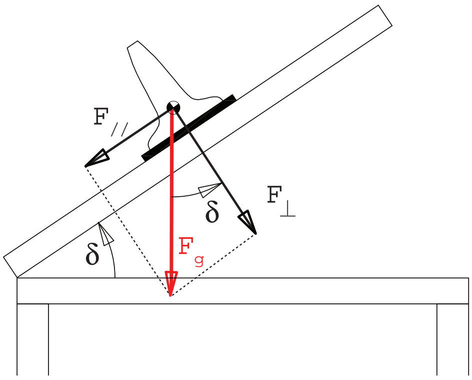

Figure 5.14: Decomposition of the weight of the end-effector

function $d(\varphi)$. The latter coincides with the local minimum of $d^2(\varphi)$, thereby we compute the derivative of this function and set it to zero:

$$\frac{d}{d\varphi}\left[d^2(\varphi)\right] = 2ax_P\, sin\varphi - 2by_P\, cos\varphi = 0 \tag{5.35}$$

After the following substitutions: $A = 2ax_P$, $B = -2by_P$ and after using the sum-difference formulas, (5.35) can be rewritten as:

$$cos(\varphi - \gamma) = 0 \tag{5.36}$$

where:

$$\gamma = atan2\left(\frac{A}{\sqrt{A^2+B^2}}, \frac{B}{\sqrt{A^2+B^2}}\right) \tag{5.37}$$

therefore, we get two values for φ:

$$\varphi_1 = \gamma + \frac{\pi}{2}; \quad \varphi_2 = \gamma + \frac{3\pi}{2} \tag{5.38}$$

The actual solution is the one leading to the minimum distance d, as computed through (5.34).

5.6.5 Wire tension distribution

Recall that the static equilibrium of the end effector may be expressed by the force-closure equation (2.2):

$$\mathbf{F} = \mathbf{A}\mathbf{f} \tag{5.39}$$

where, in the case of the Sophia-3 prototype, $\mathbf{A} \in \mathbb{R}^{2\times 3}$. Following the notation in Fig. 5.10, the structure matrix is defined as:

$$\mathbf{A} = \begin{bmatrix} cos\beta_1 & cos\beta_2 & cos\beta_3 \\ sin\beta_1 & sin\beta_2 & sin\beta_3 \end{bmatrix} \tag{5.40}$$

Notice that the angles in (5.40) may be easily computed from the corresponding φ (Fig. 5.8 and Fig. 5.14):

$$\beta_1 = \varphi_1; \quad \beta_2 = \pi - \varphi_2; \quad \beta_3 = 2\pi - \varphi_3; \tag{5.41}$$

Thus, if the end-effector does not lay on a singular position (i.e., $\operatorname{rank}(\mathbf{A}) = 2$), there are ∞^1 solutions. However, in order for a solution $\mathbf{f}$ to be feasible, it must be $\mathbf{f}(i) \in [f_{\min}, f_{\max}]$ $\forall\ i = 1, 2, 3$. Among the feasible solutions, we want to find the optimal one, i.e., the one that minimize the dissipated power. Recall that the power dissipated under quasi-static conditions is yielded by (2.4):

$$P = \sum_{i=1}^{n} c_i\, f_i^2 \tag{5.42}$$

where the constant c_i depends on the pulley-block characteristics. Assuming that the pulley-blocks are identical[10], the solution that minimized P is the minimum norm solution:

$$\min\left(P_{diss}\right) \Leftrightarrow \min\left(\, \| f \| \,\right) \tag{5.43}$$

For any CRPM, a theorem presented in a previous work [37] states the existence and uniqueness of $\hat{\mathbf{f}}$, as long as the end-effector lays inside the workspace. Also, an explicit expression for the solution was derived in [37]:

$$\begin{cases} \hat{\mathbf{f}} = \tilde{\mathbf{f}}_{\mathbf{i}} + \beta \mathbf{h} \\ \beta = \max\limits_{t=1,2,3} \left(\frac{f_{\min} - \tilde{\mathbf{f}}_{\mathbf{i}}(t)}{\mathbf{h}(t)} \right) \end{cases} \tag{5.44}$$

where $\tilde{\mathbf{f}}_{\mathbf{i}}$ is a solution of equation (5.39) having the i-th component arbitrarily set to zero (i.e. $\tilde{\mathbf{f}}_{\mathbf{i}}(i) = 0$), and $\mathbf{h}$ is the strictly-positive kernel vector of $\boldsymbol{A}$:

$$\mathbf{h} = \begin{pmatrix} \sin(\beta_3 - \beta_2) \\ \sin(\beta_1 - \beta_3) \\ \sin(\beta_2 - \beta_1) \end{pmatrix} = \begin{pmatrix} \sin \chi_2 \\ \sin \chi_3 \\ \sin \chi_1 \end{pmatrix} \tag{5.45}$$

where χ_i are defined as in Section 3.2.1.

Since (5.44) does not account for the upper bound $f_{\max}$, a method must be developed to *scale* the cable tensions vector $\mathbf{f}$ if one of its components exceeds $f_{\max}$. Given the linearity of system (5.39), by scaling vector $\mathbf{f}$ we will get an actual operational force with the same direction as $\mathbf{F}$ and a magnitude reduced by the scaling factor. The scaling factor is chosen so that the tension of the most stressed cable is kept equal to $f_{\max}$. Without this correction, the saturation of one or more actuators may lead to significant differences between the required force $\mathbf{F}$ and the actual force (Section 5.7).

In (5.39), $\mathbf{F}$ is the resultant vector of the forces applied by the end-effector. Under the pseudo-static hypothesis and assuming that friction is negligible, this force balances the one exerted by the patient's hand and the action of gravity. The latter component is nonzero when the orientation of the table (as measured through the potentiometer) is nonzero. Specifically, since friction has been neglected, only the projection of the end-effector weight on the plane of motion must be considered (Fig. 5.14):

$$\mathbf{F}_{//} = m_{EE}\, \mathbf{g}\, sin\delta \tag{5.46}$$

where m_{EE} is the mass of the end-effector, g is the gravitational acceleration and δ is the orientation of the table w.r.t a horizontal plane. The vectorial sum of $\mathbf{F}$ and $\mathbf{F}_{//}$ yields $\mathbf{F}_w$, i.e., the force exerted by the virtual wall on the patient's hand.

---

[10] Rigorously speaking, this is not the case of Sophia-3. Anyway, we still regard the minimum norm solution as the most suitable (feasible) solution of (5.39).

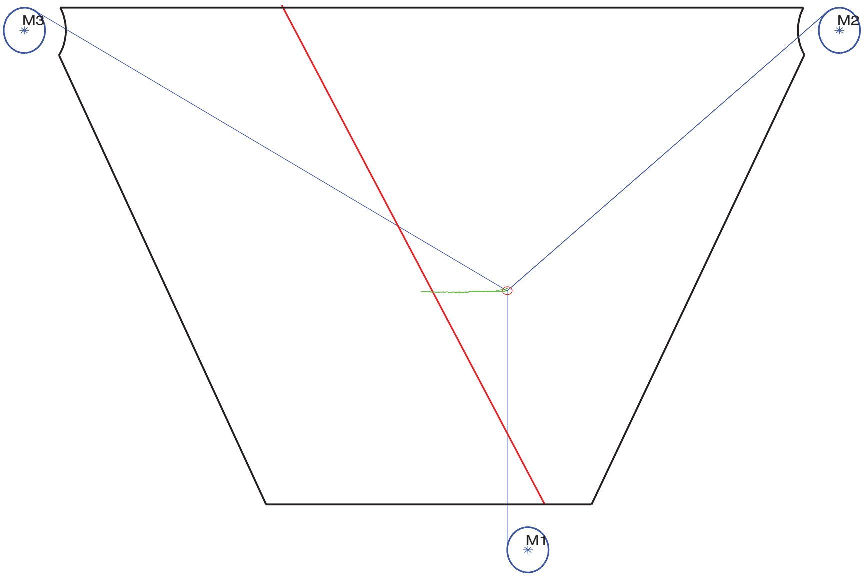

Figure 5.15: Path followed by the subject during the test

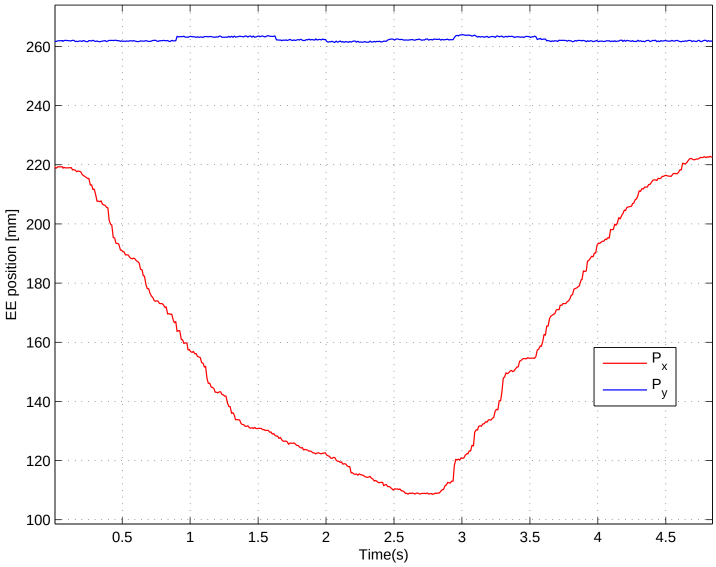

Figure 5.16: Projections of the trajectory along the coordinate axes

5.7 First Experimental results

In this section we illustrate a first experimental test which was carried out with the $\mu - RMC$ controller and the CANopen-based control architecture. A straight-line virtual wall was implemented inside the workspace, and the user was asked to perform a point-to-point reaching task along a straight-line segment, which was partially inside the virtual wall.

Fig. 5.15 shows the path followed by the user (green curve), as it was estimated by the forward kinematics algorithm. The extremities of the straight line segment representing the nominal path were both indicated on the surface of the wooden table (total length $100mm$). In the reference frame (whose origin coincides with the centroid of the trapezium and whose x axis is horizontal and oriented to the right of the user) their coordinates were: $x_1 = \{-15,\ 0\}' mm$ and $x_2 = \{85,\ 0\}' mm$.

The boundary of the virtual wall is indicated by the red solid line shown in Fig. 5.15, which splits the workspace into two regions. The virtual wall was located in the left region. The line forms an angle $\alpha = 2\pi/3$ with the x axis and passes through the origin of the reference frame. Thus, the user was supposed to enter the wall for approximately $15mm$. The wall was perfectly elastic, with $k_{\text{wall}} = 10N/mm$. This value was chosen because it guarantees stable interactions.

Fig. 5.16 shows the projections of the actual trajectory along the axes of the reference frame. It took the user $\Delta t \approx 4.8s$ to complete the movement, with an average velocity $v_{\text{avg}} \approx 41.3mms^{-1}$.

Fig. 5.17 shows the tensions carried by each cable (solid lines), as they were estimated offline, based on the current monitor. Tensions have been normalized to the maximum allowable value ($f_{\max} = 100N$). A minimum tension $f_{\min} = 5N$ was also imposed. The corresponding operational forces are portrayed in Fig. 5.18 (solid red lines) in polar coordinates. Again, the values have been normalized to $f_{\max}$.

As the end-effector approaches the virtual wall while moving on the horizontal path, positive cable tensions are computed to yield a null operational force $\mathbf{F} = \mathbf{0}$ (Fig. 5.18, upper diagram). As soon as the end-effector enters the wall, an elastic reaction force is generated, which is orthogonal to the wall boundary (i.e., $\varphi = \pi/6$). Beyond a certain value of x_{EE}, the required force causes the most loaded cable f_2 to reach the upper constraint $f_{\max}$ (Fig. 5.17). A further increment in the magnitude of $\mathbf{F}$ would lead to the saturation of the same cable, and the actual vector of cable tensions would therefore differ in one component from the computed one, which satisfies (5.39). This, in general, will result in an exerted force that differs from the required one *in both magnitude and direction*.

Fig. 5.18 clearly shows that after saturation of cable 2, not only the magnitude $\|\mathbf{F}_{sat}\|$ is less than the required one $\|\mathbf{F}_{id}\|$, but also the actual force is not directed along $\varphi_{id} = \pi/6$. Indeed, the exerted force shows an unwanted increase in the x component at the expense of the y component. The situation would have been even worse if a second cable saturated.

To overcome this issue, all tensions may be scaled so as to force the maximum tension $f_{\max}$ in the critical cable. Due to the linearity of (5.39), the actual force vector will be one having the same orientation as the nominal force, and a magnitude reduced by the scaling factor. Fig. 5.17 shows the tensions corresponding to the ideal force $\mathbf{F}_{id}$ in dashed lines. The peak value of the ideal f_2 is approximately $\approx 2.2\ f_{\max}$, thereby exceeding the upper limit of the y axis. These tensions were computed offline based on the recorded position data and on the characteristics of the virtual wall. Therefore, they do not take into account the upper bound $f_{\max}$. Solid lines represent the actual tensions in the cables, and they correspond to the force $\mathbf{F}$ shown in Fig. 5.18 (red line). It can be noticed that, as f_2 reaches f_{max}, all the tensions are scaled down, so that the critical cable f_2 is kept inside the feasible range. This, in turn, reduces the detrimental effect on the exerted force. Indeed, in Fig. 5.18 (bottom plot) the angles φ_{id} and φ are ideally coincident (differences are due to disturbances in the current signals which are reflected in the force computation). Also, the magnitude of the exerted

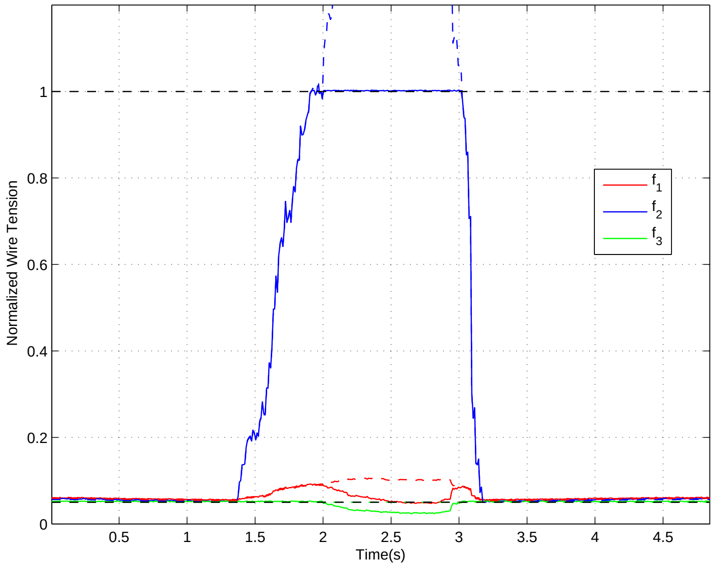

Figure 5.17: Tensions in the cables as estimated from the current monitor. Dashed lines indicate the tensions corresponding to $\mathbf{F_{id}}$

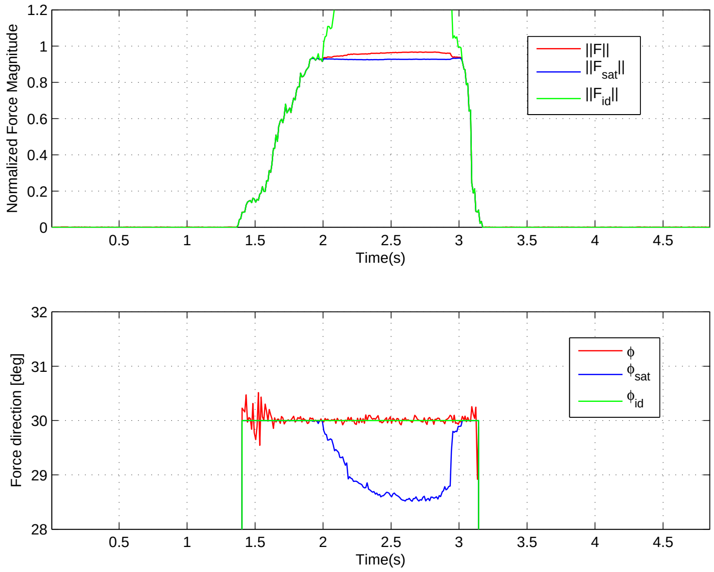

Figure 5.18: Operational force in polar coordinates: actual exerted force ($\mathbf{F}$), virtual wall force ($\mathbf{F_{id}}$) and force caused by the uncontrolled saturation of f_2 ($\mathbf{F_{sat}}$)

force is closer to the ideal one than in the previous case (top plot).

Such a behavior is clearly more suitable for a haptic device, providing the user with a more natural force feedback. The exerted force is still able to correct the patient's trajectory, even though its magnitude is lower than the computed one.

5.8 Conclusion

This chapter presented the software and the low-level control algorithms of Sophia-3, together with some experimental results. This early version of the prototype showed some limitations in early experimental tests, therefore, a new control design was developed (see Section 4.12).

The new controller architecture was developed in a centralized fashion: all the I/O signals are directly fed to the controller (industrial PC), with the exception of the encoders, whose signals are redirected from the drives to the main controller.

The new hardware configuration has already been discussed in Section 4.12. The software architecture is very similar to the previous one and, therefore, is not presented here. Experimental tests with the new hardware will start in the near future.

Conclusion

The main contribution of this thesis consists in the introduction of a new design methodology for cable-driven systems. This methodology led to the definition of a new subclass of devices, called *Adaptive cable-driven devices*. To validate the new methodology, simulated numerical analysis was carried out, and a prototype was designed, developed and tested.

A set of local, non-dimensional and configuration-dependent indices was presented first, to quantitatively define the relevant performances of a cable-driven system for any given pose of the end-effector. Thanks to this tool of analysis, it was proved that the capabilities of a device, as seen from the end-effector, are heavily dependent on the relative configuration of the cables w.r.t the end-effector. For a given traditional design (i.e. fixed attaching points to the ground and fixed shape of the end-effector), this configuration is uniquely determined by the pose of the end-effector. Therefore, once the number of cables has been decided, choosing the most efficient layout becomes a major issue, and the proposed set of indices can help the designer in defining a suitable solution in the early steps of the design process. To validate this hypothesis, a simple comparative analysis was presented in Chapter 2, where the performances of three existing prototypes were compared based on the proposed indices. In this analysis, only geometrical considerations and few inertial parameters were required.

Thanks to the insight provided by the performance indices, a new systematic design methodology was proposed, which takes advantage of the introduction of actively controlled moving pulley blocks to obtain *well-tailored* design solutions. These additional DOFs are employed to decouple the cable disposition from the pose of the end-effector, with the aim of keeping the cables close to the optimal configuration, i.e., the one yielding the highest value of a specific performance index. In Chapter 3, the effectiveness of this method was verified by solving simple case-studies with both the traditional and the new design method. The *Fully-adaptive* designs proved to be well-tailored and compact, even though design complexity increased.

The *Semi-adaptive* designs were defined as those devices wherein the number of additional DOFs does not allow to achieve a complete decoupling between the pose of the end-effector and the configuration of the cables. In Chapter 3, the presented case-studies showed that these devices may be a good compromise between ease of design and compactness, and can therefore represent a suitable solution in many practical applications.

To validate this assumption empirically, the first prototype of Semi-adaptive device, called *Sophia-3*, was designed and developed . This device was conceived as a cost-effective planar rehabilitation device to be employed in the decentralized health-care treatment of chronic post-stroke patients. Thus, cost-effectiveness, ease of use and transportability are the key points of the prototype. The device employs three active cables. However, thanks to the introduction of a moving pulley-block, Sophia-3 showed comparable force capabilities as those of a previous prototype, Sophia-4, which employed a traditional design with 4 active cables.

Chapter 4 described the mechanical and electrical design of Sophia-3, focusing on the improvements introduced w.r.t. the previous prototype, such as: the variable inclination of the working plane, the elimination of the fixed attachment points at the base and the introduction of a moving pulley-block. Chapter 5 illustrated the control architecture of Sophia-3 and the main control algorithms, and reported the first results from experimental tests carried out with the device.

In the near future, the new control architecture of Sophia-3 will be completed and the connection between the machine and the therapy software running in the host PC will be set up. Then, new experimental tests will be carried out on healthy subjects to validate the safety and the functionality of the machine.

From the theoretical point of view, the studies on the *Adaptive cable-driven systems* may be further extended, for example by studying the effects of introducing some levels of adaptiveness also in the end-effector. Also, the introduction of passive cables and springs may be an effective choice to reduce design complexity and costs, especially when the dynamic performances of the device are not a major concern.

Appendix A

Appendix

A.1 Derivation of $i_{F,CRIT}$ (2-DOF, 3-cable, point-mass device)

Let consider the class of devices whose cable attachment points lie on the vertices of an equilateral triangle, and let R and r be defined as in Section 3.2.1. Here, we want to determine $\mathbf{P}_{CRIT}$, i.e., the point of the circumference of radius r with the minimum value of i_F, and the corresponding value $i_{F,CRIT}$.

Given the symmetry of $i_F(\mathbf{P})$, three symmetrically arranged critical points have to be expected: therefore, we may restrict the minimization to the portion of the circumference belonging to a specific region, say, the lower region in Fig.3.2(a). Here, i_F is a function of χ_1 only, and to find the minimum of i_F means to find the maximum of χ_1 or, equivalently, the minimum of $\cos\chi_1$.

Let $\mathbf{P}_1, \mathbf{P}_2$ be defined as in Fig. 3.2(a). We first derive $\mathbf{v}_1$ and $\mathbf{v}_2$, the unit vectors of cable 1 and 2:

$$\begin{gathered}\mathbf{P}_1 = R\left\{\cos\theta_1, \sin\theta_1, 0\right\}^T, \quad \mathbf{P}_2 = R\left\{\cos\theta_2, \sin\theta_2, 0\right\}^T, \\ \mathbf{P}_{CRIT} = R\left\{\cos\theta, \sin\theta, 0\right\}^T \\ \mathbf{v}_1 = \frac{\mathbf{P}_{CRIT}\mathbf{P}_1}{\left\|\mathbf{P}_{CRIT}\mathbf{P}_1\right\|}, \quad \mathbf{v}_2 = \frac{\mathbf{P}_{CRIT}\mathbf{P}_2}{\left\|\mathbf{P}_{CRIT}\mathbf{P}_2\right\|}\end{gathered} \tag{A.1}$$

Then, we compute the scalar product $\mathbf{v}_1 \cdot \mathbf{v}_2$, and set its derivative to 0, in order to find θ:

$$\begin{gathered}\frac{d\cos\chi_1}{d\theta} = \\ = \frac{4rR^2(r^2 - R^2)\sin\left(\frac{\theta_1-\theta_2}{2}\right)^2 \sin\left(\theta - \frac{\theta_1+\theta_2}{2}\right)\left(-R\cos\left(\frac{\theta_1-\theta_2}{2}\right) + r\cos\left(\theta - \frac{\theta_1+\theta_2}{2}\right)\right)}{\left(r^2 + R^2 - 2rR\cos\left(\theta - \theta_1\right)\right)^{3/2}\left(r^2 + R^2 - 2rR\cos\left(\theta - \theta_2\right)\right)^{3/2}} = 0\end{gathered} \tag{A.2}$$

for $\theta_1 = 7\pi/6$, $\theta_2 = 11\pi/6$, $\theta \in [7\pi/6, 11\pi/6]$ and $(r/R) \leqslant 1/2$, the solution is unique and gives: $\theta = 3\pi/2$.

In order to derive $\sin\chi_{CRIT}$, the previous value of θ is introduced inside the expressions of $\mathbf{v}_1$ and $\mathbf{v}_2$, and the magnitude of their cross product is computed:

$$\sin\chi_{CRIT} = \mathbf{v}_1 \times \mathbf{v}_2 \cdot \mathbf{k} = \frac{\sqrt{3}}{2}\frac{\left(1 - 2\left(r/R\right)\right)}{\left(\left(r/R\right)^2 - \left(r/R\right) + 1\right)} \tag{A.3}$$

where $\mathbf{k} = \{0, 0, 1\}^T$. Finally, by substituting (A.3) into (3.5), the following expression is obtained:

$$i_{F,CRIT} = i_{F,\max}\frac{1-2(r/R)}{(r/R)^2-(r/R)+1} \qquad (r/R) \in \left[0, \tfrac{1}{2}\right] \tag{A.4}$$

where $i_{F,\max}$ is defined as in (3.6). Therefore, for a given F_{REQ}, if $i_{F,CRIT} \geqslant F_{REQ}$, then the inequality $i_F\left(\mathbf{P}\right) \geqslant F_{REQ}$ holds for all the points belonging to the circumference of radius r. In addition, since (A.4) is a monotonically decreasing function, the entire circle of radius r must posses acceptable values of i_F.

Bibliography

[1] R. Verhoeven, "Analysis of the workspace of tendon-based stewart platforms," Ph.D. dissertation, Universität Duisburg-Essen, July 29 2004.

[2] S. Behzadipour, R. Dekker, A. Khajepour, and E. Chan, "DeltaBot: A new cable-based ultra high speed robots," in *Proc. of the ASME International Mechanical Engineering Congress & Exposition IMECE2003*, vol. 2003, no. 37130. ASME, 2003, pp. 533–537.

[3] Hitachi, "Hitachi plant technologies, ltd. 2006," http://www.hitachi-pt.com/products/mechatronics/crane1/index.html, 2010.

[4] K. Maeda, S. Tadokoro, T. Takamori, M. Hiller, and R. Verhoeven, "On design of a redundant wire-driven parallel robot WARP manipulator," in *Proc. of the IEEE International Conference on Robotics and Automation ICRA1999*, vol. 2, 1999, pp. 895–900.

[5] D. A. Lawrence, "Stability and transparency in bilateral teleoperation," *IEEE Transactions on Robotics and Automation*, vol. 9, no. 5, pp. 624 –637, oct 1993.

[6] S. Kim, S. Hasegawa, Y. Koike, and M. Sato, "Tension based 7-DOF force feedback device: SPIDAR-G," in *Proc. of the IEEE Virtual Reality, 2002*, 24-28 March 2002, pp. 283 –284.

[7] G. Boschetti, G. Rosati, and A. Rossi, "A haptic system for robotic assisted spine surgery," in *Proc. of the IEEE Conference on Control Applications, CCA2005*, Aug. 2005, pp. 19–24.

[8] P. Gallina, G. Rosati, and A. Rossi, "3-d.o.f. wire driven planar haptic interface," *Journal of Intelligent and Robotic Systems*, vol. 32, no. 1, pp. 23–36, 2001.

[9] J. Pusey, A. Fattah, S. Agrawal, and E. Messina, "Design and workspace analysis of a 6-6 cable-suspended parallel robot," *Mechanism and Machine Theory*, vol. 39, no. 7, pp. 761 – 778, 2004.

[10] S.-R. Oh, K. Mankala, S. Agrawal, and J. Albus, "Dynamic modeling and robust controller design of a two-stage parallel cable robot," in *Proc of the IEEE International Conference on Robotics and Automation, 2004, ICRA '04.*, vol. 4, April 26 - May 1 2004, pp. 3678 – 3683.

[11] J. Albus, R. Bostelman, and N. Dagalakis, "NIST ROBOCRANE," *Journal of Robotic Systems*, vol. 10, no. 5, pp. 709 – 724, 1993.

[12] L. L. Cone, "SKYCAM: An aerial robotic camera system." *Byte*, vol. 10, no. 10, pp. 122–132, 1985.

[13] X. Zhao, "Statics and dynamics simulation of a multi-tethered aerostat system," Ph.D. dissertation, University of Victoria, Dept. of Mechanical Engineering, 2004.

[14] E. Brown, "NIST robocrane® cuts aircraft maintenance costs," http://www.nist.gov/el/isd/robocrane.cfm, July 2 2007.

[15] C. Inc., "Skycam," http://www.cablecam.com/, 2010.

[16] P. Bosscher, R. L. Williams II, L. S. Bryson, and D. Castro-Lacouture, "Cable-suspended robotic contour crafting system," *Automation in Construction*, vol. 17, no. 1, pp. 45 – 55, 2007.

[17] R. Rashad, "Dynamics of the arecibo radio telescope," Master's thesis, McGill University, Dept. of Mechanical Engineering Montreal, Quebec, Canada, February 2005.

[18] A. T. Riechel, P. Bosscher, H. Lipkin, and I. Ebert-Uphoff, "Concept paper: Cable-driven robots for use in hazardous environments," in *Proc. of the 10th International Conference on Robotics & Remote Systems for Hazardous Environments*, vol. 10, Florida, March 2004, pp. 310 – 316.

[19] R. L. Williams II, J. S. Albus, and R. V. Bostelman, "3D cable-based cartesian metrology system," *Journal of Robotic Systems*, vol. 21, no. 5, pp. 237 – 257, 2004.

[20] R. L. Williams II and P. Gallina, "Planar cable-direct-driven robots: Design for wrench exertion," *Journal of Intelligent and Robotic Systems*, vol. 35, no. 2, pp. 203–219, 2002.

[21] A. Fattah and S. K. Agrawal, "On the design of cable-suspended planar parallel robots," *Journal of Mechanical Design, Transactions of the ASME*, vol. 127, no. 5, pp. 1021–1028, 2005.

[22] G. Rosati, P. Gallina, A. Rossi, and S. Masiero, "Wire-based robots for upper-limb rehabilitation," *International Journal of Assistive Robotics and Mechatronics*, vol. 7, no. 2, pp. 3–10, 2006.

[23] Y. Mao and S. K. Agrawal, "Wearable cable-driven upper arm exoskeleton - motion with transmitted joint force and moment minimization," in *Proc of the IEEE International Conference on Robotics and Automation, ICRA2010*, may. 2010, pp. 4334 –4339.

[24] S. K. Mustafa, G. Yang, S. H. Yeo, W. Lin, and M. Chen, "Self-calibration of a biologically inspired 7 DOF cable-driven robotic arm," *IEEE/ASME Transactions on Mechatronics*, vol. 13, no. 1, pp. 66 –75, feb. 2008.

[25] J. S. Sulzer, M. A. Peshkin, and J. L. Patton, "Design of a mobile, inexpensive device for upper extremity rehabilitation at home," in *Proc. of the IEEE International Conference on Rehabilitation Robotics ICORR 2007*, Noordwijk, The Netherlands, June, 12-15 2007, pp. 933–937.

[26] X. Yin and A. P. Bowling, "Dynamic performance limitations due to yielding in cable-driven robotic manipulators," *Journal of Mechanical Design*, vol. 128, no. 1, pp. 311–318, 2006.

[27] A. Trevisani, "Underconstrained planar cable-direct-driven robots: A trajectory planning method ensuring positive and bounded cable tensions," *Mechatronics*, vol. 20, no. 1, pp. 113–127, 2009.

[28] A. Trevisani, P. Gallina, and R. L. Williams II, "Cable-direct-driven robot (CDDR) with passive SCARA support: Theory and simulation," *Journal of Intelligent and Robotic Systems: Theory and Applications*, vol. 46, no. 1, pp. 73–94, 2006.

[29] J. F. Veneman, R. Ekkelenkamp, R. Kruidhof, F. C. T. van der Helm, and H. van der Kooij, "A series elastic- and bowden-cable-based actuation system for use as torque actuator in exoskeleton-type robots," *The International Journal of Robotics Research*, vol. 25, no. 3, pp. 261–281, March 2006.

[30] J. Veneman, R. Kruidhof, E. Hekman, R. Ekkelenkamp, E. Van Asseldonk, and H. van der Kooij, "Design and evaluation of the LOPES exoskeleton robot for interactive gait rehabilitation," *IEEE Transactions on Neural Systems and Rehabilitation Engineering*, vol. 15, no. 3, pp. 379 –386, sep. 2007.

[31] S. K. Mustafa and S. K. Agrawal, "Reciprocal screw-based force-closure of an n-DOF open chain: Minimum number of cables required to fully constrain it," in *Proc. of the International Congress on Robotics and Automation, ICRA2011*, 2011, submitted for review.

[32] S. Behzadipour and A. Khajepour, *Industrial Robotics Theory, Modelling and Control.* plV pro literatur Verlag Robert Mayer-Scholz, 2007, ch. 7, pp. 211–236.

[33] A. Frisoli, M. Prisco, F. Salsedo, and M. Bergamasco, "A two degrees-of-freedom planar haptic interface with high kinematic isotropy," in *Proc. of the 8th IEEE International Workshop on Robot and Human Interaction RO-MAN '99*, 1999, pp. 297–302.

[34] R. L. Williams II and P. Gallina, "Planar cable-direct-driven robots, part I: Kinematics and statics," in *Proc. of the ASME Design Engineering Technical Conference*, vol. 2, 2001, pp. 1233–1240.

[35] M. Gouttefarde, S. Krut, O. Company, and F. Pierrot, *Advances in Robot Kinematics: Analysis and Design.* Springer Netherlands, 2008, ch. On the Design of Fully Constrained Parallel Cable-Driven Robots, pp. 71–78.

[36] M. Hiller, S. Fang, S. Mielczarek, R. Verhoeven, and D. Franitza, "Design, analysis and realization of tendon-based parallel manipulators," *Mechanism and Machine Theory*, vol. 40, no. 4, pp. 429–445, 2005.

[37] P. Gallina and G. Rosati, "Manipulability of a planar wire driven haptic device," *Mechanism and Machine Theory*, vol. 37, no. 2, pp. 215–228, 2002.

[38] S. E. Landsberger and P. Shanmugasundram, "Workspace of a parallel link crane," in *Proc. of IMACS/SICE International Symposium on Robotics, Mechatronics and Manufacturing Systems*, 1992, pp. 479–486.

[39] X. Diao and O. Ma, "Workspace determination of general 6-d.o.f. cable manipulators," *Advanced Robotics*, vol. 22, no. 2-3, pp. 261–278, 2008.

[40] Y. Shen, H. Osumi, and T. Arai, "Set of manipulating forces in wire driven systems," in *Proc. of the IEEE International Conference on Intelligent Robots and Systems*, 1994, pp. 1626–1631.

[41] A. Ming and T. Higuchi, "Study on multiple degree-of-freedom positioning mechanism using wires (Part1). Concept, Design and Control," *International Journal of the Japan Society for Precision Engineering*, vol. 28, no. 2, pp. 131–138, 1994.

[42] P. Bosscher and I. Ebert-Uphoff, "Wrench-based analysis of cable-driven robots," in *Proc. of the IEEE International Conference on Robotics and Automation ICRA2004*, vol. 5, April-1 May 2004, pp. 4950–4955 Vol.5.

[43] T. Bruckmann, L. Mikelsons, T. Brandt, M. Hiller, and D. Schramm, *Parallel Manipulators New Developments*. I-Tech Education and Publishing, 2008, ch. Wire Robots Part I Kinematics, Analysis & Design, pp. 109–132.

[44] P. Lafourcade, M. Llibre, and C. Reboulet, "Design of a parallel wire-driven manipulator for wind tunnels," in *Proc. of the Workshop on Fundamental Issues and Future Research Directions for Parallel Mechanisms and Manipulators*, October 3-4 2002, pp. 187–194.

[45] Y. Shen, H. Osumi, and T. Arai, "Manipulability measures for multi-wire driven parallel mechanism," in *Proc. of the IEEE International Conference on Industrial Technology*, 1994, pp. 550–.

[46] R. L. Williams II, "Cable-suspended haptic interface," *International Journal of Virtual Reality*, vol. 3, no. 3, pp. 13–21, 2005.

[47] P. Gallina, A. Rossi, and R. L. Williams II, "Planar cable-direct-driven robots, part ii: Dynamics and control," in *Proc. of the ASME Design Engineering Technical Conference*, vol. 2, 2001, pp. 1241–1247.

[48] R. L. Williams II and J. Vadia, "Planar translational cable-direct-driven robots: Hardware implementation," in *Proc. of the ASME Design Engineering Technical Conferences DETC 2003*, Chicago, IL, USA, September 2-6 2003.

[49] G. Rosati, D. Zanotto, and A. Rossi, "Performance assessment of a 3D cable-driven haptic device," in *Proc. of the ASME International Mechanical Engineering Congress & Exposition IMECE2008*, vol. 12, Boston, MA, USA, Oct 31 - Nov 6 2008, pp. 597 – 606.

[50] G. Rosati, A. Rossi, G. Boschetti, and A. Trevisani, "First experimental results of an integrated robotic system for haptic teleoperation," in *Proc. of the IEEE International Symposium on Industrial Electronics ISIE*, June 2007, pp. 3138–3143.

[51] G. Rosati, P. Gallina, and S. Masiero, "Design, implementation and clinical tests of a wire-based robot for neurorehabilitation," *IEEE Transactions on Neural Systems and Rehabilitation Engineering*, vol. 15, no. 4, pp. 560–569, 2007.

[52] P. Lafourcade and M. Llibre, "First steps toward a sketch-based design methodology for wire-driven manipulators," in *Proc. of the IEEE/ASME International Conference on Advanced Intelligent Mechatronics*, July 2003, pp. 143–148 vol.1.

[53] C. Gosselin and J. Angeles, "A global performance index for the kinematic optimization of robotic manipulators," *Journal of Mechanical Design*, vol. 113, no. 3, pp. 220–226, 1991.

[54] H. Hadian and A. Fattah, "Best kinematic performance analysis of a 6-6 cable-suspended parallel robot," in *Proc. of the IEEE/ASME International Conference on Mechatronics and Embedded Systems and Applications MESA 2008*, Beijing, China, 2008, pp. 510 – 515.

[55] S.-R. Oh and S. K. Agrawal, "Cable suspended planar robots with redundant cables: Controllers with positive tensions," *IEEE Transactions on Robotics*, vol. 21, no. 3, pp. 457–465, 2005.

[56] D. Surdilovic, R. Bernhardt, and T. Schmidt, "STRING-MAN: A new wire robotic system for gait rehabilitation," in *Proc. of the IEEE International Conference on Rehabilitation Robotics ICORR2003*, Daejeon, Republic of Korea, Apr 2003, pp. 2031 – 2036.

[57] R. Dekker, A. Khajepour, and S. Behzadipour, "Design and testing of an ultra-high-speed cable robot," *Int. J. Robot. Autom.*, vol. 21, pp. 25–34, January 2006.

[58] S. Krut, O. Company, and F. Pierrot, "Velocity performance indices for parallel mechanisms with actuation redundancy," *Robotica*, vol. 22, no. 2, pp. 129 – 139, 2004.

[59] ——, "Force performance indexes for parallel mechanisms with actuation redundancy, especially for parallel wire-driven manipulators," in *Proc. of the IEEE/RSJ International Conference on Intelligent Robots and Systems IROS2004*, vol. 4, Sendai, Japan, 2004, pp. 3936–3941.

[60] A. T. Riechel and I. Ebert-Uphoff, "Force-feasible workspace analysis for underconstrained, point-mass cable robots," in *Proc. of the IEEE International Conference on Robotics and Automation ICRA2004*, 2004, pp. 4956 – 4962.

[61] P. Bosscher and I. Ebert-Uphoff, "Disturbance robustness measures for underconstrained cable-driven robots," in *Proc. of the IEEE International Conference on Robotics and Automation ICRA2006*, May 2006, pp. 4205–4212.

[62] P. A. Voglewede and I. Ebert-Uphoff, "Application of the antipodal grasp theorem to cable-driven robots," *IEEE Transactions on Robotics*, vol. 21, no. 4, pp. 713–718, 2005.

[63] A. Khajepour, S. Behzadipour, R. Dekker, and E. Chan, "Light weight parallel manipulators using active/passive cables," USA Patent 7 367 771, May, 2008. [Online]. Available: http://www.freepatentsonline.com/7367771.html

[64] D. Surdilovic, J. Zhang, and R. Bernhardt, "STRING-MAN: Wire-robot technology for safe, flexible and human-friendly gait rehabilitation," in *Proc. of the IEEE International Conference on Rehabilitation Robotics ICORR2007*, June 2007, pp. 446–453.

[65] R. Caracciolo, G. Boschetti, N. D. Rossi, G. Rosati, and A. Trevisani, "A master-slave robotic system for haptic teleoperation," in *Proc. of the 8th Biennial ASME Conference on Engineering Systems Design and Analysis, ESDA2006*, 2006, pp. Torino, Italy.

[66] C. Fanin, P. Gallina, A. Rossi, U. Zanatta, and S. Masiero, "Nerebot: a wire-based robot for neurorehabilitation," in *8th International Conference on Rehabilitation Robotics ICORR03*, Daejeon, Republic of Korea, April 2003.

[67] G. Rosati, P. Gallina, S. Masiero, and A. Rossi, "Design of a new 5 d.o.f. wire-based robot for rehabilitation," in *Proc. of the IEEE 9th International Conference on Rehabilitation Robotics, ICORR2005*, vol. 2005, 2005, pp. 430–433.

[68] G. Rosati, M. Andreolli, A. Biondi, and P. Gallina, "Performance of cable suspended robots for upper limb rehabilitation," in *Proc. of the IEEE 10th International Conference on Rehabilitation Robotics, ICORR2007*, Noordwijk, the Netherlands, June 13-15 2007, pp. 385–392.

[69] S. Masiero, A. Celia, G. Rosati, and M. Armani, "Robotic-assisted rehabilitation of the upper limb after acute stroke," *Archives of Physical Medicine and Rehabilitation*, vol. 88, no. 2, pp. 142–149, 2007.

[70] S. Masiero, M. Armani, and G. Rosati, "Upper extremity robot-assisted therapy in rehabilitation of acute stroke patients: focused review and results of a new randomized controlled trial," *Journal of Rehabilitation Research and Development*, 2011, accepted for publication.

[71] W. T. Dempster, "Space requirements of the seated operator, geometrical, kinematic, and mechanical aspects of the body with special reference to the limbs," Defense Technical Information Center, U.S., Tech. Rep., July 1955.

[72] G. Rosati, R. Secoli, D. Zanotto, A. Rossi, and G. Boschetti, "Planar robotic systems for upper-limb post-stroke rehabilitation," in *Proc. of the ASME International Mechanical Engineering Congress & Exposition IMECE2008*, vol. 2, Boston, MA, USA, Oct 31 - Nov 6 2008, pp. 115 – 124.

[73] G. Rosati, D. Zanotto, R. Secoli, and A. Rossi, "Design and control of two planar cable-driven robots for upper-limb neurorehabilitation," in *Proc. of the IEEE 11th International Conference on Rehabilitation Robotics ICORR2009*, Kyoto, Japan, June 23-26 2009.

[74] G. Rosati, J. E. Bobrow, and D. Reinkensmeyer, "Compliant control of post-stroke rehabilitation robots: using movement-specific models to improve controller performance," in *Proceedings of the ASME International Mechanical Engineering Congress & Exposition, IMECE 2008*, Boston, MA, USA, Oct 31 - Nov 6 2008.

[75] G. Rosati, D. Zanotto, and S. K. Agrawal, "On the design of adaptive cable-driven systems," *Journal of Mechanical Design*, vol. Accepted for publication, 2010.

[76] G. Rosati and D. Zanotto, "A novel perspective in the design of cable-driven systems," in *Proc. of the ASME International Mechanical Engineering Congress & Exposition IMECE2008*, vol. 12, Boston, MA, USA, Oct 31 - Nov 6 2008, pp. 617 – 625.

[77] T. H. Massie and K. J. Salisbury, "PHANToM haptic interface: a device for probing virtual objects," in *Proc. of the ASME Winter Annual Meeting, Symposium on Haptic Interfaces for Virtual Environment and Teleoperator Systems*, Chicago, IL, USA, Nov 1994, pp. 295 – 299.

[78] T. Yoshikawa, "Analysis and control of robot manipulators with redundancy." in *Proc. of the 1st International Symposium on Robotics Research*, 1984, pp. 735–747.

[79] L. Sciavicco and B. Siciliano, *Modelling and control of robot manipulators*, 2nd ed. Springer, 2000.

[80] T. Yoshikawa, "Manipulability of robotic mechanisms," *International Journal of Robotics Research*, vol. 4, no. 2, pp. 3–9, 1985.

[81] Y. Li and Q. Xu, "GA-based multi-objective optimal design of a planar 3-DOF cable-driven parallel manipulator," in *Proc. of the IEEE International Conference on Robotics and Biomimetics*, Kunming, China, 17-20 December 2006.

[82] J. Angeles, F. Ranjbaran, and R. Patel, "On the design of the kinematic structure of seven-axes redundant manipulators for maximum conditioning," in *Proc. of the IEEE International Conference on Robotics and Automation, ICRA 1992*, vol. 1, May 1992, pp. 494–499.

[83] F. Ranjbaran, J. Angeles, and M. A. González-Palacios, "The mechanical design of a seven-axes manipulator with kinematic isotropy," *Journal of Intelligent and Robotic Systems*, vol. 14, no. 1, pp. 21–41, 1995.

[84] D. Chablat, S. Caro, P. Wenger, and J. Angeles, "The isoconditioning loci of planar three-DOF parallel manipulators," in *Proc. of the International Conference on Integrated Design and Manufacturing in Mechanical Engineering – IDMME 2002*, Clermont-Ferrand, France, May, 14-16 2002, pp. 1–10.

[85] H. Asada, "Dynamic analysis and design of robot manipulators using inertia ellipsoids," in *Proc. of the IEEE International Conference on Robotics and Automation*, vol. 1, March 1984, pp. 94–102.

[86] O. Khatib, "Inertial properties in robotic manipulation. An object-level framework," *International Journal of Robotics Research*, vol. 14, no. 1, pp. 19–36, 1995.

[87] D. Zanotto, G. Rosati, and A. Rossi, "Performance analysis of planar cable-based parallel manipulators," in *Proc. of the ASME Biennial Conference on Engineering Systems Design and Analysis ESDA2010*, Istanbul, Turkey, July 12-14 2010.

[88] Y. Yang and Y. Zhang, "A new cable-driven haptic device for integrating kinesthetic and cutaneous display," in *Proc. of the ASME International Conference on Reconfigurable Mechanisms and Robots IFToMM 2009*, London, UK, June 22-24 2009, pp. 386 – 391.

[89] A. Ming and T. Higuchi, "Study on multiple degree-of-freedom positioning mechanism using wires (Part2). Development of a Planar Completely Restrained Positioning Mechanism," *International Journal of the Japan Society for Precision Engineering*, vol. 28, no. 3, pp. 235–242, 1994.

[90] M. Yamamoto, N. Yanai, and A. Mohri, "Inverse dynamics and control of crane-type manipulator," in *Proc. of the IEEE/RSJ International Conference on Intelligent Robots and Systems IROS1999*, vol. 2, 1999, pp. 1228–1233.

[91] ——, "Trajectory control of incompletely restrained parallel-wire-suspended mechanism based on inverse dynamics," *IEEE Transactions on Robotics*, vol. 20, no. 5, pp. 840 – 850, Oct. 2004.

[92] T. Heyden and C. Woernle, "Dynamics and flatness-based control of a kinematically undetermined cable suspension manipulator," *Multibody System Dynamics*, vol. 16, no. 2, pp. 155 – 177, 2006.

[93] S. Krut, N. Ramdani, M. Gouttefarde, O. Company, and F. Pierrot, "A parallel cable-driven crane for scara-motions," in *Proc. of the ASME International Design Engineering Technical Conferences and Computers and Information in Engineering Conference DETC2008*, vol. 2, New York City, NY, United states, 2008, pp. 101 – 108.

[94] X. J. Liu, Z. L. Jin, and F. Gao, "Optimum design of 3-DOF spherical parallel manipulators with respect to the conditioning and stiffness indices," *Mechanism and Machine Theory*, vol. 35, pp. 1257–1267(11), 2000.

[95] C. M. Gosselin, "Adaptive robotic mechanical systems: A design paradigm," *Journal of Mechanical Design*, vol. 128, no. 1, pp. 192–198, 2006.

[96] *Uniform federal accessibility standards*, U.S. Architectural and Transportation Barriers Compliance Board, August 7 1984, federal Register, 49 FR 31528.

[97] L. Bonometti, *Convertitori di potenza e servomotori brushless*. UTET Div. Periodici Scient., 2001.

[98] S. Boyd and L. Vandenberghe, *Convex Optimization*. Cambridge University Press, 2004.

[99] J. Emken, R. Benitez, and D. Reinkensmeyer, "Human-robot cooperative movement training: Learning a novel sensory motor transformation during walking with robotic assistance-as-needed," *Journal of NeuroEngineering and Rehabilitation*, vol. 4, no. 1, p. 8, 2007.